6-2012

# Benchmarking of a Single-Cylinder Engine Toward the Development of a Direct Fuel-Injection System

Michael J. Nienhuis
*Western Michigan University*, nienhuisengineering@gmail.com

# BENCHMARKING OF A SINGLE-CYLINDER ENGINE TOWARD THE DEVELOPMENT OF A DIRECT FUEL INJECTION SYSTEM

by

Michael J. Nienhuis

A Thesis
Submitted to the
Faculty of The Graduate College
in partial fulfillment of the
requirements for the
Degree of Master of Science in (Mechanical) Engineering
Department of Mechanical and Aeronautical Engineering
Advisor: Claudia Fajardo, Ph.D.

Western Michigan University
Kalamazoo, Michigan
June 2012

THE GRADUATE COLLEGE
WESTERN MICHIGAN UNIVERSITY
KALAMAZOO, MICHIGAN

Date May 29, 2012

WE HEREBY APPROVE THE THESIS SUBMITTED BY

Michael J. Nienhuis

ENTITLED Benchmarking of a Single-Cylinder Engine toward the Development of a Direct Fuel-Injection System

AS PARTIAL FULFILLMENT OF THE REQUIREMENTS FOR THE

DEGREE OF Master of Science in Engineering (Mechanical)

Mechanical and Aeronautical Engineering
(Department)

Thesis Committee Chair

Mechanical Engineering
(Program)

Thesis Committee Member

Thesis Committee Member

APPROVED

Dean of The Graduate College

Date June 2012

# BENCHMARKING OF A SINGLE-CYLINDER ENGINE TOWARD THE DEVELOPMENT OF A DIRECT FUEL-INJECTION SYSTEM

Michael J. Nienhuis, M.S.E.

Western Michigan University, 2012

In this study, the performance and efficiency of a single-cylinder gasoline, four-stroke cycle engine was benchmarked in support of the Formula SAE student project. The development of an engine test stand, instrumentation, data acquisition, and test plan is described in detail. Experimental results in the areas of engine performance and efficiency are discussed. Physical test data were used to refine a previous model of a single-cylinder, gasoline, direct-injection engine. Results from this effort are discussed and compared to those obtained in a preliminary study. The current work advances the development of more efficient power-train technologies for application in small-displacement engines.

ACKNOWLEDGMENTS

I would like to thank all that helped throughout this project. First and foremost I would like to thank my advisor, Dr. Claudia Fajardo. Her support and knowledge in the area of thermodynamics and internal combustion engines made this project possible. Her support towards the advisory role of the Formula SAE student design project provided this study with a purpose.

I would like to thank Dr. Richard Hathaway for his help in problem solving and advice from his years of experience with physical testing and racing. Without his help the testing conducted during this project would have never gotten off the ground.

I would like to thank Dr. William Lou for his help within the computational fluid dynamics simulations area. The lessons learned in the class room on the subject of computational fluid dynamics provided the background information necessary to further this project.

I would like to thank Pete Thannhauser for his technical assistance with both the data acquisition and Lab-View interface. His years of experience with programming and testing made this project possible.

I would like to thank Glen Hall and John Jager for all their time, advice, and help in the construction of the engine test stand. I would also like to thank the entire Formula SAE team at Western Michigan University, both past and present, for all their hard work and dedication towards improving the program over the years.

Last but not least I would like to thank my friends and family for all their support throughout this project.

Michael J Nienhuis

TABLE OF CONTENTS

Table of Contents—continued

Table of Contents—continued

LIST OF TABLES

LIST OF FIGURES

# CHAPTER 1

# INTRODUCTION

## 1.1 Background and Motivation

With rising fuel costs and increasingly stringent regulations on fuel economy in private transportation, automotive manufacturers are continually pursuing fuel-saving technologies. By 2016, the environmental protection agency (EPA) will require a fleet-wide $CO_2$ emissions level of 250 g/mi for combined passenger car and light trucks. If manufacturers were to accomplish this only through improved fuel economy, the corresponding fuel economy would be 35.5 miles per gallon (mpg). The current 2012 requirement is 295 g/mile, or a corresponding fuel economy of 30.1 mpg (1). This corresponds to a 17% increase in fuel economy.

Gasoline internal combustion engines incorporating direct-fuel injection are now widely implemented in several power train packages, including Ford Motor Company's EcoBoost systems (2) Chevrolet's Ecotech (3), and Toyota's D-4S fuel injection system (4). Previous fuel delivery technologies used in internal combustion engines include carburetion and port fuel injection (PFI). Both methods require fuel to be delivered outside of the combustion chamber. In the case of carburetors, fuel is mixed with the incoming air at the intake system entrance. The mass of fuel delivered to the engine is varied for different speeds and loads, based on Bernoulli's principle of fluid dynamics. Higher intake air flow rates produce higher velocities, drawing more fuel through the venturi. This technology is still utilized in small utility-engine applications, but is no longer utilized in production automobiles due to its inability to compensate for widely

varying atmospheric conditions without physical adjustment. In port-fuel-injection, an electronically controlled fuel injector is placed within the intake track, as shown in Figure 1 (A). This system provides many advantages over carburetion, including its ability to meter the fuel more precisely over a wide range of engine-operating and atmospheric conditions. This is accomplished through the use of a programmable engine control module (ECM).

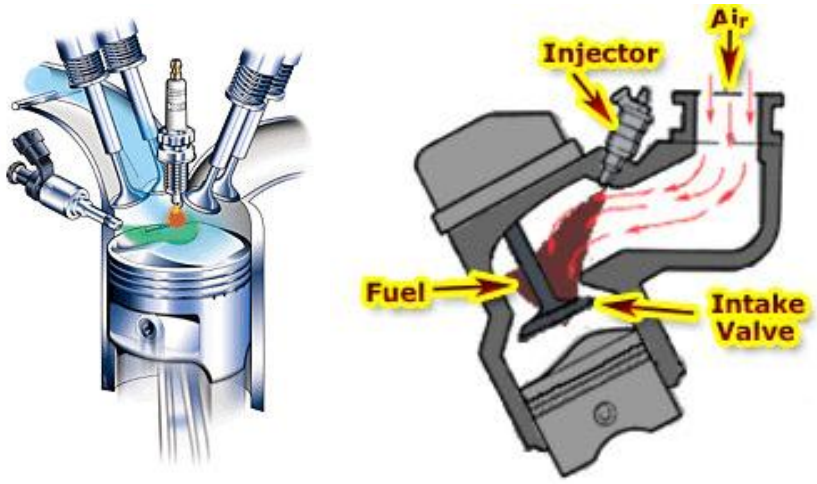


(A) (B)

*Figure 1*. Example of gasoline direct injection (A) and port fuel injection (B) (5)

In gasoline direct-injection fuel systems, fuel is directly injected into the combustion chamber, as shown in Figure 1(A). There are several advantages to this system compared to PFI engines. These include more precise fuel metering, less fuel "lost" due to wall wetting and pooling, and decreased in-cylinder temperatures due to the cooling effect induced by the evaporating fuel. Wall wetting and pooling occur because the injected fuel does not mix well with the incoming air charge and, as a result, collects along the wall boundaries such as the intake track or combustion surfaces. This fuel does not burn efficiently, and contributes to unburned hydrocarbon emissions. With direct fuel

injection, the injected fuel vaporizes within the combustion chamber, cooling the in-cylinder air charge. This decrease in the chamber temperature decreases the likelihood of knock, enabling engine designers to increase the compression ratio and/or use higher intake pressures in forced-induction applications, which can increase engine efficiency and performance.

The motivation for automobile manufacturers to improve fuel economy has influenced the competitive world of motorsports. Several major sanctioning bodies have created regulations to motivate competitors to develop and implement fuel-saving technologies. Formula One, for instance, has allowed kinetic energy recovery systems (KERS) (6). Similar to hybrid systems available in passenger vehicles, KERS is used to recover and store energy generated during vehicle braking. This energy is then used to boost vehicle power under acceleration. The boost in power, controlled by the driver, is limited to a maximum of 80 HP (60 kW) and a total duration of 6.67 seconds per lap. The energy can be stored either electrically through batteries, mechanically through a flywheel, or hydraulically through the use of a pressure accumulator. A ban on refueling was also implemented in 2010 to promote fuel economy within the sport (7). Since vehicle physical size and mass are always given primary consideration, the more fuel efficient the vehicle is, the less on board fuel mass is required for the duration of the event. Sponsors are also doing their part through contingencies such as the Michelin Green X Challenge in the Le Mans racing series, which reward competitors who succeed in consuming the least fuel without compromising performance (8).

Formula SAE (FSAE) is a student design competition that focuses on the development of new technologies through the creativity of young engineers. The event is part of the collegiate design series organized by the Society of Automotive Engineers (SAE) International. The annual series holds international competitions, including two within the United States. To participate, students are tasked with conceiving, designing, fabricating, and competing with a small, open-wheel, open cockpit, formula-style race car (9). The rules established by SAE ensure the safety of the competitors, while also allowing freedom to explore new technologies.

The major rules pertaining to powertrain state that the engine used to power the car must

- be a piston engine(s).
- incorporate a four-stroke primary heat cycle.
- have a displacement not exceeding 610 cubic centimeter (cc) per cycle.

In addition, a single circular restrictor must be placed in the intake system (between the throttle and the engine) and all airflow into the engine must pass through the restrictor (9).

Figure 2 shows an example of a Formula SAE competition vehicle: the 2009 WMU Formula Racing entry.


*Figure 2*. 2009 WMU formula SAE competition vehicle

Each vehicle is judged and scored in a series of static and dynamic events, with 1,000 total possible points. The static events at each competition include a marketing presentation worth 75 points, engineering design presentation worth 150 points, and a cost analysis presentation worth 100 points. The dynamic events, which judge the performance and reliability of the vehicles, include the acceleration event (75 points), the skid-pad event (50 points), the autocross event (150 points), and an endurance event coupled with a fuel economy score (9). Changed for the 2009 season, the scoring of fuel economy during the endurance event was increased from 50 points to 100 points. Additionally, out of the 1,000 total points, the scoring of the endurance event decreased from 350 points to 300 points. Finally, up to a 100-point penalty was implemented for those vehicles which have fuel economies less than 9.05 miles-per-gallon (mpg) (26 liters/100km) (10). This has placed significantly greater focus on fuel efficiency.

Most likely in response to fuel-economy rule changes, engine downsizing has become a recent trend within the Formula SAE competition series. Table 1 shows the types of engines used in FSAE vehicles between 2003 and 2011. These data were compiled from

the Formula SAE Michigan event competition programs. It is clear that the majority of engines chosen by teams are four-cylinder, generally out of sport motorcycles such as the Honda 600 F4i, Suzuki GSXR 600, and Yamaha R6. These engines are desirable due to their integrated transmission, high performance, and wide availability in the used-engine market. Drawbacks of this choice are the relatively high package size and weight of the base engine and subsystems.

The use of single-cylinder engines in the formula SAE competition has increased over the past six years, from 5% in 2003 to 22% in 2011 (table 1). Many of these engines, sourced from off-road performance motorcycles and all-terrain vehicles, feature integrated transmissions, either carburetion or port-fuel injection, and have total displacement volumes ranging between 450 and 525cc. Despite the overall reduction in output power due to engine downsizing, the resulting power-to-weight ratio favors downsizing when the overall vehicle weight is considered. This is because, as a result of engine downsizing, smaller and hence lighter subsystems are needed. Further, incorporating technical advances aimed at increasing engine efficiency (e.g., gasoline direct-injection) might be easier to implement in a single-cylinder engine.

*Table 1.* Breakdown of vehicle engine configurations for Formula SAE Michigan competition

| Year | 2003 | 2007 | 2008 | 2009 | 2010 | 2011 |
|---|---|---|---|---|---|---|
| Total Vehicles Listed | 80 | 100 | 105 | 82 | 72 | 103 |
| Four Cylinder | 81% | 82% | 77% | 72% | 74% | 67% |
| Single Cylinder | 5% | 7% | 13% | 21% | 17% | 22% |
| Other Engine Configuration | 1% | 2% | 10% | 7% | 8% | 10% |
| Engine Not Listed | 13% | 9% | 0% | 0% | 1% | 1% |

## 1.2 Previous Work

Most of technical literature supporting the FSAE collegiate design competitions has focused on optimizing the performance of four-cylinder engines in the presence of the 20 mm flow restrictor required by SAE competition rules (1). These research areas have included intake air system design and performance optimization with and without forced-induction (2-6), camshaft design (3, 7), and engine tuning through optimization of fuel and ignition maps (8, 9). Technical data on single-cylinder engines for FSAE applications has been very limited thus far. The present author was only able to identify the work of Corrigan et al., who developed a numerical model to evaluate the suitability of a single-cylinder, 450cc engine for use in a FSAE vehicle (10). Results indicated that, in order to remain competitive using a single-cylinder engine in a 160 kg vehicle, a power output of 52 kW is necessary. In the study, the numerical model was validated using experimental data from previous-generation, lower-displacement engines.

The trend in engine downsizing and the fuel economy rule change motivated the Western Michigan University Formula SAE team to explore innovative technologies that could be adapted to a Formula SAE competition vehicle. As part of a senior capstone project, the author pursued the evaluation of a gasoline-direct-injection fuel conversion for a 450cc, single-cylinder motorcycle engine (11). The study incorporated parametric solid modeling, coupled with one-and three-dimensional computational fluid dynamics (CFD) engine simulations to develop and analyze several initial design concepts. The primary

goal of this project was to develop an initial concept design for fuel injector placement and combustion chamber geometry. Several assumptions were made throughout the project due to the limited data available for the chosen engine. For example, important simulation inputs such as boundary conditions for pressure and temperature were unavailable. Model validation was also limited to comparing the torque and power curves predicted by the model with data from an aftermarket exhaust manufacturer. This comparison had limited validity, since the experimental conditions under which the torque and power curves were measured were not published by the manufacturer.

The final proposed design required minimal modifications to the OEM cylinder head and incorporated the original casting. Results indicated that a theoretical, maximum increase in fuel economy of 12.5% (compared to the port-fuel-injected configuration) could be achieved. It also predicted a 4% and 2.5% increase in power and torque, respectively, over the entire speed range at wide-open-throttle (WOT). The new design would most likely require a shallow-bowl piston to enhance fuel-air mixing (11).

While adequate as an initial feasibility study, the author's preliminary investigation revealed that detailed, physical test data would be required to refine the design and transition the proposed design to a prototype stage.

## 1.3 Goals and Objectives

The goal of this project is to conduct a thorough, quantitative, baseline study on the performance and efficiency of a single-cylinder gasoline engine to support ongoing design efforts by the WMU Formula SAE team. The data acquired from physical testing will serve two objectives. First, identify areas where design changes of the port-fuel-injected engine could be implemented to improve its performance and efficiency; second, to acquire the data necessary to refine and validate a CFD engine model to support the development of a direct-injected engine for application in the FSAE vehicle. The tasks necessary to fulfill the project objectives are:

1) Design and construct a modular and universal small-engine test stand. The test stand will be developed to facilitate testing of engines directly from the crankshaft. It will also incorporate the gearing required to test engines with integrated transmissions, and whose final transmission output torque exceeds the capacity of the dynamometer.
2) Design and implement a universal, small-engine sensor package, as well as an instrumentation and data acquisition system that ensures interchangeability, quick replacement of sensors, and real-time monitoring of engine data.
3) Benchmark the single-cylinder RM-Z450 engine under steady-state in order to (1) quantify engine performance and efficiency and (2) support the development of a CFD model of the engine.
4) Refine the existing CFD model of the RM-Z450 engine during the intake and compression strokes using data gathered through physical testing.

This thesis is organized as follows:

Chapter 2 will discuss performance metrics, as well as the development of the small-engine test stand, instrumentation, data acquisition system, and data processing mechanisms. Chapter 3 will present results of engine benchmarking, including those for performance, efficiency, operating conditions, and boundary conditions. Chapter 4 will provide background on previous design and simulation efforts (11), discuss the areas of uncertainty within the preliminary study, as well as the methodology and results from new model-refinement efforts. Conclusions and ideas for future work will be presented in Chapter 5.

# CHAPTER 2

# QUANTITATIVE METRICS, HARDWARE, AND INSTRUMENTATION

## 2.1 Performance Metrics

### Brake Torque and Power

The performance of an internal combustion engine can be quantified using several quantities. Torque is used to measure an engine's ability to do work (12). The torque qualifier (e.g., brake, wheel, etc) depends on the measurement location. Brake torque is measured at the output of the crankshaft, typically using an engine dynamometer. Wheel torque is typically measured using a chassis dynamometer at the drive wheels of the vehicle. It includes drive-train and rolling resistance losses.

In the present setup, schematically shown in Figure 3, brake torque could not be measured at the crankshaft output, but rather at the output of the transmission. This is because the 2008 Suzuki RM-450Z engine incorporates an integrated transmission with a minimum final-drive ratio of 2.39:1. As a result, the torque measured at the transmission output is 2.39 times higher than the torque produced at the crankshaft. The resulting torque would be outside the capacity of the dynamometer (Go-Power D100) if directly coupled to the transmission output shaft. To address this problem, the system was modified to incorporate a belt drive system with a1:2.41 ratio. The selected ratio provided the closest match to the original value using an off-the-shelf, commercially available system. The resulting overall ratio between the engine crankshaft and dynamometer is 1:1.03. The torque and power data presented in the results incorporate this correction.

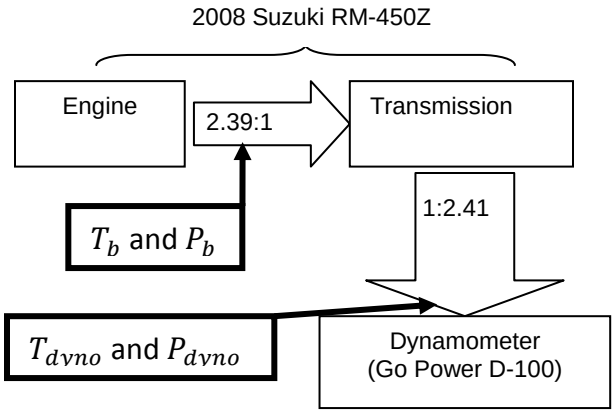


*Figure 3*. Engine-to-dynamometer torque flow chart. Brake torque and power are traditionally measured at the crankshaft. In the present system, torque and power are measured at the dynamometer

As shown in equation 1, the power measured at the dynamometer ($P_{dyno}$) is a function of the dynamometer speed ($N_{Dyno}$) and torque ($T_{dyno}$).

$$P_{dyno} = 2 * \pi * N_{Dyno} * T_{dyno} \qquad [1]$$

In this work, brake torque and power will be conservatively quantified because they are measured at the dynamometer (i.e., they are, strictly $T_{dyno}$ and $P_{dyno}$, respectively). As a result, these quantities will include mechanical losses in the integrated transmission and the engine-dynamometer coupler. As shown by equations 2 and 3, the true brake torque and power can be calculated by measuring and correcting for the mechanical losses ($P_{mech}$, $T_{mech}$) in the dynamometer-engine coupling mechanism, which includes belt drive, support bearings, and coupler friction. These brake quantities represent the usable power and torque delivered by the engine to a load (12).

$$P_b = P_{dyno} + P_{mech} \quad [2]$$

$$\mathrm{T_b} = \mathrm{T_{dyno}} + \mathrm{T_{mech}} \quad [3]$$

Although labeled "brake torque" and "brake power", the torque and power values presented in the results section were not corrected for mechanical losses in the engine-dynamometer coupling mechanisms. These losses include the bearing friction, belt to pulley friction, and friction within the jaw-type flexible coupler connected to the dynamometer. Therefore, the results will provide a conservative estimate of the engine torque and power output capabilities.

Indicated Work and Power

Indicated work represents the work extracted from the fluid operating in the combustion chamber. In order to quantify indicated work, the in-cylinder pressure as a function of cylinder volume is obtained, an example of which is shown in Figure 4. As shown in equation 4, the work can be calculated by integrating the in-cylinder pressure with respect to combustion chamber volume.

The indicated work per cycle can be broken down into three main quantities: gross indicated work, pumping work, and net-indicated work. Gross indicated work $W_{c,ig}$ represents the work done by the working fluid on the piston through the compression and expansion portion of the engine cycle. Pumping work per cycle $W_p$ represents the work done to induct the fresh charge during the intake stroke and to expel the products of

combustion during the exhaust stroke. The net indicated work per cycle $W_{c,in}$ represents the work done throughout the entire cycle, and is equal to the algebraic sum of gross-indicated and pumping work.

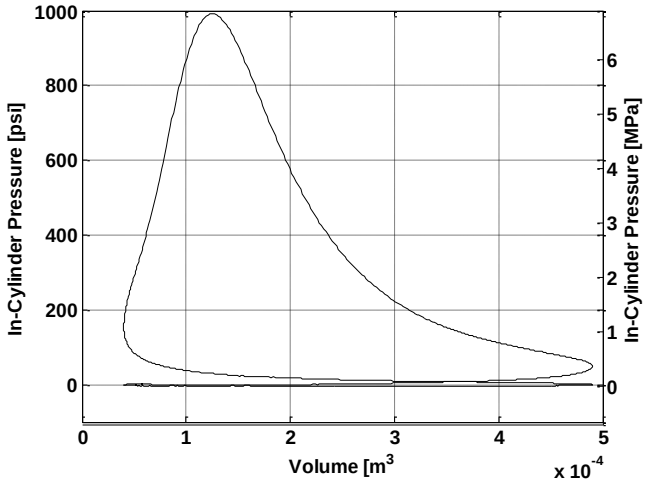


*Figure 4*. Representative pressure-volume diagram used to calculate indicated parameters. Conditions: 65% throttle, 6,500 RPM.

$$W_{c,i} = \oint p\, dV \quad [4]$$

As shown in equation 5, indicated power can be calculated from indicated work.

$$P_i = \frac{W_{c,i}\, N}{n_R} \quad [5]$$

The gross-indicated power ($P_{i,g}$) is equal to the sum of brake power and friction power. Traditionally, friction power includes the power used to drive engine accessories (e.g., mechanical oil/water pumps and alternator), rubbing friction (e.g., piston-wall and valve

trains sliding surfaces) and pumping power (12). The rubbing component, which refers to friction generated internally, within the engine, encompasses the boundary (i.e., metal on metal), hydrodynamic (i.e., lubricant viscous drag), and mixed lubrication regimes. For this study, friction losses in the transmission and as a result of the coupling system are considered as accessory friction.

$$P_{ig} = P_b + P_f \quad [6]$$

Mean Effective Pressure

Mean effective pressure measures engine performance independent of engine displacement. As shown in equation 7, the mean effective pressure is defined as the work per cycle ($W_{c,i}$) divided by the engine displacement volume ($V_d$). The gross-indicated mean effective pressure ($imep_g$) and pumping mean effective pressure ($pmep$) can be calculated from the gross indicated work and pumping work, respectively.

$$mep = \frac{W}{V_d} \quad [7]$$

The brake mean effective pressure ($bmep$), shown in equation 8, can also be quantified from the measured brake torque.

$$bmep = \frac{2\pi\ T_b n_R}{V_d} \quad [8]$$

Friction losses are quantified according to equation 9, where pumping losses are treated as a separate contributor to the overall engine friction.

$$fmep = imep_g - |pmep| - |bmep| \quad [9]$$

Coolant Load

The amount of energy released to the engine coolant system is referred to as coolant load. Under steady state operation, coolant load can be quantified using equation 11, where $m_{dot,coolant}$ represents the mass flow rate of coolant, $C_{p\,Coolant}$ represents the specific heat of the coolant, and $\Delta T_{Coolant}$ represents the temperature drop across the heat exchanger cooling the engine.

$$Q_{dot,coolant} = (m_{dot}\, C_P\ \Delta T)_{Coolant} \quad [11]$$

2.2. Efficiency Metrics

Volumetric Efficiency

In four-stroke engines, volumetric efficiency quantifies the effectiveness of the air induction process. As shown in equation 12, it is defined as the ratio of the volume flow rate of inducted air to the theoretical maximum based on engine speed and displacement volume. Many factors influence volumetric efficiency, including the level of flow restriction in the intake air track.

$$\eta_v = \frac{m_{dot,a} n_R}{\rho_{a,i} V_d N} = \frac{V_{dot,a}, n_R}{V_d N} \qquad [12]$$

Mechanical Efficiency

The ratio of brake power to gross-indicated power is known as mechanical efficiency, represented by equation 13. As mentioned in Section 2.1, the difference between brake power and gross indicated power is friction power ($P_f$), which accounts for pumping, rubbing, and accessory friction. It is emphasized again that, in this study, the friction power also includes the mechanical losses due to the integrated transmission and engine-to-dynamometer coupling system.

$$\eta_m = \frac{P_b}{P_{ig}} = 1 - \frac{P_f}{P_{ig}} \qquad [13]$$

Specific Fuel Consumption

The specific fuel consumption (*sfc*) measures how effectively an engine uses the available fuel to produce power (equation 14). The lower the specific fuel consumption, the more efficiently the engine uses the fuel supplied for a given output power.

$$sfc = \frac{m_{dot,f}}{P} \qquad [14]$$

Fuel Conversion Efficiency

Related to specific fuel consumption, the fuel conversion efficiency (equation 15) represents how effectively the engine uses the available fuel energy (i.e., the fuel heating value ($Q_{HV}$)). In this study, 93-octane gasoline was used, which has a heating value of 44 MJ/kg.

$$\eta_f = \frac{1}{sfc\, Q_{HV}} \qquad [15]$$

## 2.3 Experimental Hardware and Setup

General Engine Specifications

The base power plant, shown in Figure 5, is a 2008 model year, Suzuki RM-Z450, single-cylinder, 450-cc-displacement, four-stroke engine. This engine, originally intended for off-road, closed-course competition motorcycles, features an integrated clutch and five-speed transmission, dual-overhead-cam (DOHC), four-valve cylinder head, electronic-controlled port-fuel-injected (PFI) fuel system, and liquid cooling. Table 2 shows detailed engine specifications. This engine was used in a previous computational fluid dynamics (CFD) study to evaluate the feasibility of replacing the stock port-fuel-injection system with a direct-injection unit (11). More details on this effort, as it relates to the present work, will be provided in chapter 4.

*Figure 5*. 2008 Suzuki RM-450Z engine

The original intake, exhaust, port fuel-injection systems and engine control module (ECM) were used for this study. Although these components are typically redesigned by teams to comply with the FSAE powertrain rules (e.g., by incorporating an intake flow restrictor), this investigation focused on benchmarking the stock engine to produce baseline data that can be used to assess the performance of redesigned systems.

| General Engine Specifications | | | |
|---|---|---|---|
| **Specification** | **Quantity** | **Specification** | **Quantity** |
| Type | Four-Stroke, Liquid-Cooled, DOHC | Clutch | Wet multi-plate type |
| Cylinders | 1 | Transmission | 5-speed constant mesh |
| Displacement | 449 cm^3 (27.4 in^3) | Fuel system | Electronic port fuel injection |
| Bore | 96.0 mm (3.780 in) | Fuel pressure | 294 kPa (41.81 PSI) |
| Stroke | 62.1 mm (2.445 in) | Oil system | Semi dry sump |
| Compression ratio | 12.2:1 | Throttle Body bore | 43mm |
| Number of intake valves | 2 | Idle engine speed | 2,000 ± 100 RPM |
| Number of exhaust valves | 2 | Maximum engine speed | 10,500 RPM |
| Intake valve diameter | 36 mm (1.4 in) | Base Spark Timing | 6 deg. B.T.D.C. @ 2000 RPM |
| Exhaust valve diameter | 31 mm (1.2 in) | Overall mass dry* | 31.98 kg (70.5 lbs) |

*obtained through physical measurement of actual engine.

*Table 2*. General engine specifications for 2008 Suzuki RM-Z450 (13)

The mass of fuel injected depends on the injection duration (i.e. pulse- width) commanded by the ECM to the fuel injector. A flow chart is shown in Figure 6, describing the fuel injection modes of operation. The basic fuel injection pulse width is determined by the ECM using the intake air pressure, engine speed, and throttle opening. No compensation is applied to the fuel pressure as function of manifold pressure. This is important to note because as manifold pressure decreases, the differential pressure between the injector and manifold increases. This can potentially increase the amount of fuel injected for a constant pulse width and fuel pressure, possibly causing over-fueling. Because fuel pressure is held constant in this engine, manifold pressure is considered in the determination of the basic fuel injection pulse width, in addition to parameters such as engine coolant temperature, intake air temperature, system operating voltage, and acceleration or deceleration. The final fuel injection pulse width is determined by correcting the base injection pulse width with these factors.

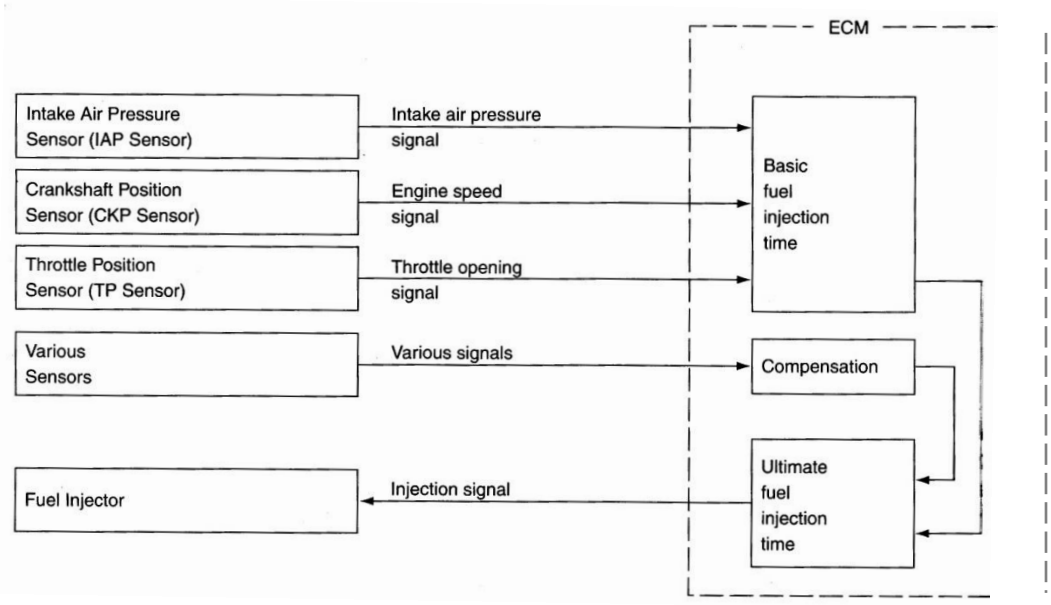


*Figure 6.* Suzuki RM-Z450 fuel injection mode of operation diagram (13)

Measurement and Modeling of Physical Geometry

An exterior parametric solid model of the engine was required to design a proper engine fixture and engine-dynamometer coupling for the test setup. The model needed to include all engine mounting locations, as well as the location of the transmission output shaft, engine crank shaft and engine starter shaft. The geometries of the combustion chamber, intake runners, and exhaust runners, which would also be necessary for three-dimensional CFD simulation, were available from a previous study (11).

To measure the physical geometry of the engine, an ATOS, high-resolution, non-contact structured light three-dimensional (3D) scanner was used. Multiple structured light bands or fringe patterns are projected from a central light source across the surface of the object being measured. Distortions of the fringe pattern caused by the three-dimensional features of the object are recorded by two equally-spaced cameras, angled 30 degrees inward from the centerline of the light source. The three-dimensional surface is then recreated within the processing software. In order to match the geometry as the camera is moved to different locations around the object, reference dots are randomly placed across the object surface. These dots are then recorded and triangulated to one another as the geometry and/ or camera is moved.

Once the exterior of the engine was scanned, a stereolithography (STL) graphics file was created and imported into solid modeling software (SolidWorks 2010). Additionally, the X, Y, Z, coordinates of critical geometry such as engine mounts, the kick start shaft, and crank shaft centerline relative to the end of the transmission output shaft were measured

within the ATOS software. The relative locations of the desired geometries were measured using best-fit planes and cylinders applied to the corresponding surfaces.

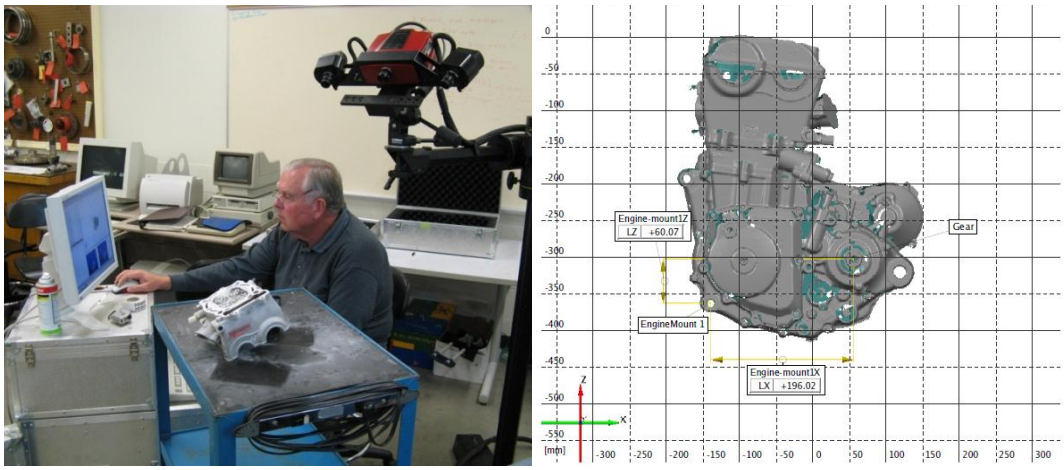


(A) (B)

*Figure 7*. ATOS scanner setup to scan cylinder head operated by Dr. Mitch Kiel of WMU(A) Example of scanned engine using ATOS software (B)

Design and Construction of the Engine Test Stand

To mount the engine, dynamometer, and sub-systems, a modular test stand was designed and built. The stand features T-slot extruded aluminum framing for the main framework and upper accessories mounts. This was chosen as it provided high adjustability when compared to a welded steel or aluminum box-tube design, which would require labor intensive modifications such as drilling of new holes or milling of new adjustment slots if components are changed. Figure 8(A) shows the engine and dynamometer attached to the main stand platform. The engine cradle and dynamometer mounting plate feature nine t-nut attachment points each, which ride in the three main frame rail slots. This provides a mechanism for adjusting the drive belt tension, and to properly align the engine output shaft and dynamometer input shaft. The engine cradle and dynamometer

mount plate were attached on common rails to enable direct transfer of torque between the engine and dynamometer. Figure 8(B) shows the completed test stand, including the lower and upper structure for mounting engine accessories, the integrated fuel system, and sensor package.

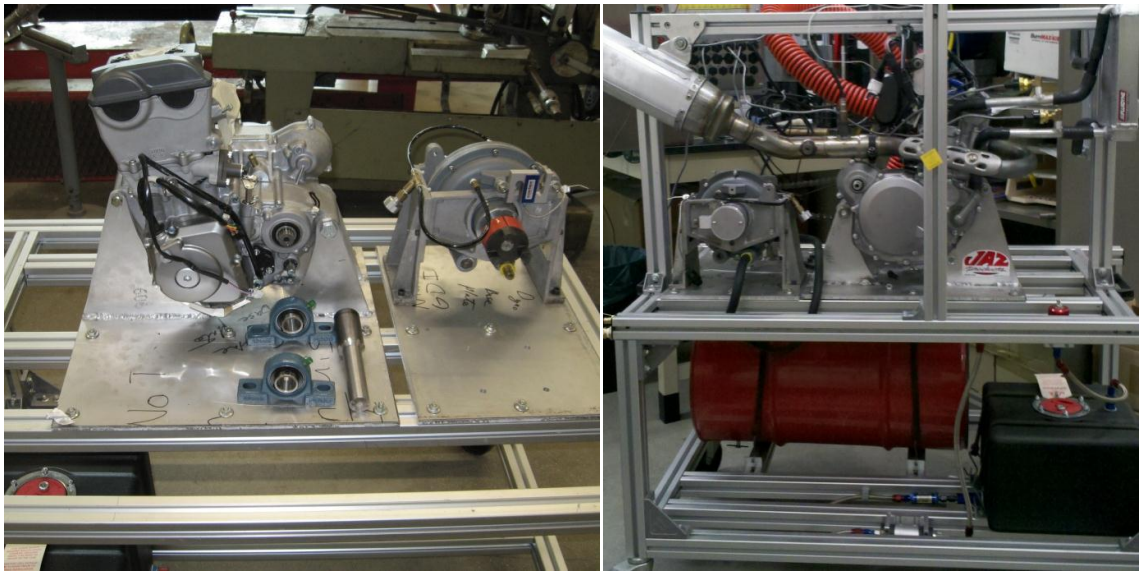

(A) (B)

*Figure 8.* Engine cradle assembly and dynamometer mounting plate (A), Test stand frame work with engine, dynamometer and accessories mounted (B)

The engine was coupled to a water-brake dynamometer (Go Power Systems' D-100). This dynamometer has a maximum power rating of 75 kW (100 HP), maximum torque of 88 Nm (65 lbf-ft), and maximum speed of 14,000 RPM. As illustrated in Figure 9, there is a 2.39:1 gear reduction within the integrated transmission, such that the torque at the engine output shaft is 2.39 times higher than the torque at the crankshaft. As illustrated in figure 3, if the engine were directly driven off the output shaft (i.e., after the transmission), the output power and torque would fall outside the capacity of the dynamometer. To remedy this problem, a synchronous belt drive system with 1:2.41

ratio was implemented. As illustrated in Figure 10(A), the belt drive shifted the output power curve to remain within the capacity of the dynamometer.

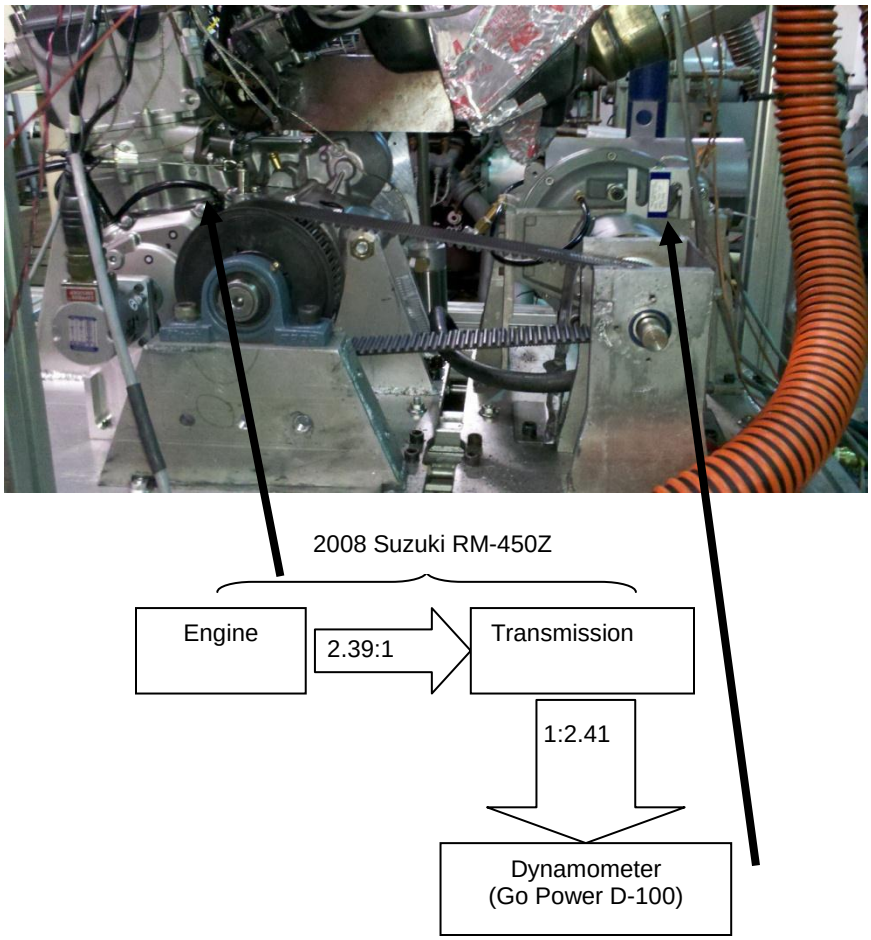


*Figure 9*. Schematic of the belt drive connection implemented to benchmark the 2008 Suzuki RM-450Z engine.

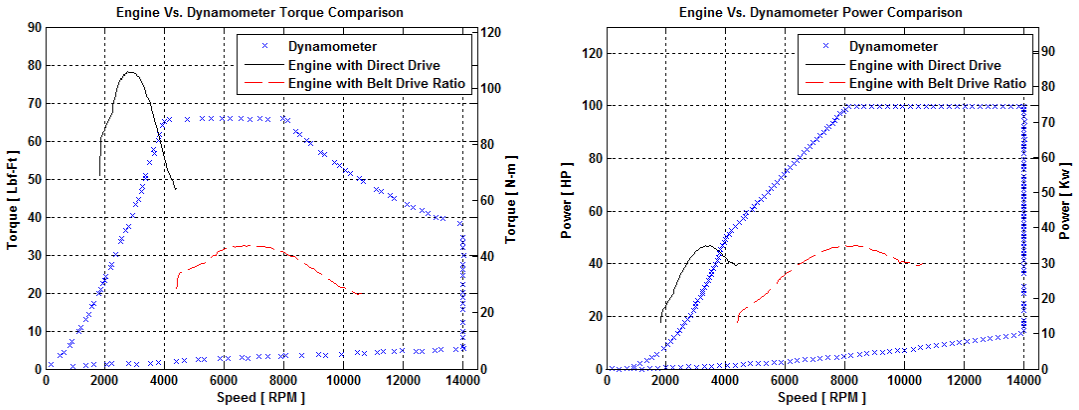


(A) (B)

*Figure 10*. Comparison of dynamometer torque (A) and power (B) capacity (crosses) to engine output with direct drive (solid line) and torque-reducing belt drive (dashed line)

The ATOS scan yielded motor mount locations relative to the transmission output shaft. This information was used to design an engine cradle. The cradle enables rigid mounting of the engine, output shaft bearing supports, optical encoder, and belt tension adjuster. The dynamometer mount plate served as common surface for the Go-Power D100 dynamometer and dynamometer input shaft bearing supports. The cradle and dynamometer mount plates were designed in SolidWorks and constructed in house out of 3/8 plate 6061 aluminum. The cradle utilizes the three lowermost engine mounts, with the two forward mounts featuring 10 mm hardware and the rear most mount featuring 16 mm hardware. In order to drive the belt pulley, a one-inch diameter steel output shaft with a 1/4 inch keyway was designed and built. A splined ring matching the splines of the engine output was welded into the engine end of the shaft. This end of the shaft was supported by the engine output shaft bearing integrated into the engine case; while the opposite end was supported by a one-inch bore pillow block bearing and support. A rendering of the final engine cradle assembly is shown in Figure 11(A).

The dynamometer mounting plate featured a hardened steel, 3/4 inch diameter input shaft with 3/16 inch keyway. Aluminum bearing supports with 3/4 inch bore sealed ball bearings were used to maintain the input shaft at the same position as the dynamometer connection. The input shaft and dynamometer were coupled through a Love-Joy L-100 flexible jaw coupling with Hytrel® insert as recommended by the dynamometer manufacturer. This enables dampening of high-magnitude output torque pulses from the engine and accommodates slight misalignment between the dynamometer and input shaft. It was found, however, during testing that the Hytrel® inserts degraded quickly, and for future testing a new type of coupler (not developed as part of this work) is suggested. Figure 11(B) shows the dynamometer mounting plate and assembly relative to the engine cradle assembly.

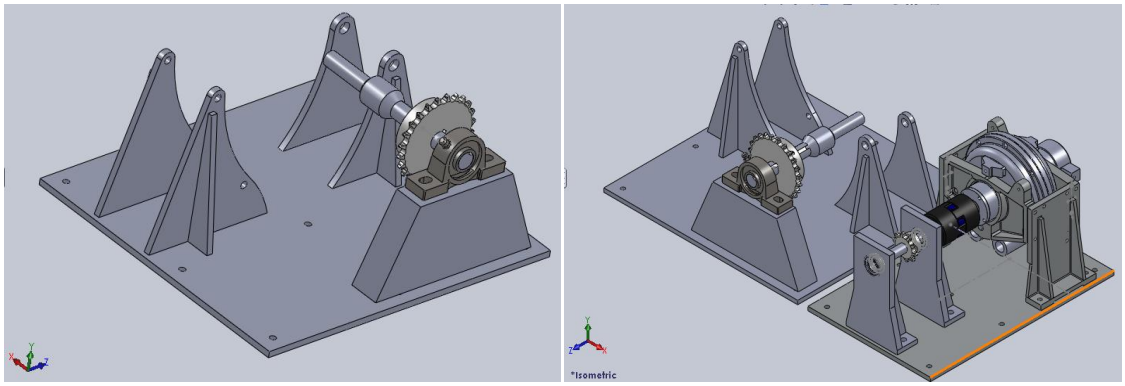


(A) (B)

*Figure 11*. Engine cradle, output shaft, and bearing/support assembly (A). Engine cradle assembly, dynamometer mounting plate, dynamometer, and dynamometer input assembly (B)

Fuel and Intake-Air Systems

An integrated fuel supply system was also designed for the test stand. The system featured a five-gallon fuel cell, Aeronautical and Navy (AN) -4 plumbing with a 85 micron pre filter (Earls 230204ERL), a 190 L/hr electronic fuel pump (Walbro GSL394), 35 micron main filter (Earls 230104ERL), and 40-75 psi adjustable fuel pressure regulator (Aeromotive 1309). A schematic of the system is shown in Figure 12. The maximum flow capacity of the fuel pump, fuel pressure adjustability, and use of easily reconfigured, AN plumbing, enables testing future engine configurations, which may require a fuel supply pressure as high as 70 psi.

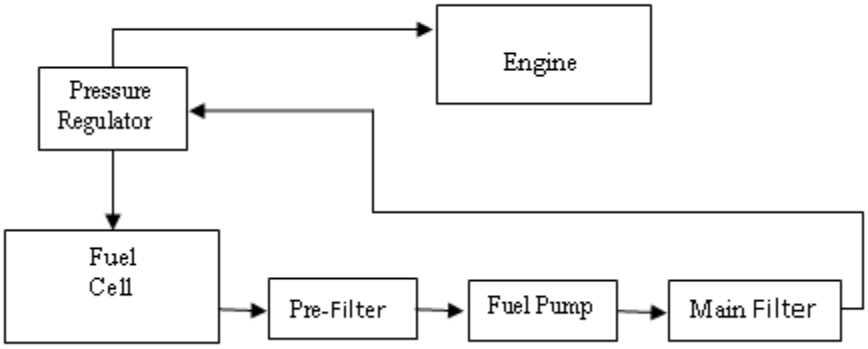


*Figure 12*. Fuel system schematic

A 66-liter (17gal) intake air plenum was also implemented in the test stand. This was done to prevent saturation of air flow measurement devices due to high amplitude intake-air flow pulses associated with single-cylinder engines. The plenum mechanically averages these pulses by providing a large volume of air for the pulses to dissipate. It featured a single inlet connected to the flow sensor and single outlet connected to the engine. The main inlet to engine air box and all secondary inlets were sealed using a sheet metal cap to ensure that the intake air completely passed through the plenum. A

single, two-inch diameter inlet was cut in the cap. The plenum and air box were then connected with a two- inch diameter hose. A schematic of the intake air system is shown in Figure 13.

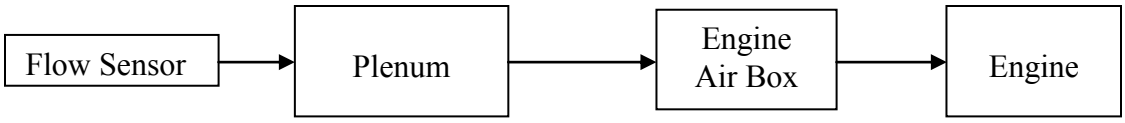


*Figure 13*. Schematic of the intake air flow path

As the stock application for this engine does not feature electric start, but a rider-actuated kick start, a pneumatically-actuated kick starter was designed and implemented with an operator controlled electronic pneumatic valve. This was needed to start the engine from the control room to comply with safety regulations. To quantify the torque required to start the engine, the kick start was rotated at approximately the starting speed, while the peak torque was measured with a beam style torque wrench Figure 14 (A). A peak torque of 75 ft-lbf was measured. A two- inch diameter, twelve-inch stroke, dual-action, pneumatic cylinder (Humphrey 4-DP) was selected to provided starting force. A seven-position adjustable lever arm and cylinder mount were also designed with a torque arm range of 4 to 8.5 inches in 3/4 inch increments. The cylinder was positioned to actuate the torque arm in the retraction direction. With an operating pressure of 100 psi and a piston area of 2.79 $in^2$ in retraction, a force of 279 lbs was available from the pneumatic cylinder. This resulted in peak torques between 99 and 210 ft-lbf. During initial testing, it was found the third position at 5.5 inches and a resulting peak torque of 136 ft-lbf provided adequate starting capacity. In order to provide adequate air pressure throughout

the stroke of the pneumatic cylinder, a five gallon storage reservoir was installed prior to the electronically actuated pneumatic valve. The complete starter assembly is shown in Figure 14 (B).

(A) (B)

*Figure 14*. Starting torque measurement setup (A). Assembled pneumatic starter (B)

Cooling System

Initially, the motorcycle's water-to-air heat exchanger, shown in Figure 15 (A) and an electric fan were selected to control engine coolant temperature. The electric fan was controlled remotely using an electric relay through a LabVIEW interface. When the engine temperature exceeded a user-specified temperature, the fan was turned on until the engine temperature was brought below the desired set point. During initial testing, this

setup was found to prevent the engine coolant temperature from increasing beyond the pre-set value, but at the expense of creating excessive overshoot around the desired set point. This problem is illustrated in Figure 15 (B), which shows the radiator inlet temperature, outlet temperature, and specified set point temperature during a four-minute test period. For this test, the engine was operated with no load, at idle (approximately 2,000 RPM), and with a coolant temperature set point of 165°F. An average, maximum, and minimum radiator inlet temperatures of 159°F, 166°F, and 152°F, respectively, were observed. This high fluctuation was determined to be unacceptable to accurately quantify coolant load.

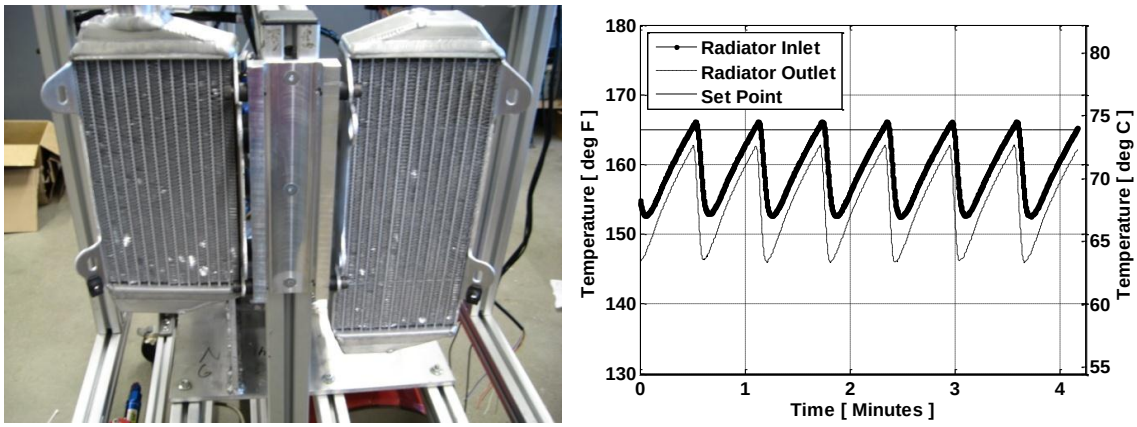


(A) (B)

*Figure 15*. Air-to-water heat exchangers (A). Engine temperatures during initial testing (B)

In order to more accurately control engine temperature, a water-to-water, shell-and-tube heat exchanger was designed and built. The cooling water available in the engine dynamometer test cell at a temperature of 65°F was used as the cooling fluid. The core of the heat exchanger consists of 25, 3/8-inch outer diameter copper tubes nine inches long, arranged in a square-pitch pattern. The shell is four inches in diameter and featured three equally-spaced baffles. The completed core is shown in Figure 16 (A). The engine

cooling water passes through the tube side of the exchanger, while the building cooling water passes through the four-inch diameter shell. The completed heat exchanger is shown in Figure 16 (B).

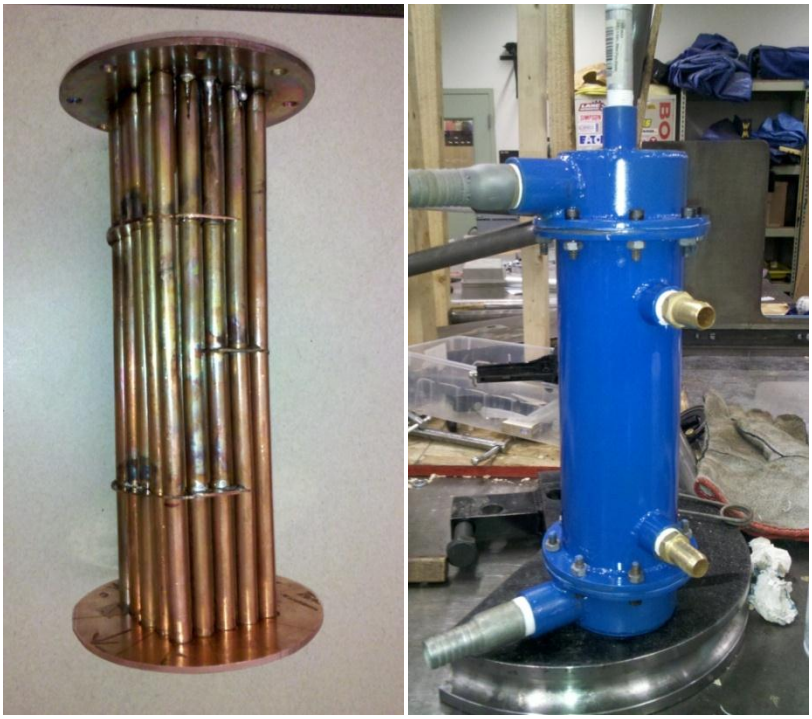

(A) (B)

*Figure 16*. Heat exchanger tube core (A), Completed heat exchanger (B)

To control the engine coolant temperature at the user specified set point, the amount of energy transferred between the building-supplied cooling water and engine cooling water was varied by controlling the flow of building cooling water. This was accomplished through the use of a brass barrel valve placed in line with the cooling water supply line. The barrel valve opening position was controlled by an attached stepper motor and driver. The stepper motor allowed for the valve to be adjusted from closed to full-open in 40 steps. The stepper motor was driven by a transistor-transistor-logic (TTL) input provided by the data acquisition system's digital output. A LabVIEW program was developed to

generate the output signal. As no position feedback was available from the valve, the LabVIEW program was required to keep count of the steps to determine the current position. Upon starting the program, the valve was driven the maximum 40 steps in the closed direction to ensure the valve was fully closed. At this point, the current step count was set to zero. The counting was done within a while loop with a user-defined time delay per iteration. The valve actual position was compared to the desired position (labeled Cooling Position on the LABVIEW interface) and an error value was determined. If the error value was positive, the valve was stepped open that number of steps. The error value was added to the current position to determine the new position. If the error value was negative, the valve was stepped closed the required number of steps and the negative error value was added to the current position. If the error value was zero, nothing was done. This new position was carried to the next iteration through the use of a shift registry and saved as the new current position. The valves position can be manually controlled through a slider on the main LabVIEW-based user interface.

A proportional-integral-derivative (PID) control algorithm was implemented to automatically control the coolant temperature. The current engine coolant temperature was monitored and compared to the user determined set point. Based on whether the error between these values was positive or negative, the magnitude of the error, and its rate of change, a new valve position was determined. The PID gain values were tuned experimentally, and the values of P gain, I gain, and D gain were found to be -2.0, -0.06, and -0.01, respectively. The developed LabVIEW code is shown in Figure 17. It was

found during testing that the setup was able to control temperature to within 2.6°F of the specified set point.

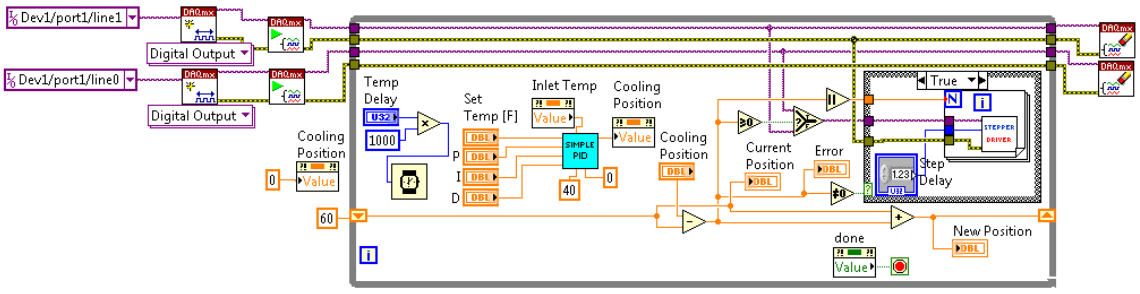


*Figure 17*. LabVIEW code for controlling coolant temperature.

Throttle and Load Control Systems

Remote engine operation was required to comply with safety requirements. To control the throttle position remotely, a Land and Sea Auto Throttle Servo was selected, as shown in Figure 18. This servo featured adjustable stops for initial and end position, as well as adjustable motion ratio. These features facilitated variable adjustment of travel and actuation force. The actuator featured a stepper motor and built-in stepper driver with TTL input for position control. Similar to the cooling water control valve, the necessary TTL input was provided by the digital output from the data acquisition card. As shown in Figure 19 (A), a LabVIEW program was developed to generate an output signal similar to that used for the coolant temperature control. The user specifies the desired step position through a slider on the front panel, shown in Figure 19 (B) with a range of o to 360 steps representing closed to wide-open throttle, respectively. The actual throttle butterfly position was measured directly and displayed on the front panel. It was

found during testing that the system enabled throttle position control to within 1% of the desired set point.

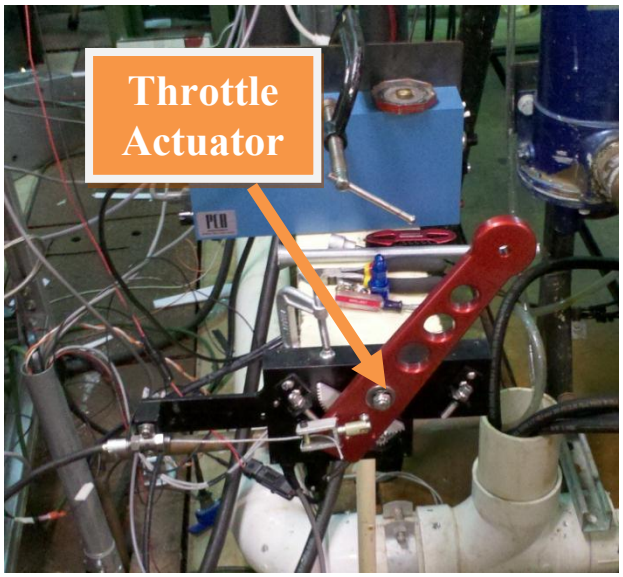


*Figure 18.* Electronic throttle actuator

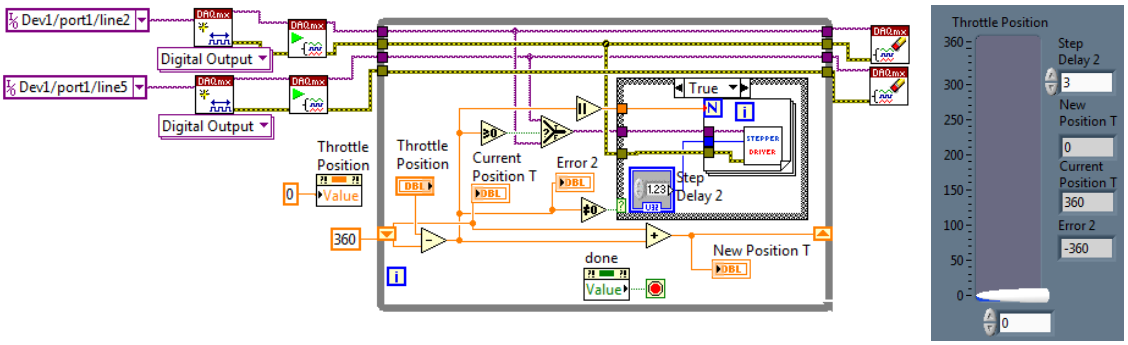


(A) (B)

*Figure 19.* LabVIEW Code throttle actuator (A). Throttle Position User interface (B)

The engine load was controlled using manually-actuated (coarse and fine) water valves supplied as part of the water brake dynamometer package (Figure 20). Water was supplied through an independent building supply. The resistant torque on the engine was varied by varying the flow of water into the dynamometer through the load-control valve(s).


*Figure 20.* Go-Power systems load-control valves

## 2.4. INSTRUMENTATION AND DATA ACQUISITION

### Sensor Overview

One of the main goals when instrumenting the engine was to minimize engine modifications. Once performance and efficiency metrics were defined (see sections 2.1 and 2.2), a list of parameters to be measured and corresponding sensors was developed. This list is shown in Table 3.

*Table 3.* Parameters to be measured and required sensors

| Parameter | Sensor Type |
|---|---|
| Engine speed | Optical encoder |
| Engine crank angle | Optical encoder |
| Throttle position | Throttle position sensor |
| Air-to-fuel ratio | Wideband oxygen sensor |
| Flow rate | |
| Coolant | Turbine flow meter |
| Fuel | Piston flow meter |
| Intake air | Mass air flow meter |
| Pressure | |
| Combustion chamber | piezoelectric pressure- measuring spark plug |
| Intake air, exhaust, fuel, radiator (inlet/outlet), dynamometer water inlet, engine oil | Pressure transducer |
| Temperature | |
| Intake air, exhaust gas, engine oil, fuel, radiator (inlet/outlet), cylinder wall, dynamometer water (inlet and outlet) | K type thermocouple |
| Test cell relative humidity, dew point, temperature, barometric pressure | Barometric pressure, temperature, and humidity transmitter |

In-Cylinder Pressure Transducer

The combustion chamber was instrumented with a piezoelectric pressure transducer integrated into the spark plug (Kistler model 6113BFD35Q04A41), coupled to a charge amplifier (PCB model 462A) which enabled measurements of the in-cylinder pressure with one-half crank angle resolution. Because this sensor was integrated into a spark plug matching original equipment manufacturer (OEM) specifications, no modifications of the cylinder head were necessary. Before installing the sensor, a dynamic calibration of the amplifier was conducted. The pressure transducer was installed in the spark plug port (Figure 21 B) of a 1967 Cooperative Fuel Research (CFR) engine (Figure 21 A), while an analog compression gauge was installed in the CFR engine's test port (Figure 21 C).

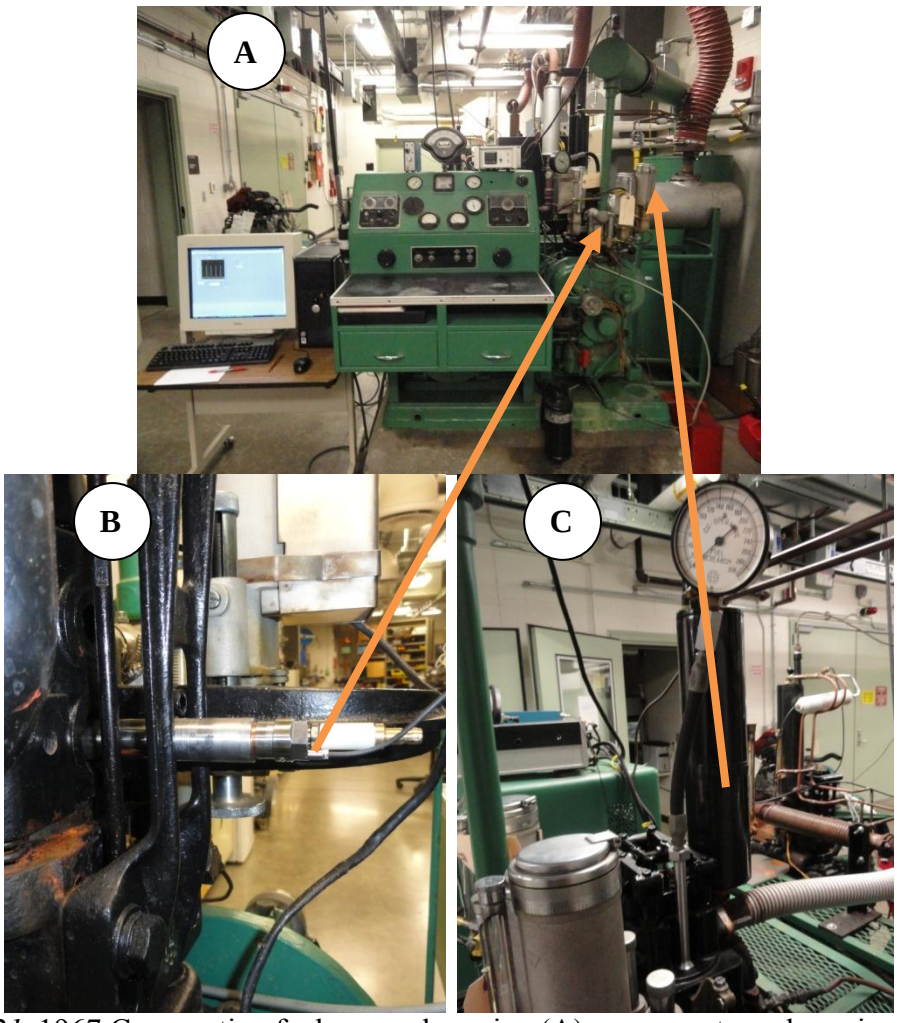


*Figure 21.* 1967 Cooperative fuel research engine (A); pressure transducer installed in spark plug port (B); analog pressure gauge installed in test port (C).

The charge amplifier output signal was connected to a National Instruments SCB-68 shielded I/O connector block, which was in turn connected to a National Instruments NI PCI-MIO-16E-4 (NI 6040E) data acquisition card. The CFR engine was motored at 600 RPM. The signal was sampled at 7.2 kHz and 7,200 samples were recorded. In order to time data acquisition with piston position, sampling was triggered on the compression stroke when the in-cylinder pressure exceeded 40 psi. This allowed for five complete cycles to be sampled with half- a-degree crank angle resolution. The pressure curves had

to be "shifted" to an appropriate reference value. As the CFR engine is un-throttled, manifold pressure during the intake stroke was assumed to 100 kPa. The index during the intake stroke when the intake manifold pressure was equal to the measured in-cylinder pressure was selected. The pressure reading at that index was used as a reference to shift the pressure at that index to 100 kPa. The LabVIEW front panel is shown in Figure 22 (A). It displays the referenced index (highlighted in yellow) and example readings for maximum pressure, minimum pressure, percent error, and the input of analog peak pressure reading. The LabVIEW code is shown in Figure 22 (B).

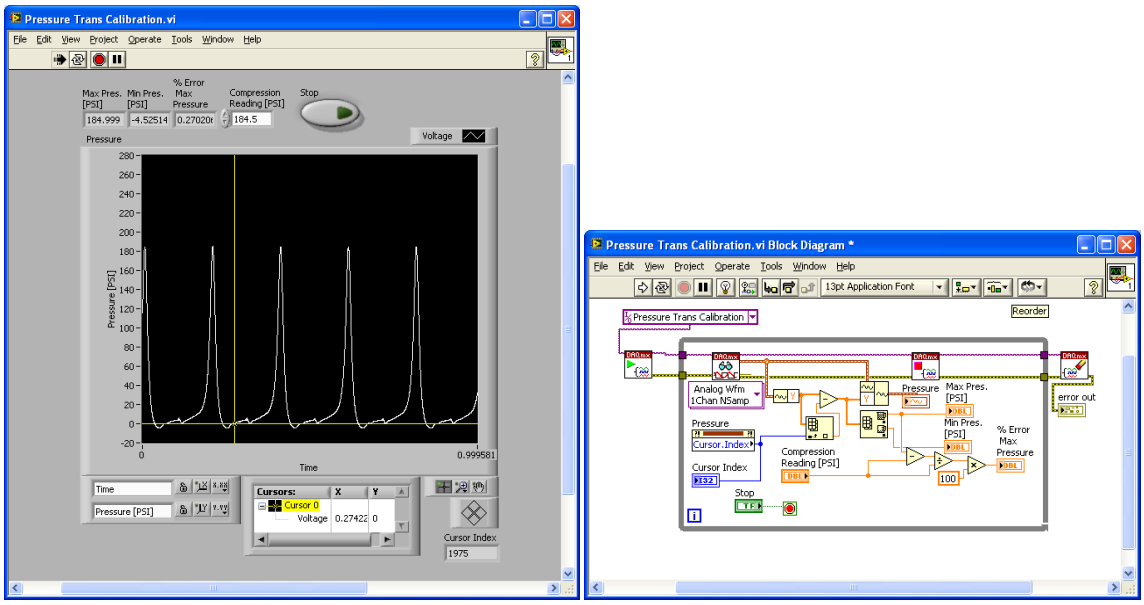


(A) (B)

*Figure 22.* LabVIEW Front Panel with Pressure readings (A), LabVIEW code (B)

To begin the test, an initial charge amplifier setting was calculated using the calibration sheet for the Kistler transducer. This was based on an approximate full-scale voltage of 9.98 volts, corresponding to a full-scale reading of 15 MPa (2,175 psi). The engine was then motored without fuel or ignition at a specified compression ratio. The scaled

amplifier output was compared to the compression gauge reading. The amplifier setting was then adjusted until the scaled amplifier output was in agreement with the measured compression gauge reading. The calibration was performed for compression ratios ranging from 5.29:1 to 11:1 (micrometer reading of 0.150 inches to 0.750 inches). The results, shown in Figure 23, illustrate excellent agreement between the output of the piezoelectric transducer-charge amplifier system and the reference measurement over the tested range of compression ratios. Once calibrated, the pressure transducer was installed in the RM-450Z engine to record in-cylinder pressure data.

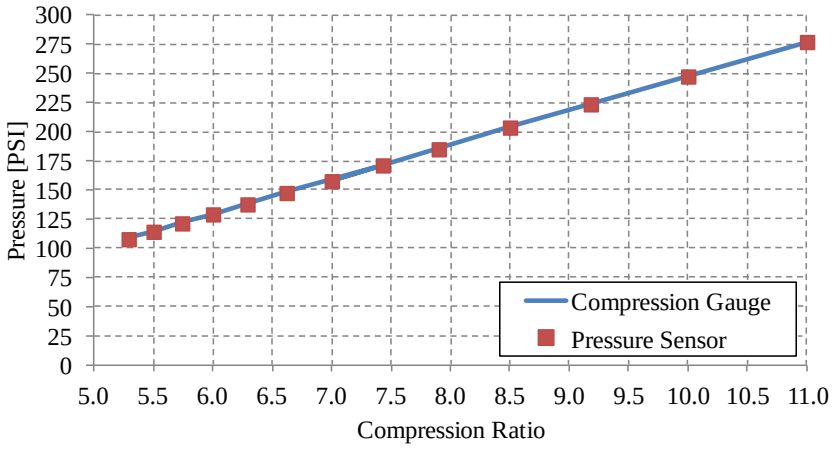


*Figure 23.* Calibration curve of in-cylinder pressure transducer

Additional Pressure Sensors

Pressure sensors (Omega model PX181B-060C5V) were installed to monitor the intake and exhaust pressures, as well as the pressure at the inlet and exit ports of the radiator. A pressure sensor (Omega model PX181B-100G5V) was also installed at the dynamometer inlet in order to monitor the supply-water pressure. Fuel and oil pressures were monitored with Omega model PX181B-100G5V pressure sensors.

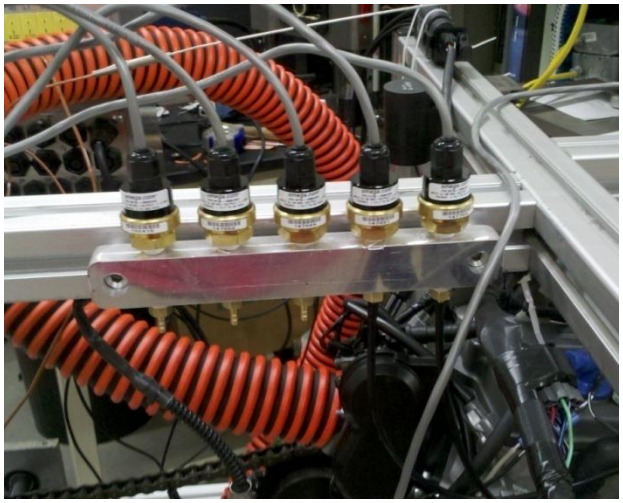

*Figure 24:* Remote pressure sensor packaging

Temperature Sensors

The intake and exhaust (Figure 25D) systems were instrumented with 1/16 inch, K-type thermocouples (Omega model TJ36). Additional thermocouples were used to monitor fuel (Figure 25B) and oil temperatures (Figure 25E), as well as the coolant temperature at the inlet and exit ports of the radiator (Figure 25C). Thermocouples were also installed to measure the temperature of the dynamometer water at the inlet and exit ports (Figure 25A) to comply with dynamometer operation guidelines.

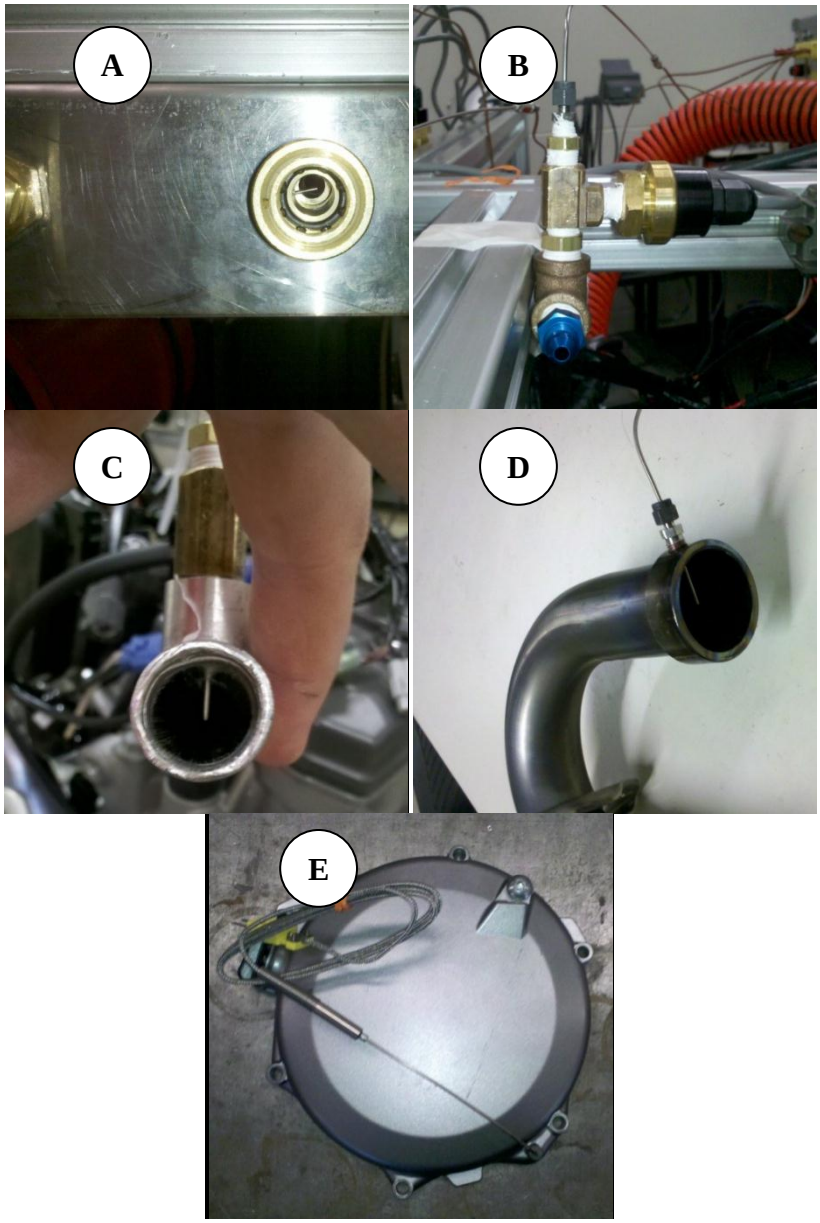


*Figure 25.* Temperature sensor locations: dynamometer water (A), fuel (B), engine cooling water (C), exhaust gas temperature (D), oil temperature (E)

Boundary Temperatures

To measure boundary temperatures in support of ongoing simulation efforts, four surface K-type thermocouples (Omega model SA1XL-K) were placed centered on the top left, top right, bottom left, and bottom right quadrants of the intake port. The top left and top right positioning are shown in Figure 26(C). A single surface K-type thermocouple (Omega model SA1XL-K) was also placed centered on the left quadrant of the exhaust port, shown Figure 26(B). To measure the cylinder wall temperature, three 1/6 inch, K-type thermocouples were installed in the lower flange of the cylinder. This lower flange is located 1.5 inches (38.1 mm) from top surface of the cylinder. This location is also approximately one inch (25.4 mm) above the piston face at bottom dead center based on the engine stroke of 2.445 inches (62.1 mm). A 1/16 diameter hole was drilled in the solid flange, centered between the base of the flange and the bottom of the cooling jacket. The hole was drilled to depth that allowed the tip of the thermocouple probe to be in contact with cylinder wall, as shown in Figure 25 (D). These thermocouples were placed in the forward, right, and rear quadrants of the cylinder, as shown in Figure 26 (E).

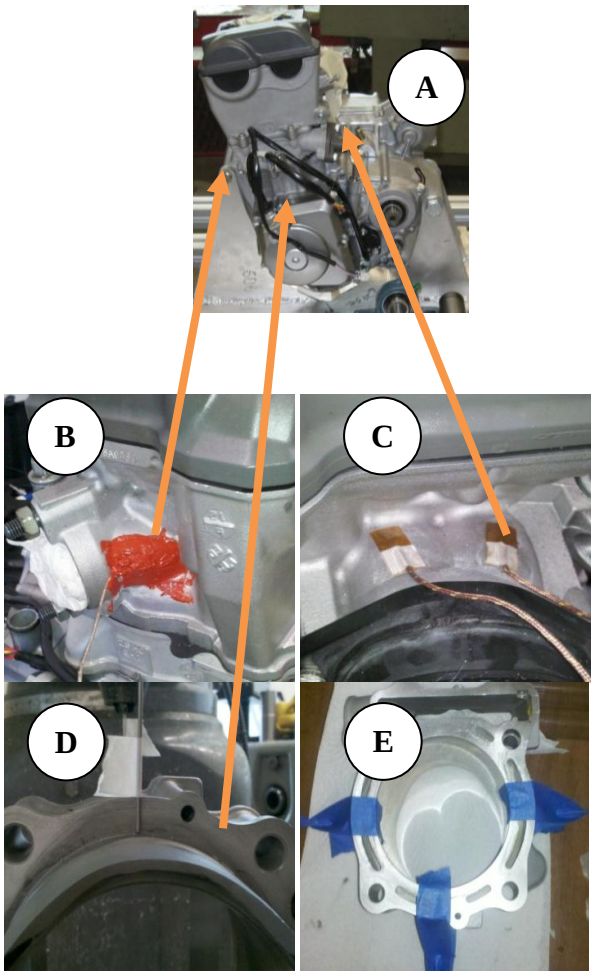


*Figure 26.* Installation location of surface thermocouples. Engine left side view (A), exhaust port left quadrant (B), intake port top left and right quadrant (C), cylinder wall sensor depth (D), cylinder wall sensor location (E).

Flow Sensors

The engine was also instrumented with flow sensors to monitor the volumetric flow rate of coolant (Omega Model FTB-1424) and fuel (Max Machinery model 213), as well as the volumetric flow rate of the intake air (Ford model XTP49526). The volumetric flow sensor output was calibrated using a Super Flow model 110 flow bench, shown in Figure 27. As part of the calibration procedure, the volumetric flow rate was varied from 0 to 157 cubic feet per minute (4.45 $m^3$/min) while recording the voltage output of the sensor. This test was repeated twice, the data points were averaged, and a third-order polynomial curve was fit to the data. This function was then used to physically scale the signal within in the data acquisition setup. The results of the calibration and curve fit are shown in Figure 28.


*Figure 27.* Flow sensor calibration setup using a flow bench

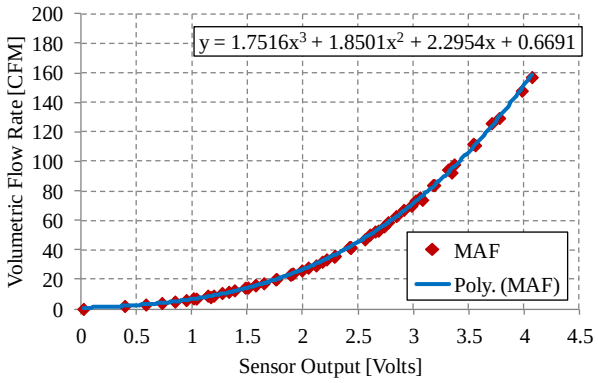


*Figure 28.* Calibration curve of the intake air flow sensor used for engine benchmarking

Speed, Position, and Torque Sensors

In addition to pressure, temperature, and flow sensors, an optical encoder (BEI Model H25) was installed directly on the crankshaft through the stator/timing cover access port. This location allowed the encoder to be driven off the stator retaining nut attached to the crankshaft without any modification to the crankshaft or engine cover. The encoder, which measured crank angles at one-half degree resolution, was used to synchronize the piezoelectric pressure transducer with the piston position throughout the engine cycle. Signals from the encoder were also used as a secondary measurement of engine speed. Throttle position was measured using the stock sensor, mounted on the engine's throttle body. The air-to-fuel ratio was monitored using a wideband oxygen sensor (Innovate model LC-1). The sensor was installed in the exhaust, just upstream of the muffler. As this sensor is not part of the fuel injection system, it operated in open-loop mode. The pressure, temperature and relative humidity of the engine test cell were monitored with a probe and transmitter unit (Omega model IBTHX-W-5). Ambient humidity, temperature and atmospheric pressure remained consistently at 22.5%, 22°C (71°F), and 984 mbar, respectively, throughout the course of the experiments.

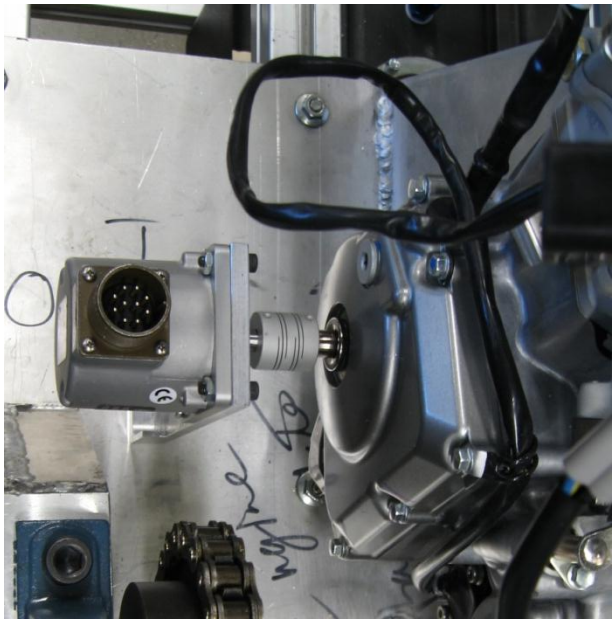

*Figure 29.* Optical encoder mounting location

The load cell and a sixty-tooth wheel with magnetic pickup provided as part of the dynamometer package were used for measuring torque and speed, respectively. The signals were conditioned using the Go-Power systems DC-200 unit to obtain dynamometer speed, torque, and power. These signals were routed to a computer through a serial communication port. The dynamometer speed was used as the primary measurement of engine speed, as the signal proved to be more stable than the output from the crank angle encoder, which varied by ±50 RPM. Although small, a correction for the difference in gear ratios (1:1.02) was applied to the dynamometer speed and torque to relate it to the engine quantities.

Sensor Connections and Data Acquisition

A National Instruments (NI) PCI-6251, 16-Bit, high speed (1 MS/s[1]) data acquisition card was used throughout the experiments. Sensors were connected to a universal interface panel, shown in Figure 30(A). This panel featured connections for 24 k-type thermocouple mini connectors, 12 five-wire sensors, 12 four-wire sensors, two six-wire sensors, one eight-wire sensor and ten 12 volt power sources. The panel was connected to a boom movable within a three-foot radius from the main connection box. The variety of available connections and position adjustability of the box were purposely designed into the system so that it can be later used in a variety of test setups. These connection points were then wired into the SCXI chassis and connection blocks, housed in a single stainless steel enclosure, as shown in Figure 30(B). Thermocouple signals were connected to a NI SCXI-1102, 32-channel thermocouple/voltage input module, through a NI SCXI-1303 terminal block. This module was also used to collect voltage signals from the pressure transducers (excluding the in-cylinder pressure data), flow sensors, and the throttle position sensor. The SCXI-1102 module was installed in a SCXI-1000 chassis and multiplexer. All other voltage inputs (oxygen sensor and in-cylinder pressure), counter/timer inputs (optical encoder), and digital signals from the throttle and engine coolant temperature controllers were connected through a NI CB-68LPR connector block. A SCXI-1346 multi chassis adapter was used to connect both the SCXI-1000 chassis and CB-68LPR to the PCI-6251 data acquisition card.

[1] One million samples per second

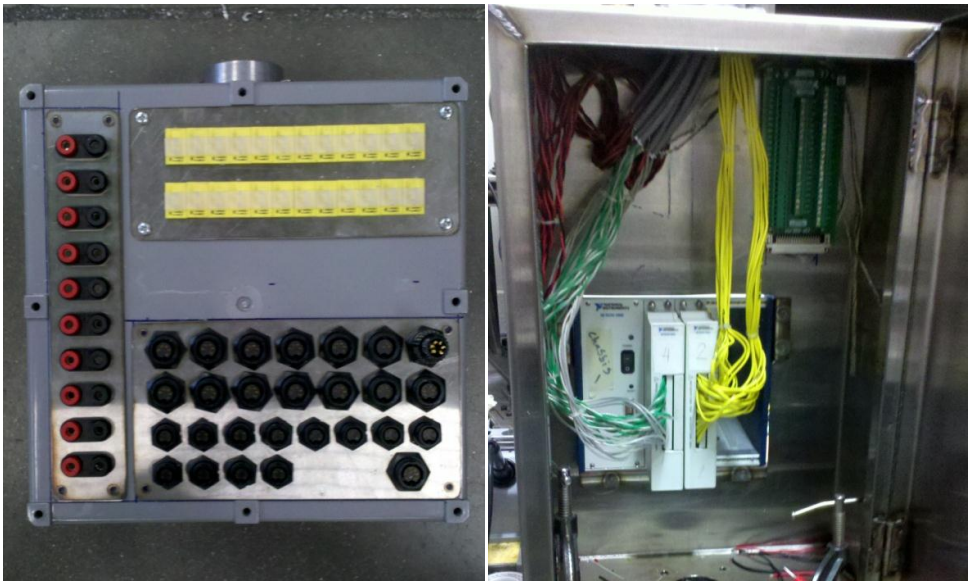

(A) (B)

*Figure 30.* Sensor connection panel (A), SCXI chassis and connector block (B). Both systems were developed in-house by the author.

Dynamometer torque, power, and speed were acquired and conditioned through the Go-Power systems DC-200 unit, which interfaced with the computer through a serial communication port. The test cell conditions, measured using an IBTHX-W-5 sensor system, were acquired via a network Ethernet connection.

User Interface

A LabVIEW-based user interface was developed to enable user input for throttle position and engine coolant temperature set points, real-time monitoring of all the instrumented systems, and triggering of data acquisition. The user interface, shown in Figure 31, was developed in LabVIEW to monitor general engine performance parameters and acquire the experimental data remotely. Using this interface, the user is able to specify the number of samples. The file naming convention is of the form

(GDI_EngineSpeed_XXXX_Throttle_Position_ XX), based on the engine speed and throttle position of the first recorded sample.

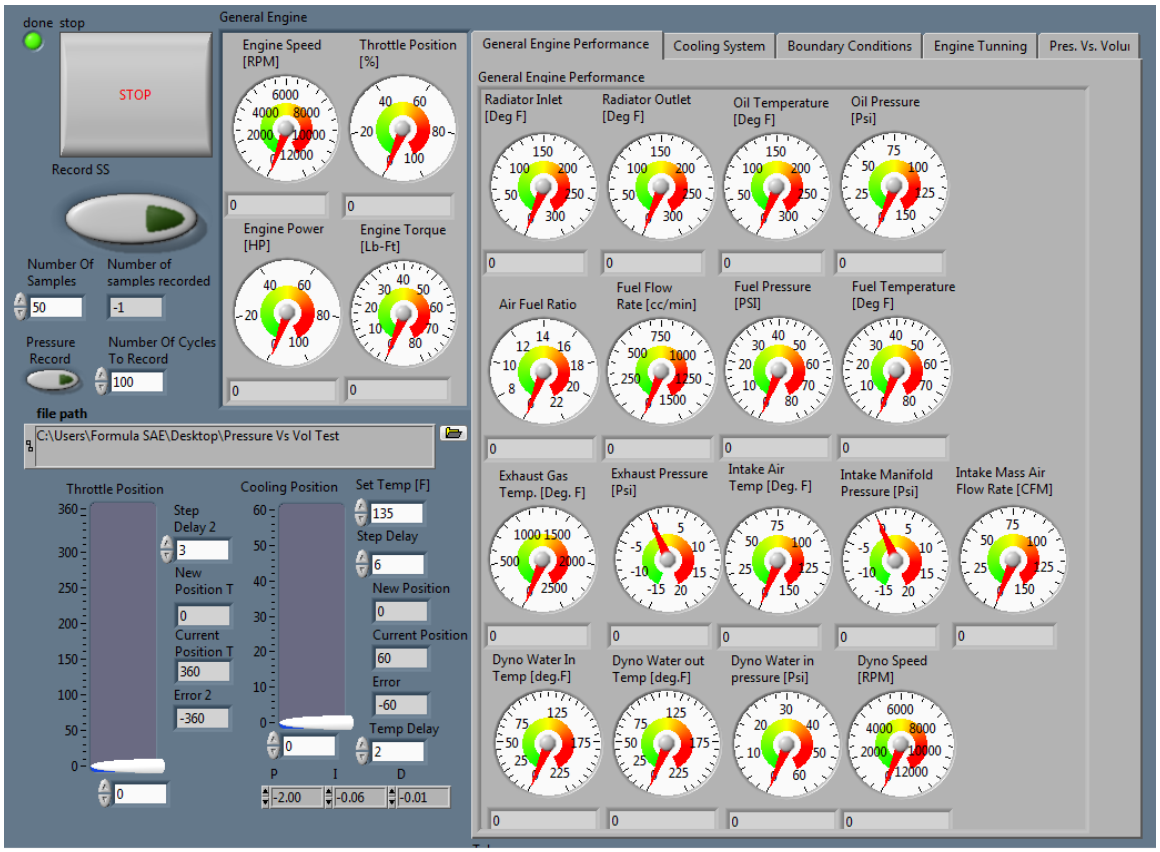


*Figure 31*. In-housed developed LabVIEW user interface

## 2.5 Test Plan, Data Collection and Post-Processing

Experiments were conducted at 30, 50, 65, 80, and 100% throttle openings. At each throttle position, the engine speed was swept from 4,000 RPM to 9,500 RPM in 500 RPM increments. At the beginning of the tests, the engine was allowed to idle with the transmission disengaged until the coolant temperature reached 74°C (165°F). After completing the warm up process, the throttle was set to the desired set point. The engine was loaded by controlling the rate of water flow through the dynamometer until a steady

speed of 4,000 RPM was reached. At this point, the load was decreased in order to increase the engine speed from 4,000 to 9,500 in 500 RPM increments. The engine was allowed to stabilize to within ±1 RPM, as indicated by the D200 dynamometer speed readout, before initiating data collection. The uncertainty in the encoder measurement of engine speed was larger (±50 RPM). The larger error might be attributed to the higher sampling rate (720 samples/engine revolution as a function of engine speed) compared to the 100 Hz sampling rate of the D200 unit. This higher sampling rate resolves small fluctuations in engine speed. This error was acceptable, as natural cycle-to-cycle variations can cause these fluctuations, but overall the engine operated steadily. At each test point, data were sampled at 1 kHz over the course of 50 seconds. One-hundred samples were averaged every second, yielding 50 data points per test condition. The in-cylinder pressure was measured at every half crank angle over 100 cycles, regardless of engine speed. The mean in-cylinder pressure trace was, therefore, generated using a one-hundred sample average at each half crank angle.

The experimental data were processed using Microsoft Excel and MATLAB. For the steady state data, the LabVIEW-generated CSV files were exported into Excel. A fifty-sample average was generated for each test condition. The averaged values were then organized in a single spreadsheet as a function of throttle position. The steady state performance and efficiency parameters described in sections 2.1 and 2.2 were then calculated. In order to generate graphical representation of the data, a MATLAB program was developed to read the summary file, make any additional calculations or unit conversions, and graph the appropriate quantities.

The in-cylinder pressure data were also post processed through MATLAB. The program allowed the user to select the desired CSV file and input the engine speed and throttle position, as shown in Figure 32. The program then used the trapezoidal numerical integration function in MATLAB to determine the area under the intake, compression, expansion, and exhaust strokes from the pressure-volume diagram. The algorithm was tested on a sine function using an amplitude of one and a period of zero to pi in 360 steps. The trapezoidal integration predicted the area to equal two (i.e., the known solution). Results were used to quantify gross and net indicated work (equation 4) and power (equation 5), gross and net indicated mean effective pressure (equation 7), as well as the magnitude and location of peak pressure. These parameters were automatically recorded in a new CSV file and saved with a file name corresponding to the user-specified engine speed and throttle position.

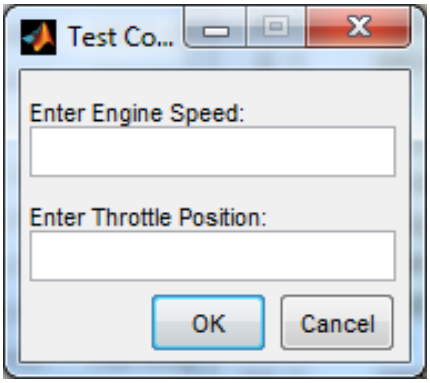


*Figure 32.* MATLAB pressure data processing input screen

# CHAPTER 3

# ENGINE BENCHMARKING RESULTS

## 3.1 Overview

This chapter will describe results of the experiments conducted to benchmark the Suzuki RM-Z450 engine. The chapter begins by summarizing ambient conditions during testing (Section 3.2), and follows with a discussion of the engine operating and boundary conditions during testing (Section 3.3). Finally, engine performance and efficiency data are discussed in Sections 3.4 and 3.5, respectively.

## 3.2 Ambient Test Conditions

Ambient conditions in the test cell were monitored throughout the experiments. Results, presented in Table 4, show that the measured values fall within the acceptable range of dry air pressure and temperature specified by SAE standard J1349 (14) and shown in Table 5. A correction factor for the engine output power, also based on SAE standard J1349 for wide-open-throttle operation, can be calculated from the measured and standard ambient test conditions according to equation 16. Here $p_{s,d}$ is the standard dry pressure, $p_m$ is the measured atmospheric pressure, $p_{v,m}$ is the measured water vapor pressure, $T_m$ is the measured temperature, and $T_s$ is the standard temperature. For this test, it was found that incorporating the correction would modify the measured power by a factor of 1.007. This effect is negligible and, as a result, the correction was not applied to the experimental data

$$C_F = 1.18\left[\frac{p_{s,d}}{p_m - p_{v,m}}\left(\frac{T_m}{T_s}\right)^{1/2}\right] - 0.18 \qquad [16]$$

*Table 4*.Measured ambient test conditions

| Measured Ambient Test Conditions | | | | |
|---|---|---|---|---|
| **Humidity** | **Water Vapor Pressure** | **Dew Point** | **Temperature** | **Atmospheric Pressure** |
| % | inHg | °F | °F | inHg |
| 22.5 | 0.17 | 31.10 | 70.70 | 29.05 |
| | mmHg | °C | °C | mmHg |
| | 4.42 | -0.05 | 21.50 | 737.76 |

*Table 5*. SAE standard J1349 standard ambient test conditions

| SAE Standard Ambient Test Conditions | | | | |
|---|---|---|---|---|
| **Water Vapor Pressure** | **Temperature** | | **Dry Air Pressure** | |
| | **Standard** | **Test Range Limit** | **Standard** | **Test Range Limit** |
| inHg | °F | °F | inHg | inHg |
| 0.30 | 77.00 | 59 - 95 | 29.23 | 26.6 - 31.0 |
| mmHg | °C | °C | mmHg | mmHg |
| 7.50 | 25.00 | 15 - 35 | 742.50 | 675.1 - 787.6 |

## 3.3 Operating and Boundary Condition Results

A number of engine subsystems were monitored throughout the experiments to ensure adequate engine operation, prevent catastrophic failures, and gather quantitative data to assist in the interpretation of results.

### 3.3.1 Engine Operating Conditions

Cooling System

It was observed during early testing that variations in engine temperature resulted in engine in brake power, torque, and cooling load. To verify that the designed engine heat exchanger was working properly, the radiator inlet and outlet temperatures were recorded for each test. The engine temperature set point (measured at the heat exchanger inlet, engine side) was set to a temperature of 165 °F (74 °C). As shown in Figure 33, trends in coolant temperature, measured at the radiator inlet, remained consistent throughout the experiments. An exception is observed at 30% throttle, between 5,000 and 5,500 RPM. These data points were determined to be outliers, potentially caused by an error in the temperature control unit.

The minimum recorded temperature was 158 °F (70 °C) at 4,000 RPM and 100% throttle. The maximum recorded temperature was 168 °F (75.5 °C) at 30% throttle and 8,500 RPM. Average temperatures and corresponding uncertainties are summarized in Table 6. Results indicate that the water-to-water heat exchanges enabled average temperature control to within $\pm$2.6 °F of the user-specified value of 165 °F (74 °C).

Figure 33 B shows that the radiator outlet temperature remained consistently below the radiator inlet temperature. This is expected, since the function of the radiator is to cool the flowing coolant. It is also observed that at higher engine speeds (7,000-9,500 RPM) the higher throttle openings (i.e. higher engine power output) led to lower radiator outlet temperatures. For example, at 9,500 RPM and 30% throttle, the radiator exit temperature is 161.9 °F (72.2 °C), while at 100 and 80 percent throttles, the radiator outlet temperature decreased to 159.2 °F (70.7 °C) and 158.3 °F (70.2 °C) respectively. This is expected as with a constant inlet temperature and mass flow rate, a lower outlet temperature is required to dissipate the higher coolant load at increased loads.

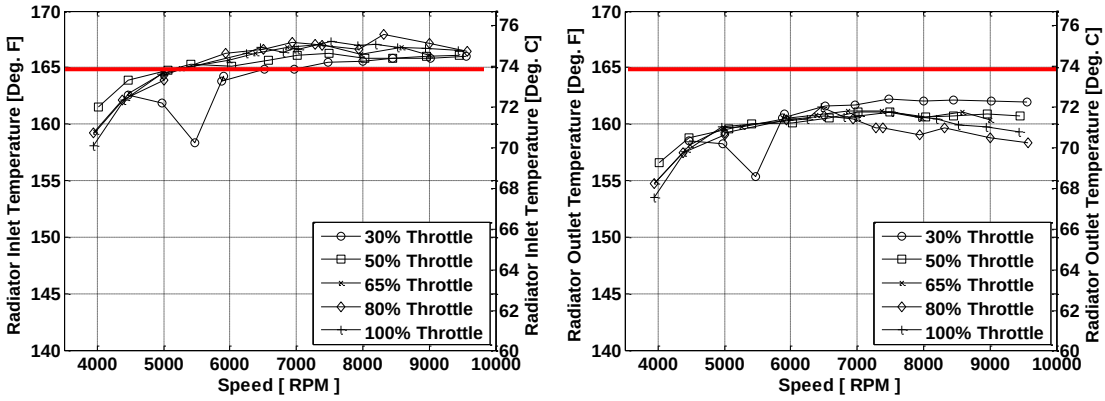


(A) (B)

*Figure 33.* Temperatures measured at the radiator inlet (A) and outlet (B). The set point value is specified by the red line.

*Table 6.* Average values of radiator inlet temperature at each throttle position

| Average Radiator Inlet Temp | | |
|---|---|---|
| **Throttle Position** | **Radiator Inlet Temp** | |
| | °F | °C |
| 30 | 164.1 ± 2.2 | 73.4 |
| 50 | 165.2 ± 1.3 | 74.0 |
| 65 | 165.2 ± 2.3 | 74.0 |
| 80 | 165.5 ± 2.5 | 74.2 |
| 100 | 165.6 ± 2.6 | 74.2 |

Oil pressure and temperature

While engine coolant temperature was held relatively constant thought each test, the engine oil temperature increased significantly. Figure 34 (A) shows that engine oil temperature remained between 139.6 °F (59.8 °C) and 158.1 °F (70.1 °C) at lower engine speeds and steadily increased with engine speed and throttle position to values ranging from 226.5 °F (108.1 °C) to 304.1 °F (151.2 °C). While the engine is equipped with an integrated, oil-to-water heat exchanger located next to the water pump (Figure 35), these results suggest that the current system may not be enough to adequately regulate engine oil temperature.

It was also important to ensure that the oil pressure remained above 7.1 psi (49 kPa) at 4,000 RPM and 120 °F (48.9 °C) oil temperature to ensure good engine health. As the engine oil system uses mechanically driven oil pumps, it was expected that engine oil pressure would increase as a function of increasing engine speed. As shown in Figure 34 (B), this trend in oil pressure was not observed for most throttle positions, as oil pressure remained relatively constant (between 14 and 16 psi) through the tested range of engine speeds and throttle positions. This could potentially be attributed to poor control of engine oil temperature, as the oil pressure is directly affected by the (temperature-dependent) viscosity of the fluid. That is, as the oil temperature increases, its viscosity decreases, decreasing oil pressure.

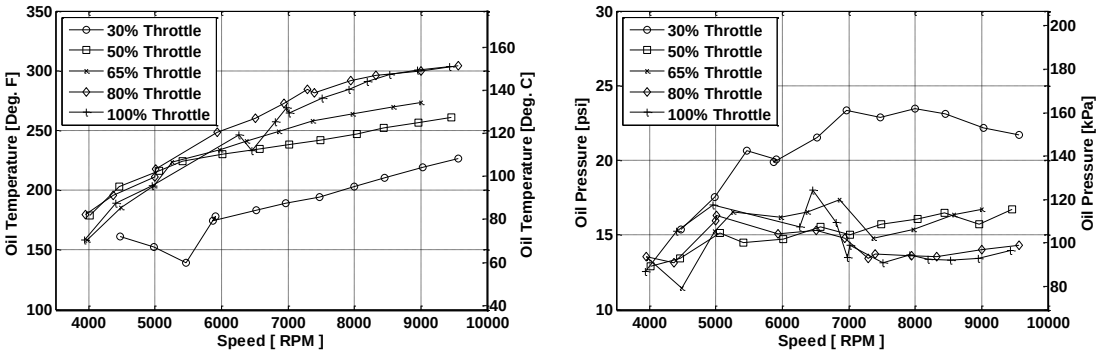


(A) (B)

*Figure 34.* Engine oil temperature (A) and pressure (B)

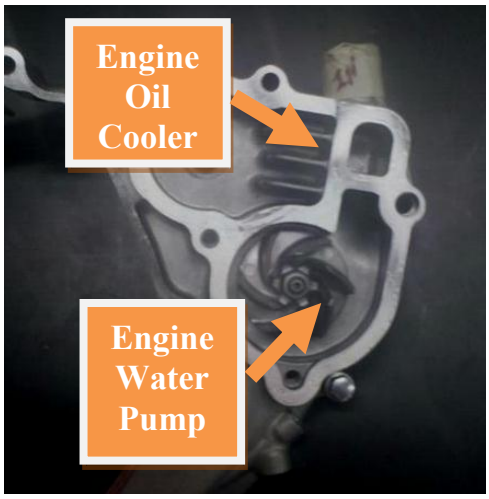


*Figure 35.* Integrated engine oil cooler

Fuel Pressure and Temperature

The engine ECM does not compensate fuel delivery for (fuel) pressure and temperature. . Because of this, it was important to ensure that these variables did not vary greatly throughout testing. Figure 36 (A) shows fuel pressure as a function of engine speed for the range of throttle positions tested. Summarized in Table 7, fuel pressure remained at an average value of 40.4 psi (278.3 kPa) with a maximum variance of ±0.3 psi (2.4 kPa)

at 80% throttle. It is important to note that, as with the stock setup, fuel pressure was held constant as a function of intake manifold pressure. Variations in fuel flow rate due to changing differential pressure across the fuel injector were compensated by the stock ECM as originally intended by the manufacturer. This is described in section 2.3

Fuel temperature (Figure 36B) ranged from 73.6 °F (23.1 °C) to 80.7 °F (27.1 °C). The maximum average fuel temperature recorded was 78.1°F (25.6 °C) ± 2.2°F. This temperature variation causes negligible variation in fuel density and therefore, in the mass of fuel injected.

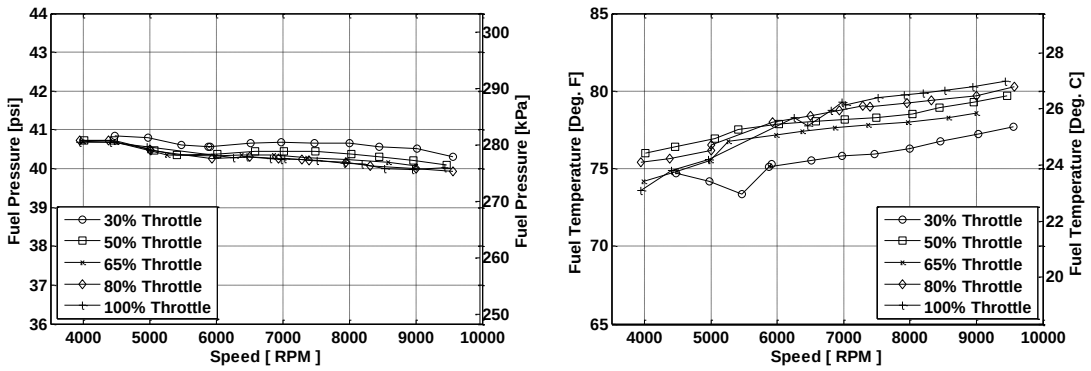


(A) (B)

*Figure 36*. Fuel pressure (A) and temperature (B)

*Table 7.* Average fuel pressure and temperature at each throttle position

| Average Fuel Pressure | | | Average Fuel Temperature | | |
|---|---|---|---|---|---|
| **Throttle Position** | **psi** | **kPa** | **Throttle Position** | **°F** | **°C** |
| 30 | 40.6 ± 0.2 | 279.9 | 30 | 75.7 ± 1.3 | 24.3 |
| 50 | 40.4 ± 0.2 | 278.4 | 50 | 78.0 ± 1.2 | 25.6 |
| 65 | 40.4 ± 0.2 | 278.4 | 65 | 77.1 ± 1.5 | 25.0 |
| 80 | 40.3 ± 0.3 | 277.7 | 80 | 78.1 ± 1.6 | 25.6 |
| 100 | 40.3 ± 0.2 | 277.5 | 100 | 78.4 ± 2.2 | 25.8 |

Fuel Mass Flow Rate and Mass Per Cycle

The mass flow rate of fuel (A) and mass of fuel injected per cycle (B) as a function of engine speed and throttle position are shown in Figure 37. As expected, the fuel mass flow rate increases as a function of engine speed. At lower engine speeds (4,000 to 5,000 RPM) and above 50% throttle, there was weak dependence of fuel flow rate on throttle position. This weak dependence on throttle position is also observed for the intake air flow, as will be shown by volumetric efficiency trends in a later section. For engine speeds greater than 5,000 RPM, the fuel flow rate increases with throttle opening. The mass of fuel injected per cycle, shown in Figure 43 (B) was also calculated as it provides a more convenient input for fuel injection modeling.

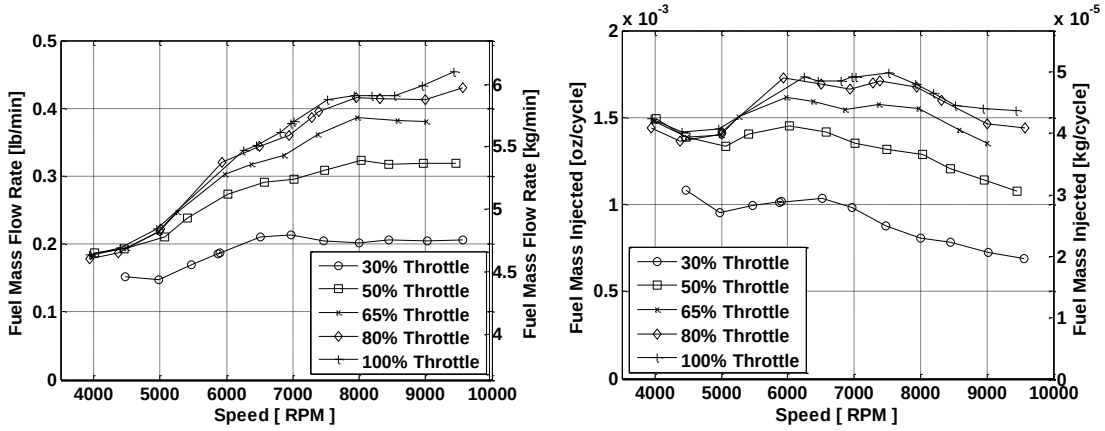


(A) (B)

*Figure 37*. Fuel mass flow rate (A), Fuel mass injected per cycle (B)

Fuel-to-Air Equivalence Ratio φ

The fuel-to-air ratio is the mass ratio of fuel to air. The equivalence ratio (φ), mathematically defined by equation 16, is the fuel-to-air ratio measured during actual operating conditions, normalized by the stoichiometric fuel to air ratio. Values greater than one indicate a fuel-rich mixture, with more fuel available that it is theoretically

required by the stoichiometric reaction.

The equivalence ratio[2] is shown in Figure 38. All equivalence ratio values were considerably higher than one, indicating that this engine is operated richer than expected at all conditions tested. Between 5,000 and 6,000 RPM the fuel-air mixture becomes richer as engine speed increases, with weak dependence on throttle position. Between 6,000 and 9,500 RPM, a relatively constant equivalence ratio of 1.45 $\pm$ 0.05 was observed. An exception is noted at 30% throttle. A potential cause for the observed deviation at this throttle position is an error in the fuel map of the Suzuki ECM.

$$\phi = \frac{(F/A)_{actual}}{(F/A)_{Stoich}} \qquad [16]$$

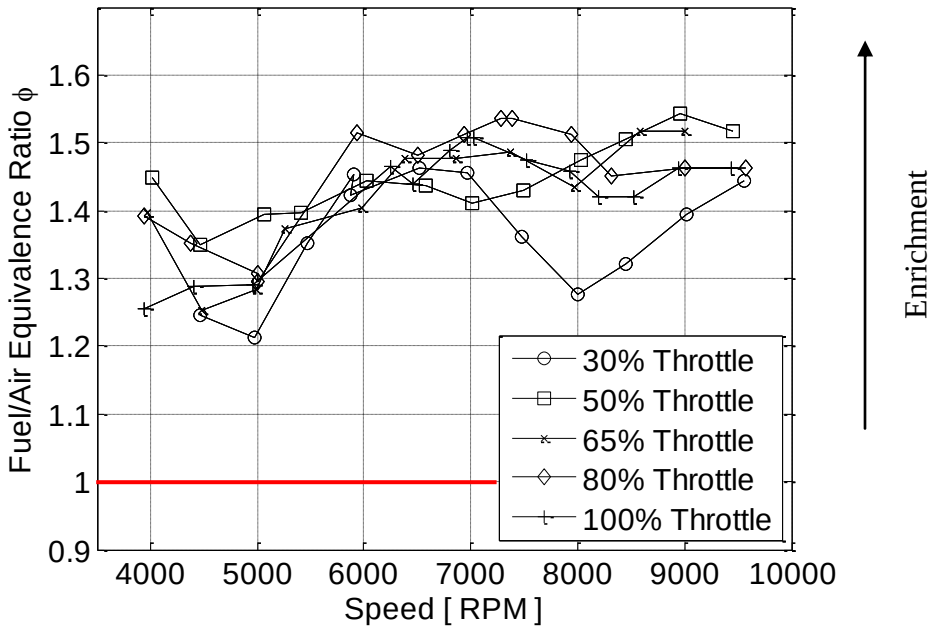


*Figure 38*. Fuel air equivalence ratio as a function of speed and throttle position for the Suzuki RM-Z450 engine. The stoichiometric value is shown the red line.

[2] The equivalence ratio was calculated assuming a 14.7:1 air-to-fuel ratio.

Intake Air Temperature and Manifold Pressure

Intake-air temperature, measured at the entrance of the engine air-box, is shown in Figure 39 (A) as a function of engine speed and throttle position. It was important for the intake-air temperature to remain relatively constant to minimize its influence on volumetric efficiency and consequently on engine performance. The minimum value observed was 76.1 °F (24.5 °C) at 30% throttle and 5,500 RPM, whereas the maximum value was 82.3 °F (27.9 °C) at 80% throttle and 9,500 RPM. The average intake air temperature at each throttle position is shown in Table 8. The maximum variation in temperature of 1.6 °F for the 100 and 80 percent throttle tests. This variation was considered acceptable and consistent with the overall increase in engine boundary temperatures discussed in section 3.3.2.

Intake manifold pressure, measured at the stock location, directly behind the throttle plate, is shown in Figure 39 (B) as a function of engine speed and throttle opening. As expected, the manifold pressure is inversely proportional to throttle opening. The highest and lowest manifold vacuums occurred at 30% and 100% throttle positions, respectively. The absolute manifold pressure decreases with engine speed as expected. The values of manifold vacuum are important as they provide a critical boundary condition input for computer simulations.

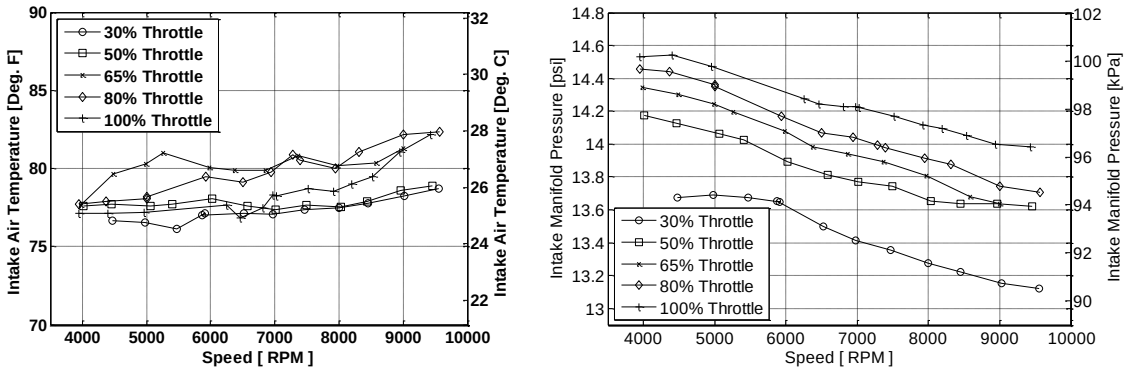


(A) (B)

*Figure 39.* Engine intake air temperature (A) and manifold absolute pressure (B)

*Table 8.* Average inlet air temperature during each throttle position test

| Average Inlet Air Temp | | |
|---|---|---|
| **Throttle Position** | **°F** | **°C** |
| 30 | 77.3 ± 0.7 | 25.2 |
| 50 | 77.8 ± 0.5 | 25.4 |
| 65 | 80.2 ± 1.0 | 26.8 |
| 80 | 79.8 ± 1.6 | 26.6 |
| 100 | 78.5 ± 1.6 | 25.8 |

Exhaust Gas Temperature and Pressure

Exhaust gas temperature and pressure are shown in Figure 40. With the exception of 30% throttle, the exhaust gas temperature increased steadily for all throttle positions, from 1,300 °F (704.4 °C) at 4,000 RPM to 1,500 °F (815.6 °C) at 9,500 RPM. Exhaust manifold pressure (Figure 40 B) increased both as a function of engine speed and throttle position, with a minimum value of 14.93 psi (101.59 kPa) at 30% throttle and 4,500 RPM and a maximum value of 15.98 psi (110.1 kPa) at 100% throttle and 9,500 RPM. These trends are dominated by the level of exhaust back pressure and provide useful boundary conditions for computer simulations.

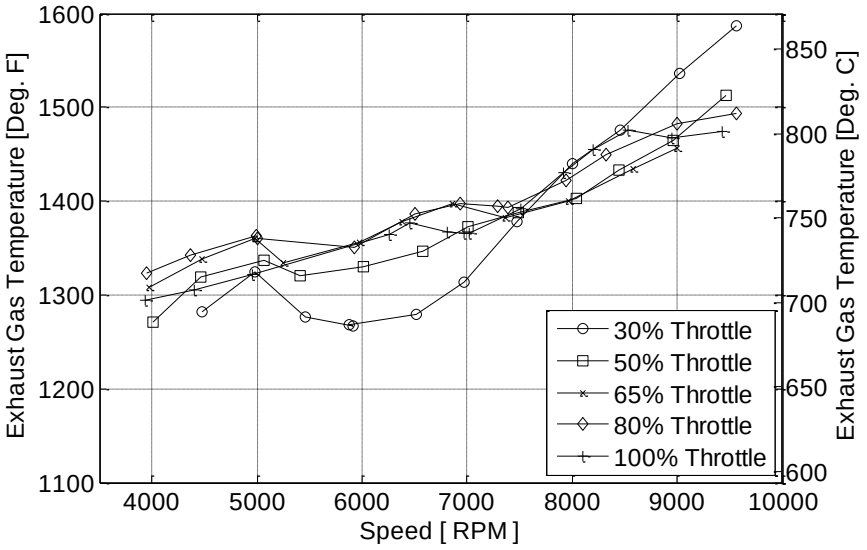


(A)

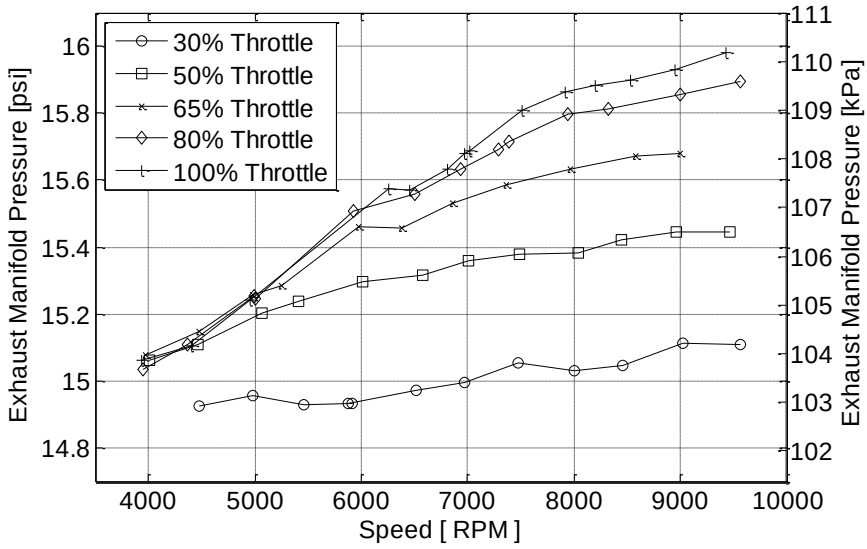


(B)

*Figure 40.* Exhaust gas temperature (A) and absolute manifold pressure (B)

### 3.3.2 Boundary Temperatures

Intake Port Temperature

Intake port surface temperatures as a function of engine speed and throttle position are shown in Figure 41 within quadrants specified in section 2.3. The temperature remains between 140 °F (60 °C) and 130 °F (54.4 °C) for the bottom left and right quadrants, respectively. The left quadrants exhibit higher temperatures relative to the right quadrants. Potential for the observed temperature differences include an imbalance in mass flow rates between the left and right runners, which could modify heat transfer from the port surface to the intake air stream and/or proximity of the left quadrant to a coolant passage, since the coolant temperature is higher than the port surface temperature. This information can be used to better define boundary conditions within CFD engine simulations.

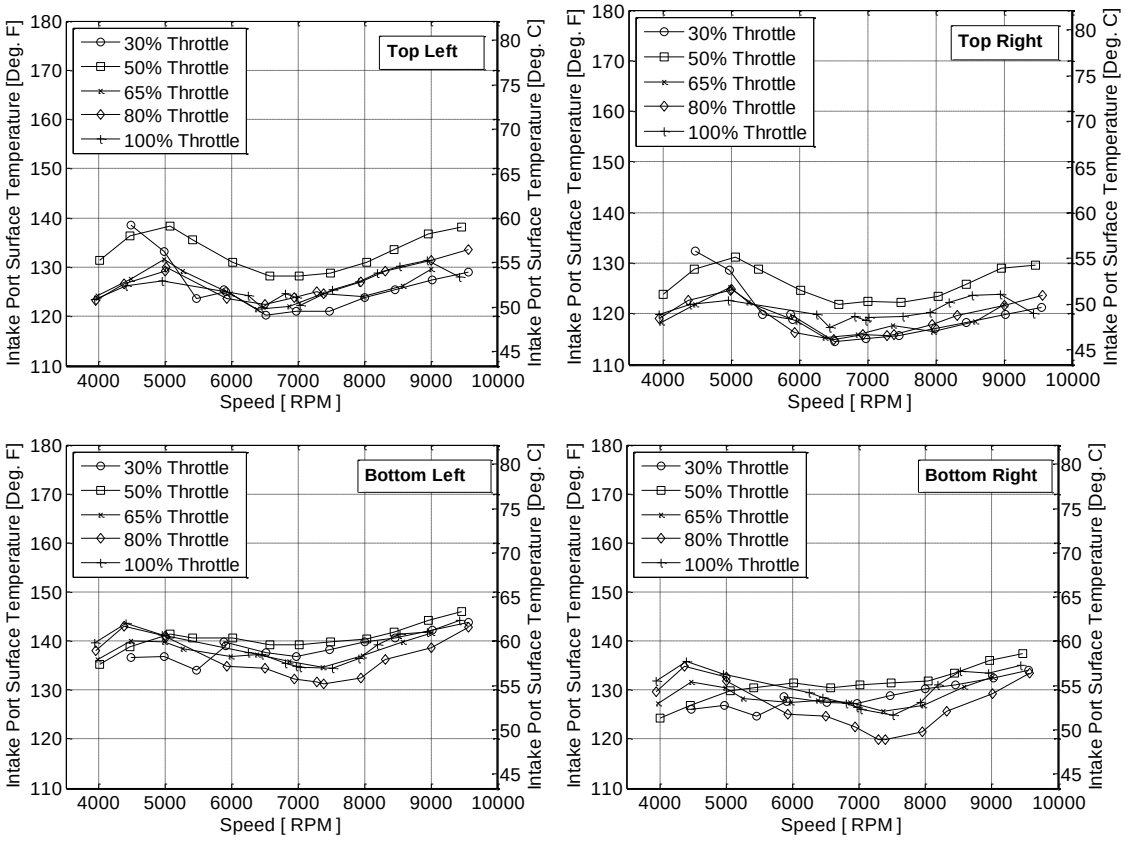


*Figure 41.* Intake port surface temperature at specified quadrants as a function of engine speed and throttle position

Exhaust Port Surface Temperature

Exhaust port surface temperature is shown in Figure 42. The temperature increased with increasing engine speed for all throttle openings. The exhaust port temperature also increased with increasing throttle openings up to 80% throttle. As with the intake port surface temperature, these readings provide boundary conditions useful for refining CFD engine simulations.

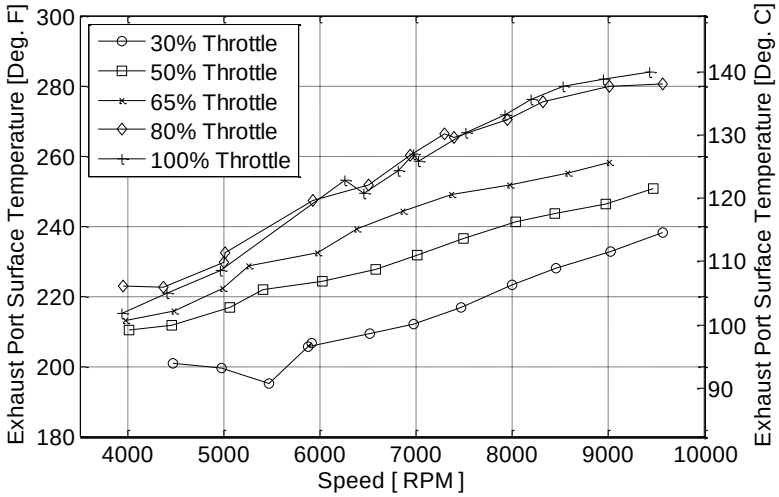


*Figure 42.* Exhaust port surface temperature as a function of engine speed and throttle position

Cylinder Wall Temperature

Figure 43 shows cylinder wall temperature as a function of engine speed and throttle position. These quantities were measured 1.5 inches from the top surface of the cylinder on the front, right and rear of the cylinder. The boundary temperature increases at all locations as a function of engine speed. Two exceptions are observed, one at 30% throttle and 5,500 RPM; the second at 80% throttle and 8,200 RPM. While no obvious reason was found to explain the latter, the former might be attributed to an error in the cooling

control (see section 3.3.1). A potential causes for the increase in cylinder wall temperature as a function of speed is the increase in friction as engine speed increases. It is also observed that cylinder wall temperature increases with increased throttle position. This increase might be explained by to the higher temperatures present at the gas/cylinder liner interface as both power and friction increase. Higher temperatures were recorded by the thermocouple located in the rear position (see section 2.4). This may be attributed to its proximity to the integrated transmission. The majority of the engine oil is stored in the transmission housing. The transmission housing temperature will depend heavily on engine oil temperature, which, as previously shown, varied significantly with engine speed and load.

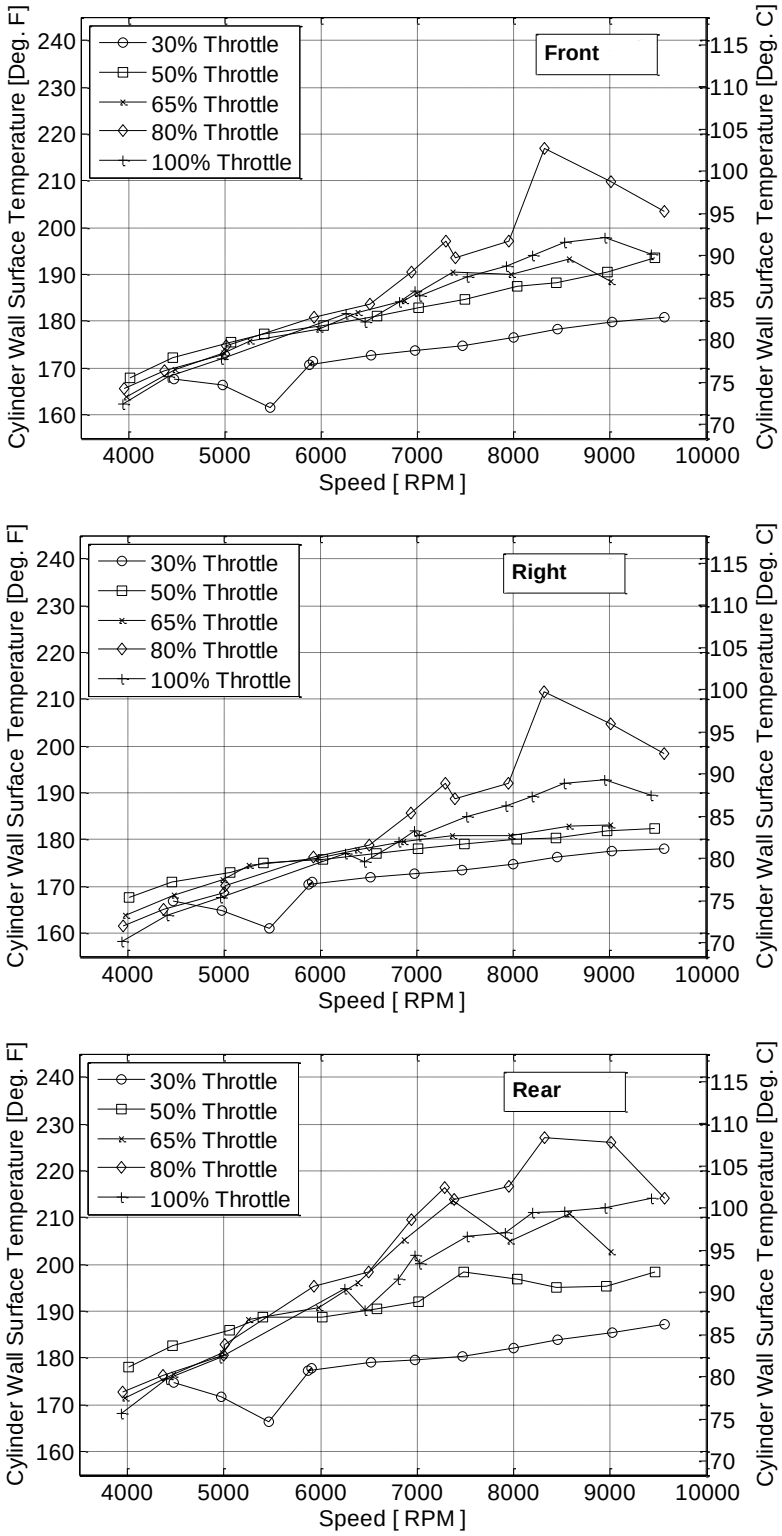


*Figure 43.* Cylinder wall temperatures as a function of engine speed and throttle position

## 3.4 Performance Results

### 3.4.1 Brake/Dynamometer Torque and Power

Brake torque and power as a function of engine speed are shown in Figure 44 A and B, respectively. As expected, brake power increases with engine speed in all cases. As summarized in Table 9, the maximum power is generally produced between 7,500 and 9,000 RPM. At lower throttle positions (30% to 50%) maximum power is produced at lower engine speeds when compared to higher throttle openings (80% and 100%). As highlighted in Table 9, peak torque occurs at 4,500 RPM for lower throttle positions (30% and 50%) and between 6,500 and 7,000 RPM for higher throttle openings. These trends might be explained by the observation that the speed at which intake air choking occurs increases as the throttle position is increased (i.e., as the throttle opens). Peak torque and power at wide-open-throttle are 62 Nm (46 lbf-ft) at 7,100 RPM and 50 kW (67 HP) at 8,600 RPM, respectively. Published values for a 2009 Suzuki RM-Z450 engine show peak torque and power of 45 Nm (33 lbf-ft) at 7,000 RPM and 36 kW (48 HP) at 9,000 RPM respectively [13]. These values are shown as reference only, since the test setup and operating conditions corresponding to the published values are unknown.

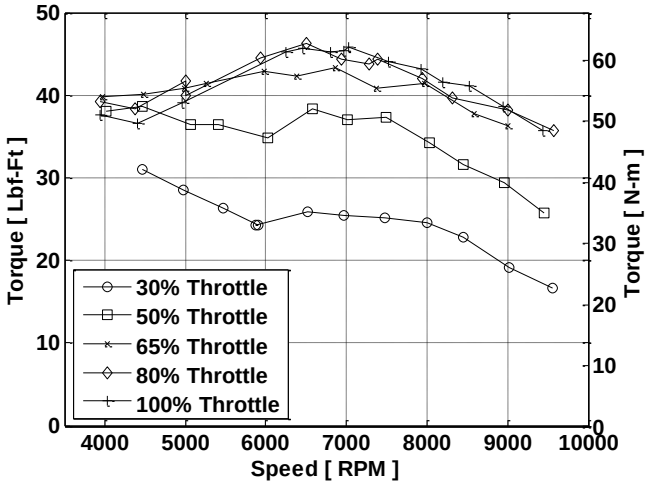


(A)

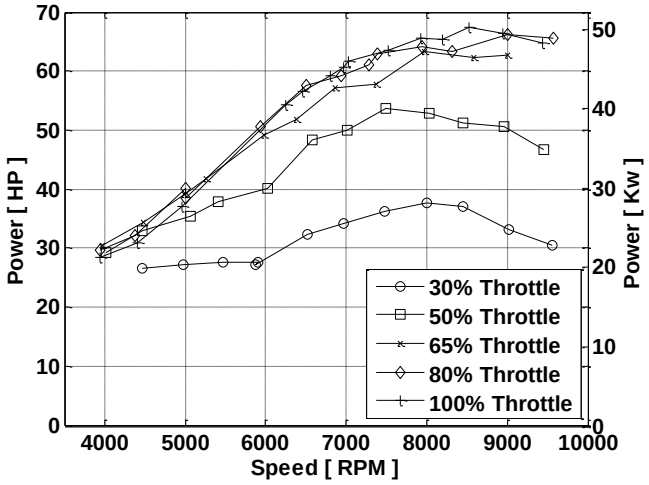


(B)

*Figure 44*. Brake torque (A) and brake power (B) as a function of engine speed

*Table 9.* Summary of maximum brake torque and power between 30% and 100% throttle

| Maximum Brake Performance Quantities | | | | | | |
|---|---|---|---|---|---|---|
| **Throttle Position** | **Maximum Torque** | | **Engine Speed** | **Maximum Power** | | **Engine Speed** |
| **[%]** | **[lbf-ft]** | **[N-m]** | **[RPM]** | **[HP]** | **[KW]** | **[RPM]** |
| 30 | 31.1 | 42.2 | 4500 | 37.6 | 28.0 | 8000 |
| 50 | 38.6 | 52.3 | 4400 | 53.7 | 40.0 | 7500 |
| 65 | 43.4 | 58.9 | 6900 | 63.3 | 47.2 | 8000 |
| 80 | 46.2 | 62.6 | 6500 | 66.1 | 49.3 | 9000 |
| 100 | 45.8 | 62.1 | 7000 | 67.4 | 50.3 | 8500 |

3.4.2 Net Indicated Power

The net indicated power, calculated using equation 5, is shown in Figure 33 for a range of speeds and throttle openings. Similar to the results of brake power, the net indicated power increased with increasing throttle opening. This is expected, as indicated quantities are a function of the in-cylinder pressure magnitude. As speed increases and throttling is reduced, more air and consequently fuel are brought into the cylinder. More energy is released during combustion, raising the in-cylinder pressure. . As summarized in

Table ***10***, the net indicated power reached a maximum at similar engine speeds for all throttle positions except 100%, for which it occurred 1,000 RPM later at 9,500 RPM. Net indicated power was not quantified for 80% throttle due to equipment malfunction during testing at that throttle position.

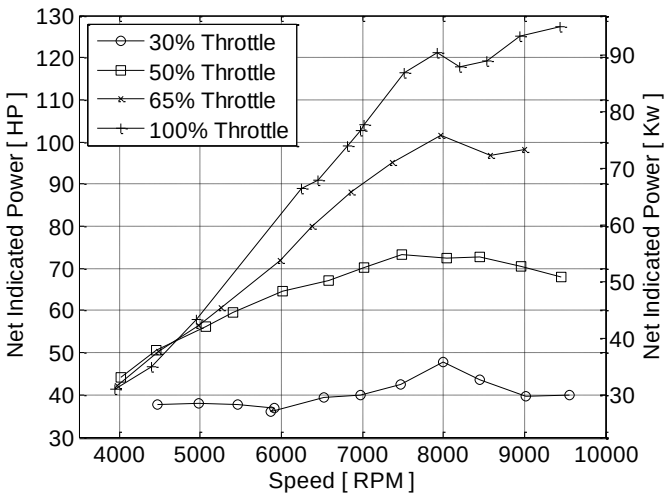


*Figure 45*. Net indicated power as a function of engine speed and throttle position

*Table 10.* Summary of maximum net indicated power between 30% and 100% throttle.

| Maximum Net Indicated Power | | | |
|---|---|---|---|
| **Throttle Position** | **Power** | | **Engine Speed** |
| **[%]** | **[HP]** | **[kW]** | **[RPM]** |
| 30 | 47.8 | 35.6 | 8000 |
| 50 | 73.4 | 54.7 | 7500 |
| 65 | 101.6 | 75.8 | 8000 |
| 100 | 127.3 | 94.9 | 9500 |

3.4.3 Mean Effective Pressure

Trends in mean effective pressure as a function of engine speed are shown in Figure 46 for 30%, 50%, 65% and 100% (wide-open) throttle. Regardless of throttle opening, pumping losses exhibit a modest increase with engine speed ranging from approximately 1.2 psi (8.3 kPa) to 16 psi (110 kPa). The trend in pumping mean effective pressure is more clearly illustrated in Figure 47. Pumping losses are comparable at 30% and 50% throttle. Pumping losses are also highest at these throttle openings, increasing significantly above 6,000 RPM with respect to 65% and wide-open throttle. The power lost to rubbing and accessory friction[3] is most significant at larger throttle openings. The maximum friction, 204 psi (1.4 MPa), was found at wide-open-throttle. This is a 38% increase from the maximum friction of 148 (1.0 MPa) at 65% throttle. The increase in rubbing friction with increasing throttle opening may be explained as follows: as load increases, more air (and proportionally fuel) is inducted into the combustion chamber. More energy is released, which causes a rise in the in-cylinder pressure. The load exerted

[3] Rubbing and accessory friction are not decoupled in this work

by the working fluid on chamber and piston surfaces increases, which leads to an increase in friction forces. An increase in accessory friction (specifically in friction within the integrated transmission) might also help explain the observed trend. As the load in the transmission increases with increased torque output, the friction of the gear train and bearings is also expected to increase. As speed increases, the effects of hydrodynamic drag as the transmission components rotate within the oil sump become more significant, increasing friction

Based on the magnitude of pumping versus rubbing/accessory friction, it can be concluded that rubbing and accessory friction losses are the dominant sources of mechanical efficiency losses for the 2008 Suzuki RM-450Z engine, regardless of speed and load. It is emphasized again that, in this work, accessory friction includes contributions from the integrated transmission.

The present findings can be used for validating the model predictions of indicated work and power, and to supply these models with friction parameters which may be difficult to estimate accurately in the absence of physical data.

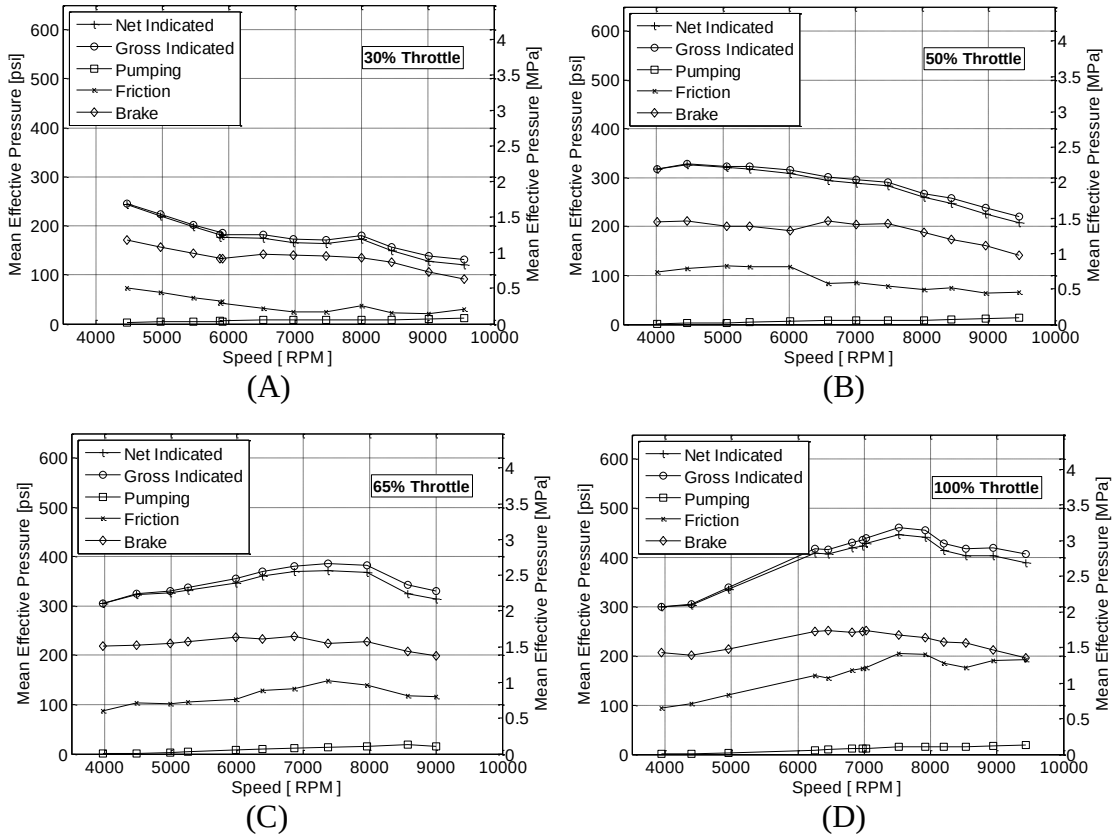


*Figure 46*. Mean effective pressure as a function of engine speed for 30% (A), 50% (B), 65% (C) and 100% (D) throttle

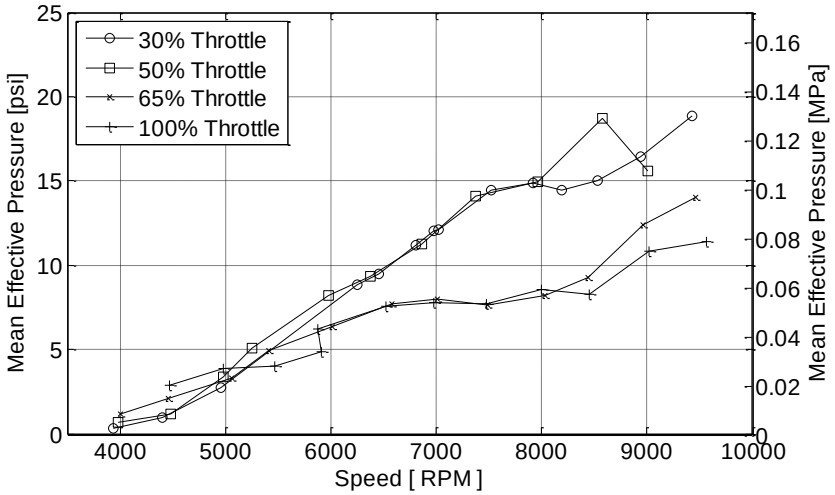


*Figure 47*. Pumping mean effective pressure

3.4.4 Coolant Load

Quantified using equation 11, the cooling load, as a function of engine speed and throttle position, is shown in Figure 48. Cooling load ranges from 5.1 HP (3.8 kW) at 30% throttle and 5,500 RPM to 19.7 HP (14.7 kW) at 80% throttle and 9,500 RPM. Cooling load increases as the throttle is opened with the exception of 30% throttle and 5,500 RPM. This error can potentially be caused by the uncertainty in engine temperature control noted in section 3.3.1. The observed increase is expected, as cooling load increases with engine power output, which exhibits a similar trend. Cooling load also increases as the throttle opens, with maximum values at 80% and 100% throttles twice that of the maximum value of 30% throttle at maximum engine speed.

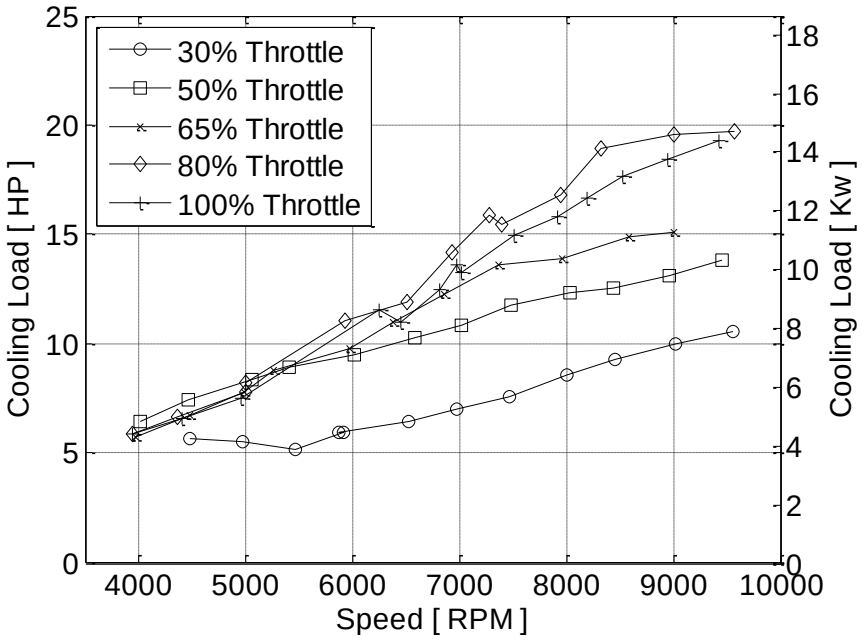

Figure 48. Cooling load as a function of engine speed and throttle position.

3.5 Efficiency Results

3.5.1 Fuel Conversion Efficiency

The fuel conversion efficiency (equation 15) as function of engine speed and throttle position is shown in Figure 49. Values ranged from 32% at wide open throttle and 9,500 RPM to 42% at 30% throttle and 8,000 RPM. A summary of the average fuel conversion efficiency for each throttle position and their standard deviation is shown in Table ***11***.

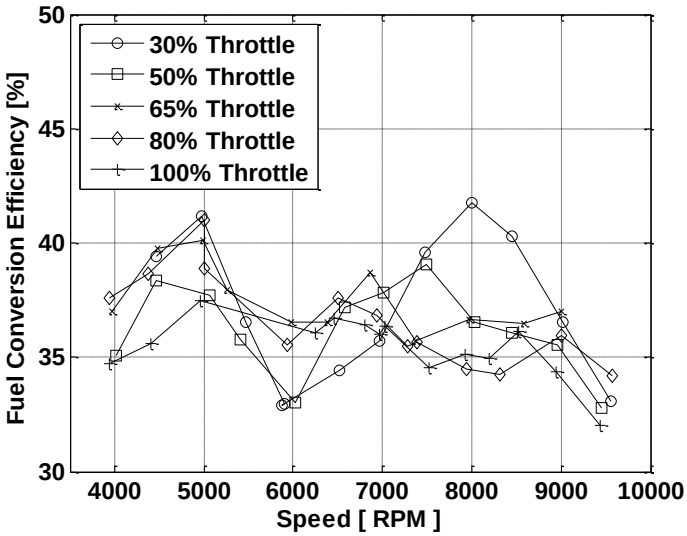


*Figure 49.* Fuel conversion efficiency as a function of engine speed and throttle position

*Table 11*. Average fuel conversion efficiency with standard deviation at each throttle position tested.

| **Average Fuel Conversion Efficiency** | |
|---|---|
| **Throttle Position [%]** | **Fuel Conversion Efficiency [%]** |
| 30 | 37 ± 3.3 |
| 50 | 36 ± 2.0 |
| 65 | 38 ± 1.4 |
| 80 | 37 ± 2.1 |

| | |
|---|---|
| 100 | $36 \pm 1.3$ |

3.5.2 Specific Fuel Consumption

Brake and net-indicated specific fuel consumption (equation 14) of the Suzuki RM-450Z engine are shown in Figure 50. These quantities are related to each other through the mechanical efficiency, according to equation 17.

$$bsfc = \frac{isfc_{net}}{\eta_m} \quad (17)$$

The net-indicated fuel consumption ($isfc_{net}$) ranges between 50 and 160 g/(kWh). It increases steadily for all loads between approximately 4,000 and 6,500 RPM, although this increase is more pronounced at 65% and 100% throttle. Overall, however, the net-indicated specific fuel consumption remains lower at these throttle positions. Above 6,500 RPM, the net-indicated fuel consumption remains fairly constant, between 100 and 140 g/(kWh) at 65% and 100% throttle, and at approximately 160 g/(kWh) at 30% and 50% throttle.

As expected, the brake specific fuel consumption remains consistently higher than net-indicated values, ranging between 200 and 255 g/(kWh), depending on speed and load. At 100% (wide-open) throttle, the trend is as expected: the fuel consumption is highest at lower speeds (i.e., below 5,000 RPM) and higher speeds (i.e., above 8,500 RPM). The reasons for the observed trend at 100% throttle are well documented in the technical literature (12). Heat losses and friction are the dominant mechanisms for reducing engine power output at low and high speeds, respectively, increasing the specific fuel

consumption (see equation 14). At 30% and 50% throttle, a depression in the brake specific fuel consumption curve is evident at around 8,000 RPM (red circle in figure 50). According to equation 17, the brake specific fuel consumption may be increased by decreasing the mechanical efficiency and/or increasing the net-indicated specific fuel consumption. As will be shown in figure 52, the mechanical efficiency decreases sharply at 8,000 RPM. A slight decrease in the net-indicated specific fuel consumption is also apparent, which correlates well with a decrease in the equivalence ratio (i.e., fuel-leaner mixture) at that operating point (see figure 38).

Both the fuel conversion efficiency (section 3.5.1) and specific fuel consumption are important baseline metrics for designing a gasoline direct-injection fuel system. These quantities provide a useful baseline for fuel economy, which is worth 10% of the total points in the FSAE endurance race (9). While the engine is generally operated at wide-open-throttle in these events, reducing fuel consumption is also important in portions of the course that demand part-throttle operation (e.g. during steady state cornering) to increase the overall fuel economy in FSAE dynamic events.

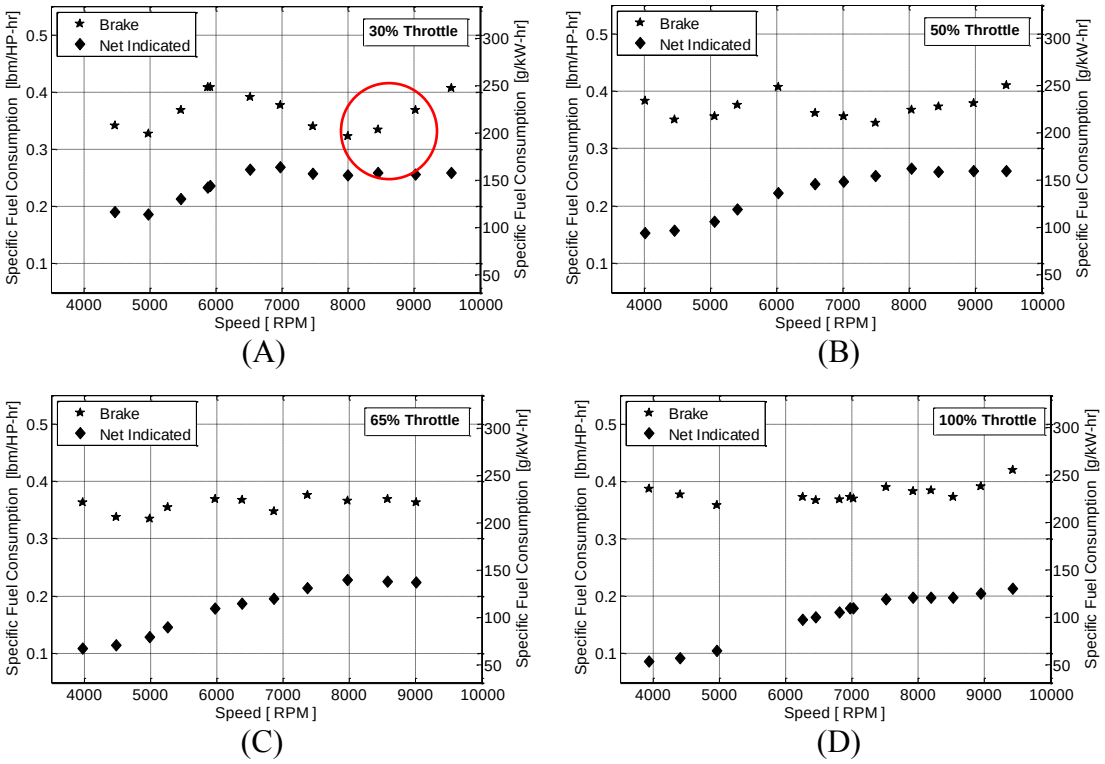


*Figure 50*. Brake and net indicated specific fuel consumption as a function of engine speed for 30% (A), 50% (B), 65% (C) and 100% (D) throttle

### 3.5.3 Volumetric Efficiency

Figure 51 shows volumetric efficiency as a function of engine speed and throttle position. As expected, volumetric efficiency increases with increased throttle position (i.e., smaller flow restriction). For throttle positions 30% and 50% the volumetric efficiency decreases with increasing engine speed, with maximum values occurring at the lowest engine speed of 4,000 RPM. At small throttle openings, the flow may become choked at comparatively lower engine speeds. At larger throttle openings, additional dynamic factors affect volumetric efficiency For example, at lower engine speeds and fixed valve timing, backflow from the exhaust manifold and increased time for charge heating reduce the intake flow. While these effects become less dominant as engine speed increases,

flow friction and choking effects begin to affect volumetric efficiency, potentially reducing air induction into the cylinder (12).

Table 12 presents the maximum volumetric efficiency and the speed at which it occurs for each throttle position. As discussed, from 30 to 50 percent throttle, this peak occurred at the lowest test speed of 4,000 RPM. Between 80 and 100 percent throttle, the volumetric efficiency reaches approximately 100% between 6,000 and 6,500 RPM. Trends in volumetric efficiency correlate well with trends in brake torque. These data can be useful for quantifying the effect of modifying the intake system (e.g. by incorporating a restrictor) on engine performance.

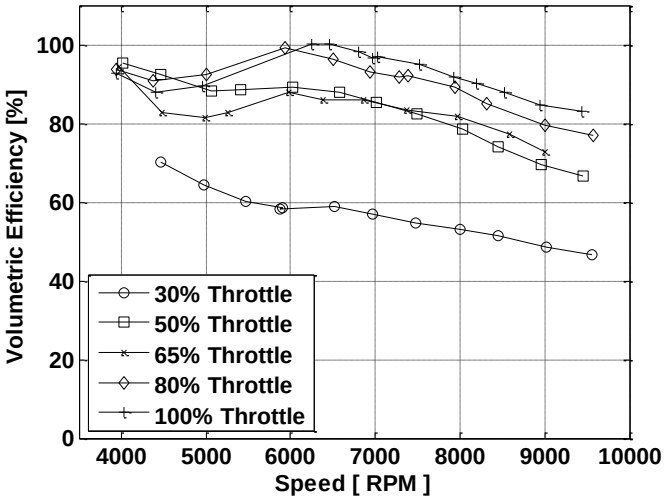


*Figure 51.* Volumetric efficiency as a function of engine speed corresponding for a 2008 Suzuki RM-450Z.

*Table 12.* Maximum volumetric efficiency for the RM-Z450 engine as a function of throttle position, showing magnitude and location within the speed range.

| Maximum Volumetric Efficiency | | |
|---|---|---|
| **Throttle Position [%]** | **Volumetric Efficiency [%]** | **Engine Speed [RPM]** |
| 30 | 70 | 4,000 |
| 50 | 95 | 4,000 |
| 65 | 94 | 4,000 |
| 80 | 99 | 6,000 |
| 100 | 100 | 6,500 |

3.5.4 Mechanical Efficiency

The mechanical efficiency as a function of throttle position and engine speed is shown in Figure 52. At speeds above 6,000 RPM, the mechanical efficiency decreases with increased throttle opening. This is consistent with the increase in total friction as the throttle opens (see section 3.3.3), which is dominated by an increase in rubbing and accessory friction.

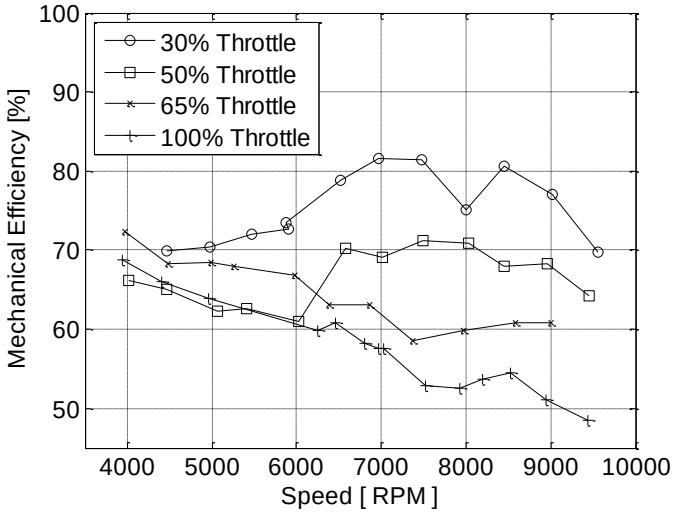


*Figure 52*. Mechanical efficiency as a function of engine speed and throttle position

3.6 Peak In-Cylinder Pressure and Location

The peak in-cylinder pressure as a function of engine speed and throttle position is shown in Figure 53 (A). As expected, the maximum pressure increases with throttle opening. It ranges from a minimum value of 315 psi (2.2 MPa) at 30% throttle and 9,500 RPM to a maximum of 1,263 psi (8.7 MPa) at 100% throttle at 7,500 RPM. At lower throttle positions (30 and 50%), peak cylinder pressure decreases from its maximum value, reached at 4,500 RPM, as engine speed increases. This behavior might be correlated to volumetric efficiency trends shown in section 3.5.3. At low throttle openings, the volumetric efficiency is lower, indicating that less air and subsequently fuel is inducted into the system. Consequently, the energy released during combustion and hence, the peak pressure will decrease. At higher throttle openings, (65 and 100%) the peak pressure increases in correspondence with volumetric efficiency. Overall, trends in brake torque (section 3.4.1) correlate with those of peak pressure. Maximum pressure and brake torque are found at similar engine speeds for each throttle position.

The magnitude of peak pressure reveals why direct-injection systems require higher fuel injection pressures compared to PFI systems. The flow rate of fuel delivered by the injector is proportional to the pressure differential across the injector. In direct-injection engines, this difference depends on the in-cylinder pressure at the time of injection. If late injection (i.e., during the compression stroke) is desired, the fuel pressure must be higher than that of in-cylinder pressure to ensure adequate spray penetration.

The location of peak pressure relative to top-dead-center compression is shown in Figure 53 (B). Peak pressure location retards (i.e., later in the cycle) slightly between 4,000 to 5,000 RPM for most throttle positions. At 100% throttle, the location of peak pressure remains fairly constant (45 ATDC) between 5,000 to 8,000 RPM. This is expected, as it is common practice to advance (i.e., earlier in the cycle) the spark timing, of an engine to maintain combustion phasing approximately constant as engine speed increases. Similar trends are found at 65% throttle between 4,000 to 7,500 RPM. At this point, the location of peak pressure is retarded by approximately five CAD. This spike may be attributed to the engine operating with a leaner fuel-air mixture at the same throttle and speed location, which would slow down the burn rate and retard combustion phasing. The trend at fifty percent throttle is similar to that found at higher throttle positions between 4,000 and 6,000 RPM. Above 6,000 RPM, the in-cylinder pressure peaks earlier in the expansion stroke. Although this behavior could be explained by the overall reduction in the fuel-air mass trapped in the cylinder at these conditions (see volumetric efficiency curve), a definitive conclusion is not possible without spark timing data. The same observation

applies to the relatively advanced values observed at 30% throttle. As for the 65% throttle, the sudden retardation in the location of peak pressure may also correlated to decrease in the equivalence ratio.

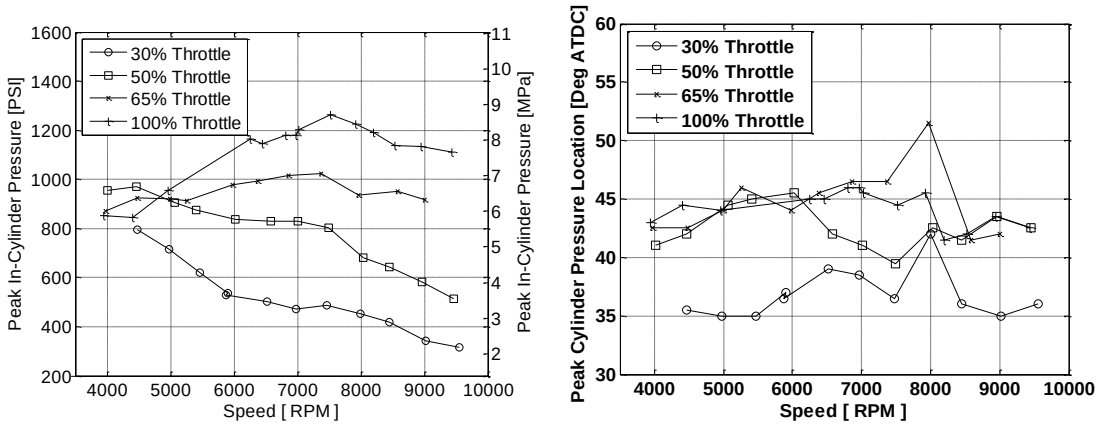


(A) (B)

Figure 53. Peak in-cylinder pressure (A) and peak cylinder pressure location relative to top- dead-center compression (B)

# CHAPTER 4

## REFINEMENT OF CFD MODEL FOR THE DIRECT FUEL-INJECTED ENGINE

As mentioned in Chapter 1, benchmarking of the single-cylinder RM-Z450 engine was pursued for two main reasons: first, to identify areas where modifications of the engine in its port-fuel-injected configuration can be made to increase performance and efficiency; and second, to advance efforts toward converting the RM-Z450 to a direct-fuel-injected engine. The second objective requires the development of a CFD engine model, as it would be impractical to evaluate the effect of design changes solely through physical testing. CFD models of internal combustion engines require accurate boundary and initial conditions to successfully reproduce engine performance. In the past, these values have been mostly estimated due to lack of experimental data. The experimental data gathered as part of this work opens new possibilities for developing an accurate engine model.

In this chapter, past modeling efforts of the single-cylinder engine are first described. Semi-quantitative results in the areas of injector packaging, piston head design, and compression ratio are reviewed to illustrate the potential benefits of direct-injection specific to the RM-Z450 engine. Sources of uncertainty in the original model due to lack of experimental data are described, emphasizing how the data acquired in the present work might be used for model refinement. The revised simulation, incorporating physically-tested boundary conditions, as well as mesh size and cross linking refinements, is described in section 4.5. Finally, results from the preliminary and new simulations are compared to the section 4.6.

## 4.1 Review of Previous Design

### 4.1.1 - Injector Packaging

In a previous feasibility study, the author considered the feasibility of packaging the injector in a RM-Z450 engine (11). The three main constraints for selecting injector location were temperature effects, ease of implementation, and allowable injection angle based on surrounding geometry. The final configuration for a new, direct-injection engine design incorporated Bosch's B5602_2 injector (Figure 54). The injector has a length-to-diameter ratio of 1.67 and delivers 17.5 $cm^3/s$ of fuel at 10 MPa injection pressure. These specifications were adequate to deliver the proper amount of fuel and overcome the effects of the compression inside the cylinder.

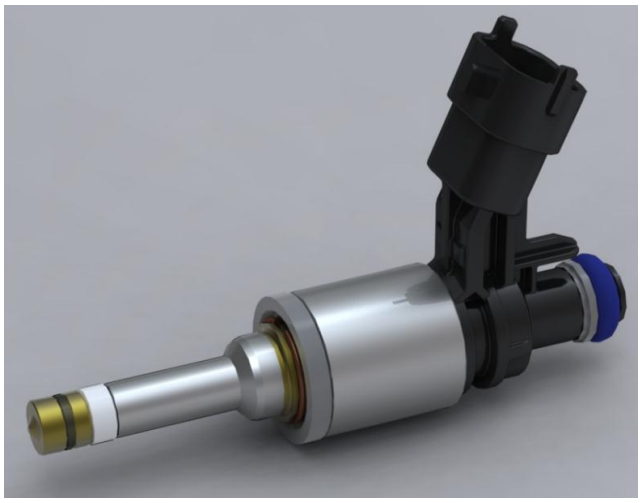

*Figure 54*. Rendering of BOSCH B5602_2 injector

This injector was designed to deliver fuel at 30 degrees from the centerline of the injector in any direction. This attribute made the B5602_2 ideal for this application, since the physical packaging constraints of the head limit the injector location, and thus the angles at which the fuel can be injected. Since the injector could not be placed on the exhaust side of the engine head, only two mounting positions were available to ensure fuel delivery at the proper angle. The first option was mounting the injector between the intake ports of the head, angled 41 to 63 degrees from the horizontal axis (Figure 55A). This modification would require re-designing the intake ports to allow sufficient space for the injector to rest, while positioning the injector head close enough to the edge of the chamber. The second possible placement was parallel to and underneath the intake runner (Figure 55A). This required no modification of the ports and only minimal addition of material for mounting the injector in the cylinder head. The engine geometry, however, limited the range of injection from 35 to 47 degrees from the horizontal. The possible injector placements are shown in Figure 55; the first image shows the semi-vertical and parallel-to-intake locations, whereas and the following demonstrates the feasible injection angles (as shown by the spray cone relative to the piston at bottom dead center).

After considering both possible injector locations and manufacturing requirements of each design, it was concluded that the semi-vertical set-up would require a brand new cast of the redesigned head to accommodate the change in port design. Since this was a major modification to the original system, the second design, requiring packaging the injector underneath and parallel to the intake runner, was chosen. Since this configuration allowed for a range of injection angles between 35 and 47 degrees, the angles of 35, 40 and 45 degrees from the horizontal axis were analyzed using the computational fluid

dynamics software Ricardo VECTIS to qualitatively assess the effect of injection angle on fuel-air mixing and boundary wetting. Results are presented in section 4.3. It should be emphasized, however, that to adequately select the final injector placement and injection angle, the CFD model needs to reliably predict fuel-air mixing throughout the intake and compression strokes. It should also capture the general features of the combustion process. Not enough physical data were available at the time of this preliminary assessment to ensure model accuracy. Therefore, only a qualitative comparison will be made in section 4.3.

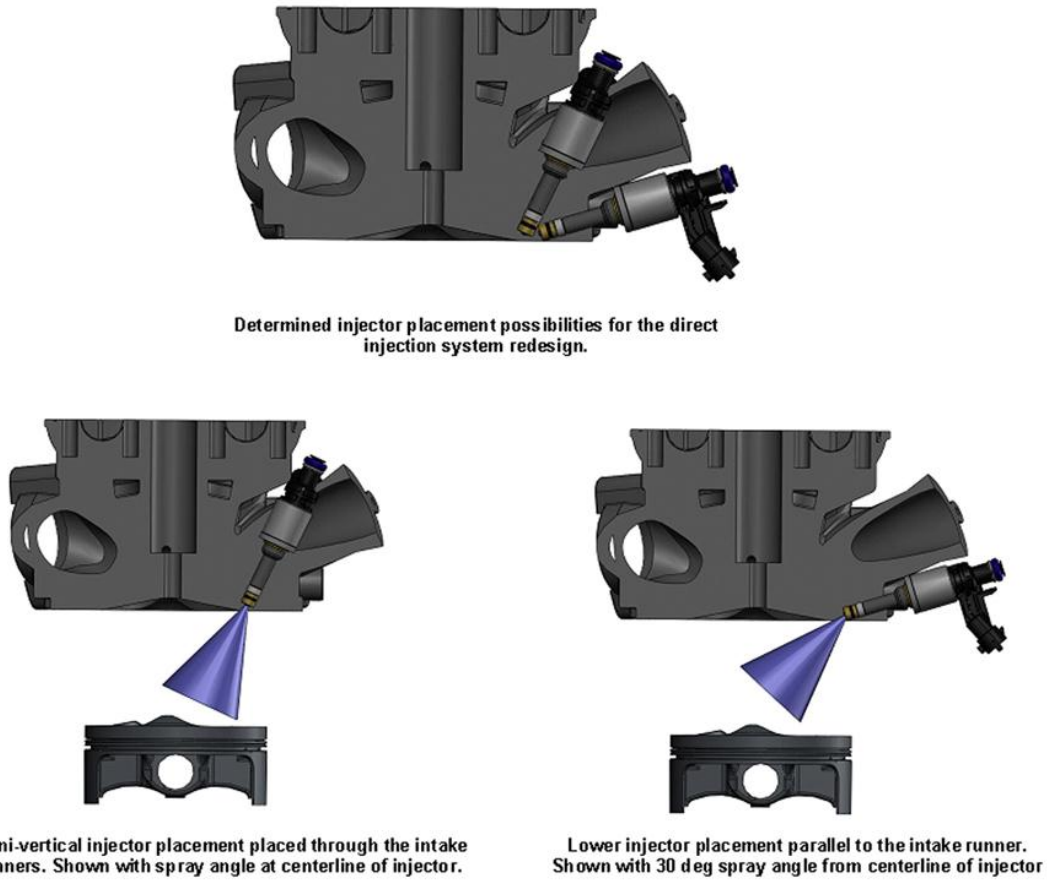


*Figure 55*. Comparison of possible injector placement within the stock Suzuki RM-450Z cylinder head

### 4.1.2 Piston Head Design

After preliminary considerations of injector packaging, piston design was considered. Since mixture preparation times are generally shorter for direct-injection engines than for port-fuel-injected designs, exploring alternative piston designs was in order. The goals were to increase the engine compression ratio (to increase the engine thermal efficiency, and output power); and to enhance fuel-air mixing within the cylinder. Based on reviews of the technical literature, three piston designs were considered. The first design consists of a flat top piston, similar to the stock RM-Z450 piston, but modified to reduce the clearance height. The second and third designs incorporated a shallow bowl (rim diameter of 80mm and a depth of 3mm), and a deep bowl, (rim diameter of 60mm and a depth of 6mm). These designs are shown in Figure 56 and Figure 57.

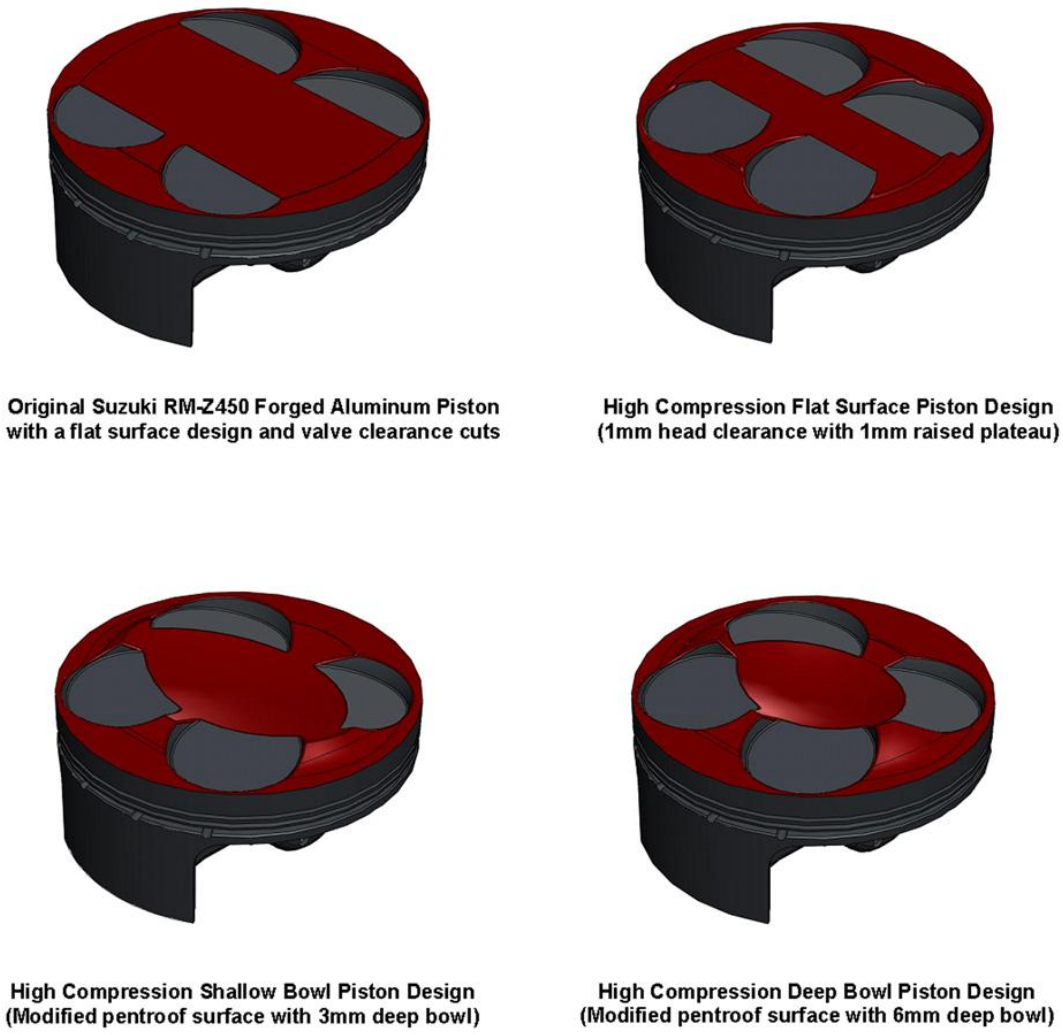


*Figure 56.* Comparison of piston designs - isometric view


*Figure 57.* Comparison of piston designs - side view cutaway

These bowl designs were used to enable the fuel injected on the intake side to more easily reach the opposite side of the cylinder. The idea is that during the compression stroke, the injected fuel would move along the surface of the piston bowl to the opposite side of the piston, working with the tumble flow within the cylinder to generate a homogeneous mixture quicker than the flat top piston. Due to the large cylindrical sections removed from each piston design (which ensured valve clearance when the cylinder was at TDC) increasing the compression ratio would require the addition of material on the piston surface. The contours of the piston surface directly match the cylinder head contour at top-dead-center, increasing the overall clearance height by 1mm at the rim and 1.5mm near the valves. The bowls and cylindrical sections for the valves were then removed from this surface, generating the largest compression ratio possible. To analyze the effects of each piston on the motion and mixing of the fuel within the chamber, they were imported into Ricardo VECTIS for computational fluid dynamics simulation. The results of this are discussed in section 4.3.

### 4.1.3 Compression Ratio

It is desirable to increase the compression ratio of an engine to increase its thermal efficiency and capitalize on fuel economy benefits. Two main design parameters were considered when selecting the compression ratio: the geometric constraints of the piston-cylinder head clearance and the onset of knock. Due to piston to valve and cylinder head clearance limitations, the maximum compression ratio was geometrically limited to 14.1:1, an additional 1.9:1 from the original stock piston.

When increasing the engine compression ratio, the onset of knock is a critical concern that should be investigated. Two solution methods were evaluated to estimate the knock-limited compression ratio. The first of these was a MathCAD model incorporating thermodynamic principles (e.g., evaporative cooling of the liquid jet), which revealed a maximum compression ratio of 14.8:1. The second method consisted of using Ricardo Wave, a one-dimensional simulation code, to evaluate knock intensity as a function of compression ratio. With this method, knock intensity was monitored as the compression ratio varied between 12.2:1 and 16.0:1, in increments of 0.1. As expected, knock intensity increased with increasing compression ratio. The maximum allowable compression was found to be 15.5:1. Based on geometric and knock-limit constraints, the final compression ratio was conservatively chosen to be 14.0:1.

## 4.2 Previous CFD Simulation Work

Results from the preliminary assessment described in section 4.1 established a design envelope for further evaluation. Yet, to investigate the effect of direct injection on the performance of the single-cylinder engine, the effect of injection angle and piston geometry on fuel-air mixing needed to be assessed. The most effective approach was to develop a computational fluid dynamics model of the engine cycle that would facilitate conducting parametric studies. This section describes the use of three-dimensional fluid dynamics software to develop a model for the single-cylinder engine, as well as efforts to improve the model using the experimental benchmark data and results from current simulations.

### 4.2.1 Software Overview and Simulation Strategy

Ricardo VECTIS is a three-dimensional computational fluid dynamics software (CFD) specifically designed flow simulations in automotive applications, ranging from under-hood cooling to in-cylinder flow. The software is divided into three main sections: Phase 1, Phase 5, and Phase 6. In Phase 1, geometry models are imported, boundaries defined, and meshes prepared. The geometries are then meshed and exported to a data file. Input conditions are entered in Phase 5. These include number of iterations, boundary conditions and initial conditions. Also within Phase 5, sub-models such as fuel spray and combustion can be configured. The solver is then activated from this phase, and the case study simulated. Once the simulation is complete, a post file is written, and this post file can be viewed in Phase 6. Two-dimensional plots such as velocity profiles and scalar plots can be created in this phase, as well as two-dimensional and three-dimensional

animations of transient solutions. To visualize graphical results such as residuals at each iteration, Ricardo R-Plot can be used.

### 4.2.2 Model Creation

Geometry Preparation

First, the modeled geometry of the system, including the cylinder head, valves, cylinder liner, and piston face at top-dead-center exhaust stroke were imported into VECTIS Phase 1. All unnecessary geometries such as the exterior (i.e. non-flow contacting) geometries of the cylinder head, were removed using the *trimming* tool. Any holes or missing geometries were sealed using the *hole fill* tool. An example of the geometry before and after trimming is shown in Figure 58.

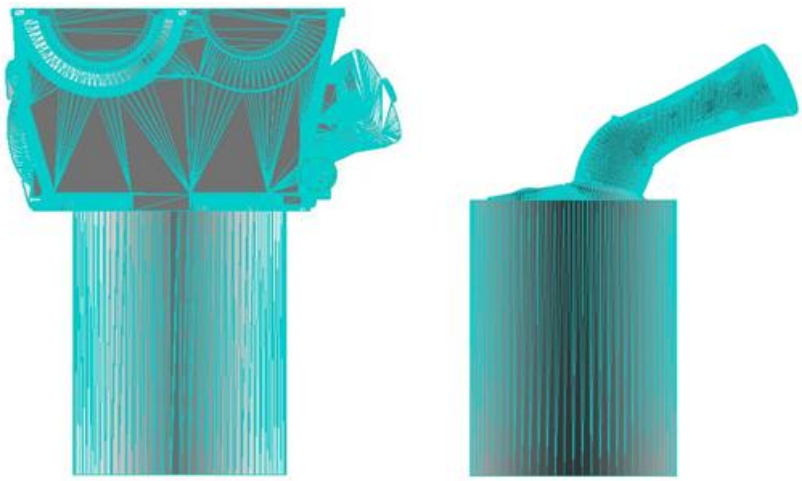

(A) (B)

*Figure 58.* Original geometry (A) and geometry after trimming (B)

Three main geometry files were created for the transient analysis. The first geometry, corresponding to top-dead-center (TDC) exhaust stroke, included the intake and exhaust

runner and valve assemblies. At 16 degrees after TDC (exhaust stroke), the exhaust valve is closed and a new geometry was created with the exhaust runner and valve stem removed. The exhaust valve face in contact with the in-cylinder flow was retained. The final geometry created corresponded to 220 degrees after TDC (exhaust stroke) when the intake valve has closed. The process followed for exhaust valve closing was repeated for the closing of the intake valve. This final geometry was used through the end of the compression stroke (i.e., until TDC compression).

Once the initial geometries had been prepared, the boundaries were defined using the boundary painting screen. Boundaries for the intake and exhaust runner, intake inlet and exhaust outlet, intake and exhaust valve stem and valve body/face, cylinder head combustion face, piston face, and cylinder liner were defined. The type of boundary (i.e. wall or inlet/outlet) was also defined. If the boundary was in motion throughout the cycle, such as the valve bodies/faces and piston face, the direction vector and displacement as a function of crank angle was specified. The boundary specifications are shown in Figure 59. The three aforementioned geometries at 0, 16, and 220 degrees after TDC exhaust stroke, with painted boundaries are shown in Figure 60, Figure 61, and Figure 62 respectively.

The geometries at crank angle locations in-between the three main geometry files were generated automatically during the mesh generation process. This will be explained in greater detail in the next section.

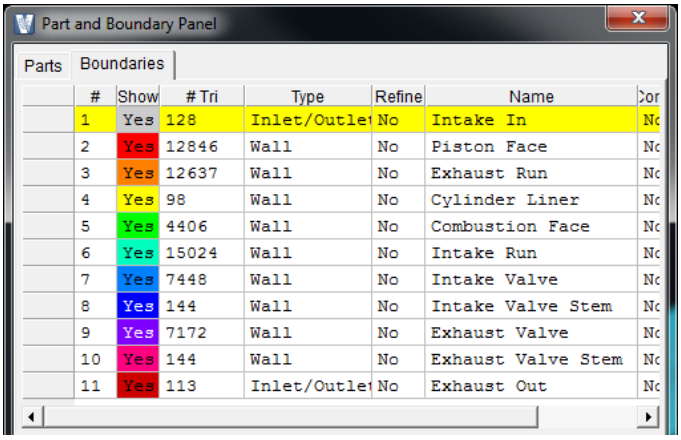


*Figure 59.* Boundary painting input screen

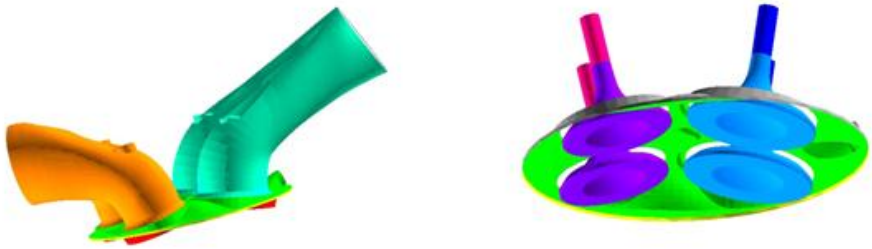

*Figure 60.* VECTIS boundary setup for transient analysis for partially open valves at TDC

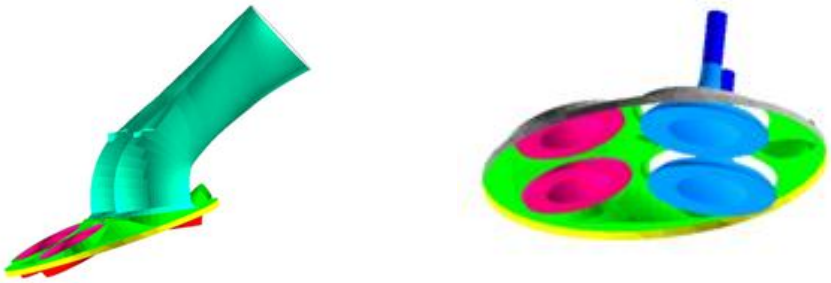

*Figure 61.* VECTIS boundary setup for transient analysis with intake valve at maximum lift

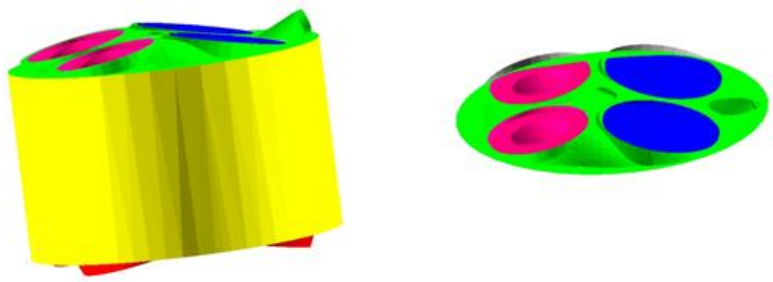

*Figure 62.* VECTIS boundary setup for transient analysis with both valves closed during compression

Mesh Generation and Validation

Mesh creation is also done through Phase 1 of VECTIS. Overall mesh size, localized mesh refinement, and boundary refinement can be specified. An example of a uniform mesh with no refinement is shown in Figure 63. The meshing process is then launched either directly from Phase 1 or through a batch file command and the meshing of the geometry is done in background processes (Phase 2 and 4). The meshed geometry is then saved in a separate file that can be loaded by the solver (Phase 5).

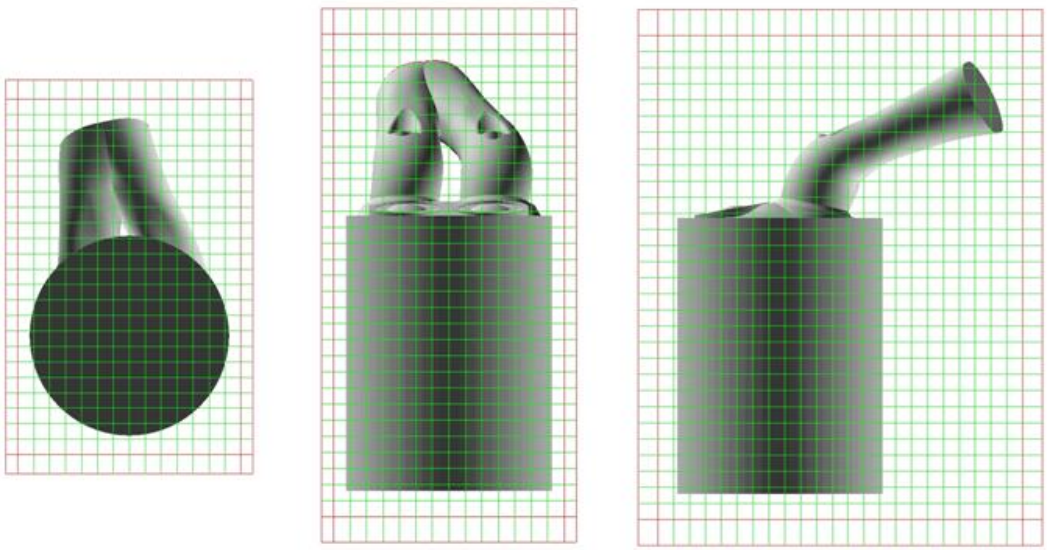

*Figure 63*. Example of a uniform mesh applied to the engine geometry

Before a mesh for the transient model of the intake and compression strokes could be developed, a mesh convergence study and validation was conducted using a simplified steady state model. This steady state case was validated through a physical test conducted using a Super Flow model 110 flow bench. The physical test conditions were at maximum valve lift and a known pressure drop across the inlet and outlet boundaries, using atmospheric conditions at the inlet and a vacuum at the outlet. Volumetric flow rate was measured and a mass flow rate was calculated based on measured atmospheric test conditions. The physical test was then modeled as a mass flow rate-driven solution within the simulation. A variety of uniform and non-uniform mesh sizes with and without boundary refinement were tested. It was found in this study that a 7.5mm uniform mesh provided the most accurate results with an average error of 8.1% at the exit boundary.

With the mesh criteria specified of uniform 7.5mm spacing, meshing of all the necessary geometries was conducted through a single batch file. The meshing process automatically positions the moving boundaries at the correct location for the requested crank angle time step before the mesh is applied. The number of geometries and their time step locations are based on a used specified cross-link criteria. The spacing of the geometries varies based on specific events through the cycle and is explained in more detail in section 4.5.1

Solver Setup

Once the meshes were created, the solver parameters needed to be setup within Phase 5. This included simulation timing information, solver algorithm selection, and iteration/convergence criteria. The settings used for the preliminary study are shown in Figure 64. The transient four-stroke model was specified, along with the engine speed of 5,000 RPM, start time of 0 crank angle degrees (TDC intake), end time of 365 crank angle degrees, and time step 0.5 crank angle degrees. Per the VECTIS user manual suggestion for transient simulation, the pressure correction solver and PISO algorithm were selected. A convergence criteria of 1e-006 was specified with five iterations per step.

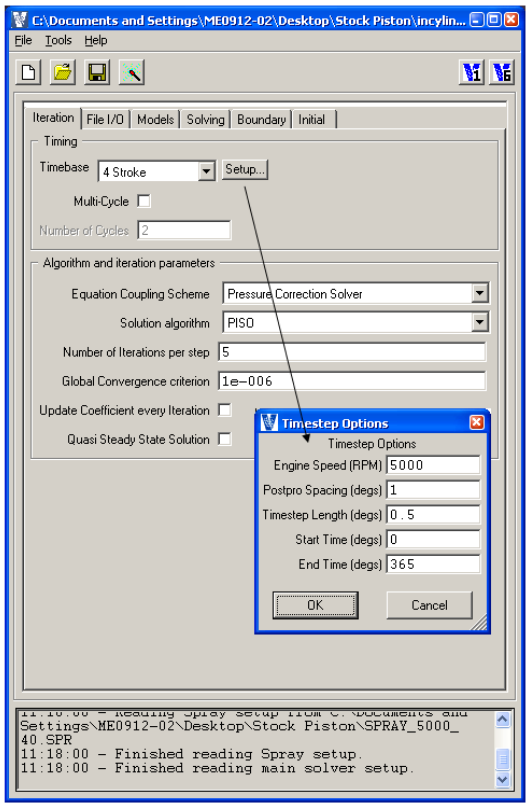


*Figure 64.* VECTIS input screen – iteration timing and time step options

Next, under the File I/O tab, the monitoring point(s) for the simulation was specified. A point just after the entrance of the intake and a point located within the combustion chamber near the exhaust valve were specified. These locations were suggested by the VECTIS user manual.

Finally within the Model Tab, the cross linking time regions are defined. For each meshed cross link geometry, the corresponding file name, and start time within the cycle in crank angle degrees relative to top dead center intake was specified. The direction of travel was also indicated, forward being TDC towards BDC, and reverse being BDC towards TDC during the cycle. These direction specifications are used to pre deform the mesh between geometry files. In the forward direction, the mesh is stretched while in the reverse direction the mesh is compressed. The cross-link time (specified in crank angle degrees) and direction are shown in Figure 65.

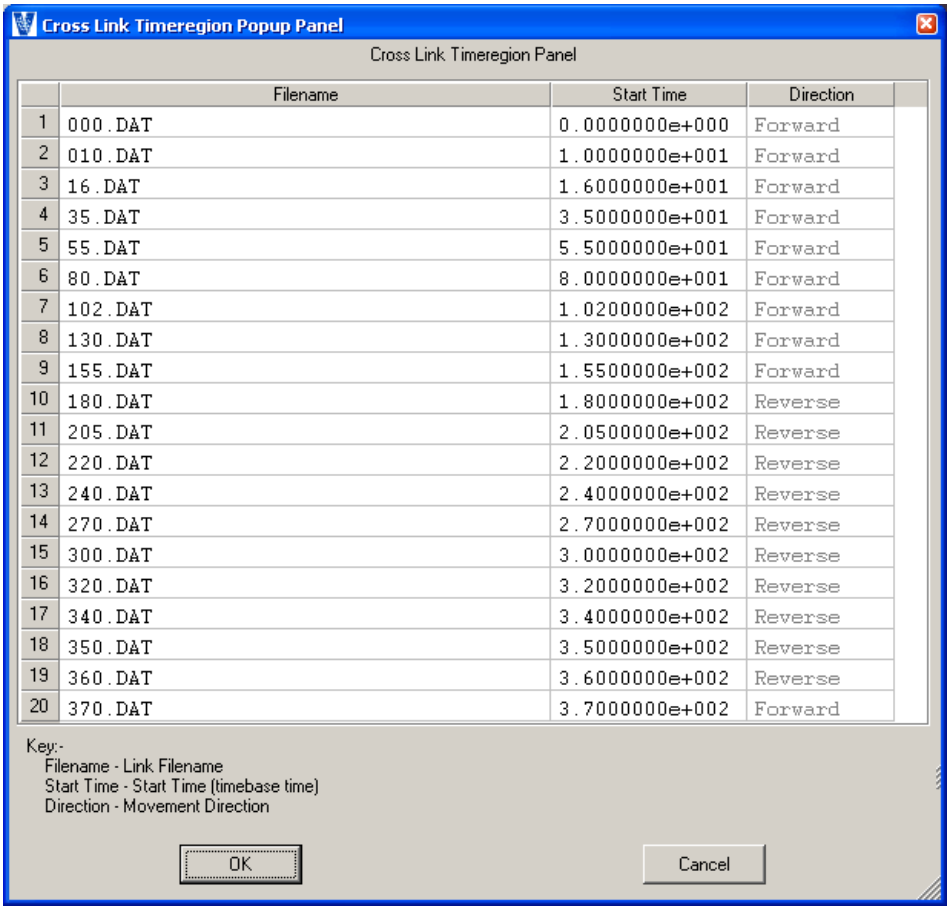


*Figure 65.* VECTIS input screen – cross link timeregion construction

Boundary Motion and Conditions

As mentioned in the geometry preparation section, the piston face and valve face/body are moving boundaries. Boundary motion inputs were specified within the Boundary Motion Option in the Models Tab. Also, boundaries that are connected to both a stationary boundary and moving boundary, such as the cylinder liner and valve stem are also specified within this option. Piston Motion was specified for the piston face and is specified by the engine connecting rod length and stroke (Figure 66 A). Interpolated Displacement was specified for the cylinder liner because the cylinder length changes

through the engine cycle. The cylinder liner was interpolated between the stationary combustion face boundary, and the moving piston face boundary. Prescribed Displacement Motion was specified for both the intake and exhaust valve face/body boundaries (Figure 66 B) and linked to the respective valve motion files. Prescribed displacement is utilized because these boundaries are time-dependent motions relative to crank angle.

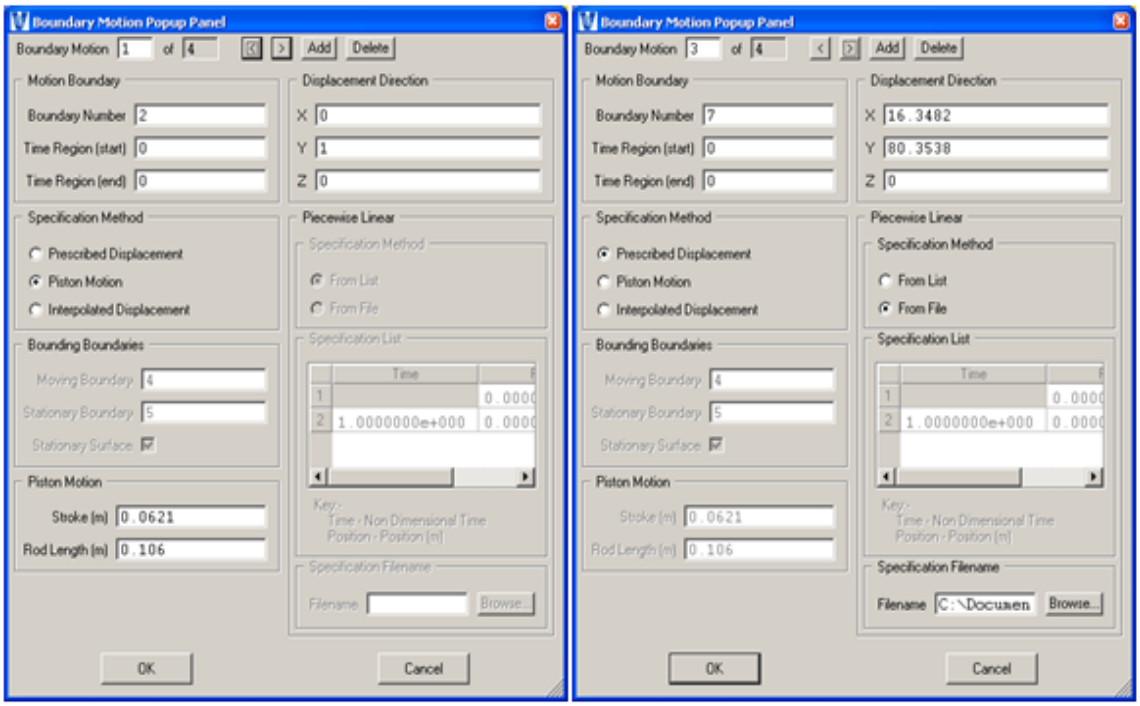


*Figure 66.* VECTIS input screen – boundary motion controls

The boundary conditions are specified within the Boundary Tab. For the inlet and outlet boundaries, mass flow rate as a function of time and a static pressure of atmospheric (100 kPa) respectively, were specified. The mass flow rate boundary was based on a one-dimensional engine simulation output also conducted as part of the preliminary study, as no other physical data was available for the engine at that time. The mass flow rate was

specified at 16 time steps throughout the intake cycle. To smooth the transition in mass flow rates between each specified time step, the mass flow ramp option was used.

Finally, the wall conditions were specified for all the boundaries in contact with the air flow. Because the temperatures for each wall boundary were unknown, default values provided by the VECTIS user manual were used.

Initial Conditions

Default initial conditions (100 kPa and 500 K) were used for the simulations in the preliminary study, as no physical data were available for the specific engine at the time. These conditions were applied throughout the system.

Sub-Models: Turbulence and Injection Modeling

The Sub-Model tab allows outside solution models such as spray, combustion, and turbulence to be activated. For this study the turbulence and spray models were used. The k-epsilon turbulence model was used with the simulation default constants. The constants values are shown in Figure 67.

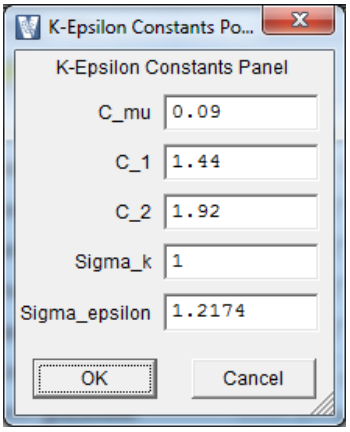


*Figure 67*. Simulation default K-epsilon turbulence model constants

The spray model input screen is shown in Figure 68. Here the fuel type is specified, as well as the break up and impingement models. Because these specifications where unknown for the Bosch injector chosen, the default values specified by Ricardo were used.

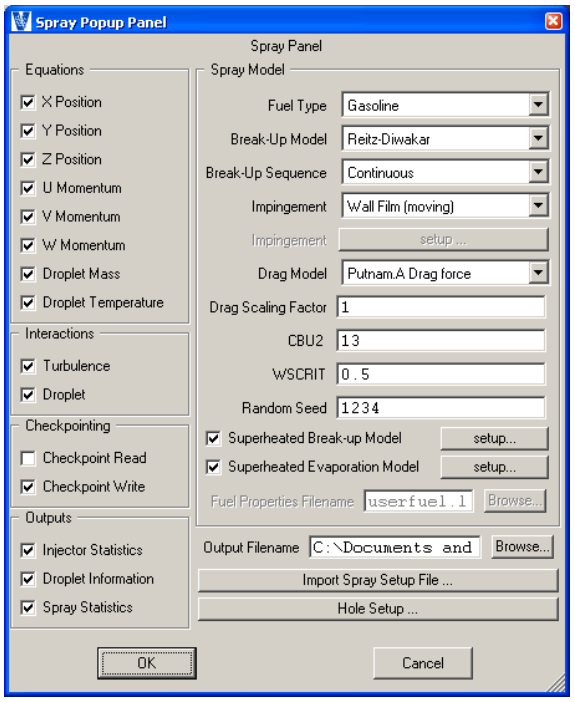


*Figure 68*. VECTIS input screen – spray model definition

Within the *injector hole setup* option in the *spray* panel, the location of the injector was specified, as well as direction vector, cone angles, injector hole radius and length-to-diameter ratio. This was specified for all six holes of the injector. Next, the droplet distribution was specified under the Droplet Tab in terms of droplet size in meters, and the probability this droplet would occur. These data were not available for the injector chosen, so the default values provided by Ricardo were used. Under the Injection Tab, the mass of fuel to be injected for each hole was specified. This mass was equivalent to what would be injected in a port-fuel-injected system at the simulated speed and load. The mass used was based on one-dimensional engine simulation that was also developed during the preliminary study, as physical test data was unavailable. Figure 69 shows the parameters specified for *hole one* for the respective tabs.

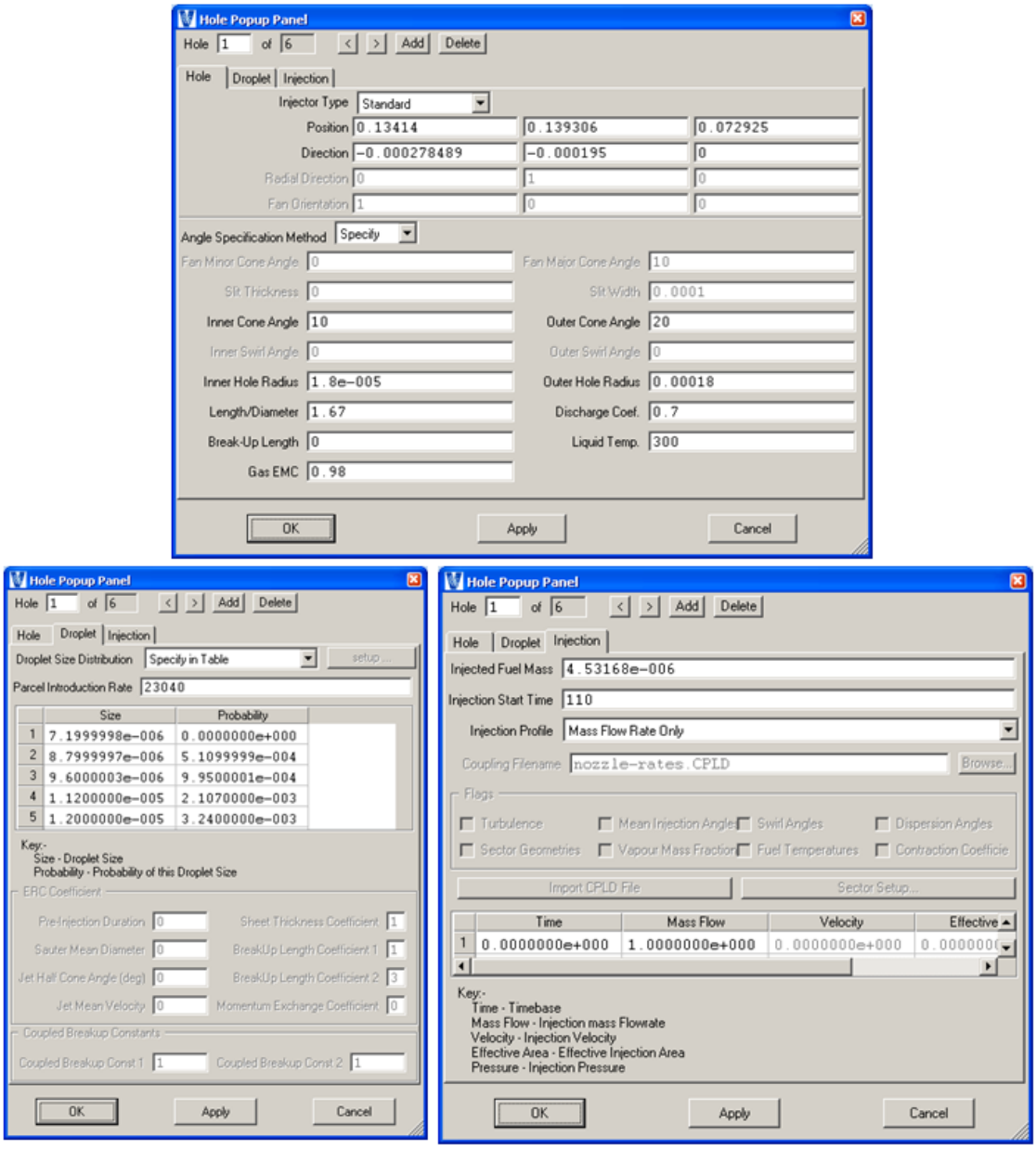


Figure 69: VECTIS input screens – injection parameters (hole size, fuel mass, and droplet sizing)

## 4.3 Results of Preliminary Design Efforts

Having created and meshed a model for the single-cylinder engine within the constraints highlighted in the previous section, transient analysis was conducted using Ricardo VECTIS to evaluate the effect of injection angle and piston head design on fuel-air mixing. The following was determined:

### Injection Angle

The injector would be placed underneath the intake runner and parallel to the centerline to minimize modifications to the stock cylinder head. It was determined by the results of the preliminary transient model that an injection angle of 40 degrees from the horizontal provided the lowest global air-fuel ratio (i.e., richest fuel-air mixture) and lowest fuel loss due to wall sticking (Figure 70) for the same mass of fuel injected. This indicated better fuel-air mixing and the highest potential for increasing the engine's fuel efficiency.

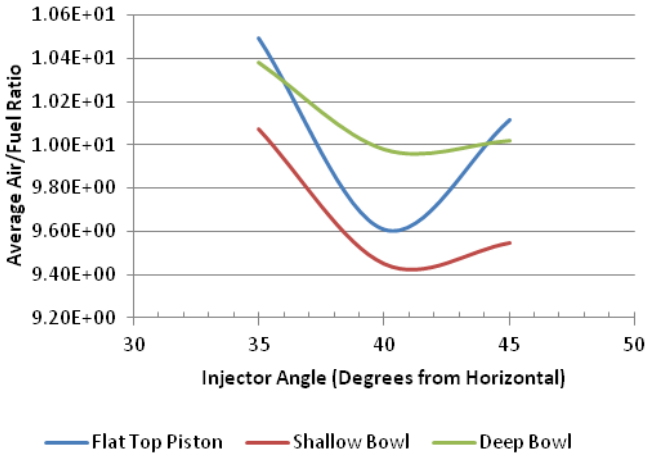


(A)

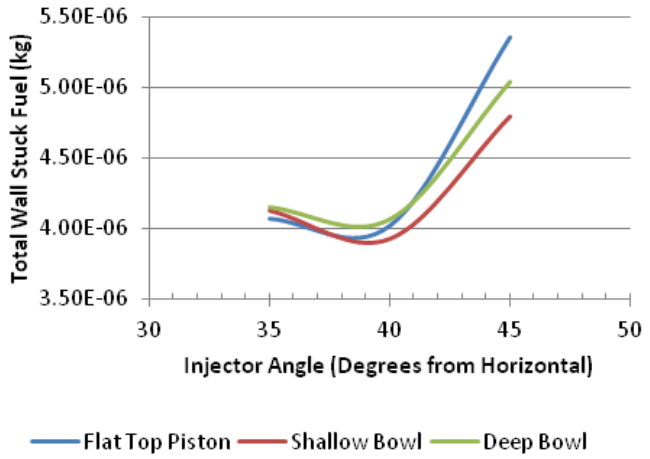


(B)

*Figure 70*. Global air/fuel ratio (A) and total wall stuck fuel (B) for varying injection angles and piston designs: WOT at 5,000 RPM

Piston Head Design

Also based on results shown in Figure 70, a shallow bowl piston design was chosen, as it provides the least amount of fuel accumulation, while enhancing fuel/air mixing. This was determined from the observation that the shallow bowl piston produced the least amount of total fuel loss to wall sticking (B) and providing the richest average air fuel ratio (A), which indicated that more fuel had mixed with the air within the cylinder. This decrease in fuel accumulation enables decreasing the total fuel supply needed to operate the engine. When compared to the fuel supplied to the port-fuel-injected system, the new direct-injection system fuel requirement resulted in a theoretical, maximum increase of 12.5% in fuel efficiency. Figure 71 shows air-to-fuel ratio results from the shallow bowl piston design at 5,000 RPM engine speed. Toward the beginning of the compression stroke (220 crank angles after TDC-intake), the injected fuel has reached the piston bowl. As the compression stroke continues, this fuel is forced back into the chamber. At 290 crank angle degrees, only a small amount of fuel accumulation can be seen in the corner of the cylinder opposite to the injection side. The final picture shows the air-to-fuel ratio of the optimized design before spark ignition. The air to fuel ratio is slightly rich (9.45:1), suggesting there are opportunities for reducing the amount of fuel injected. This decrease in fuel accounts for the fuel efficiency increase. The shallow bowl piston was also designed to incorporate the desired maximum compression ratio of 14.0:1.

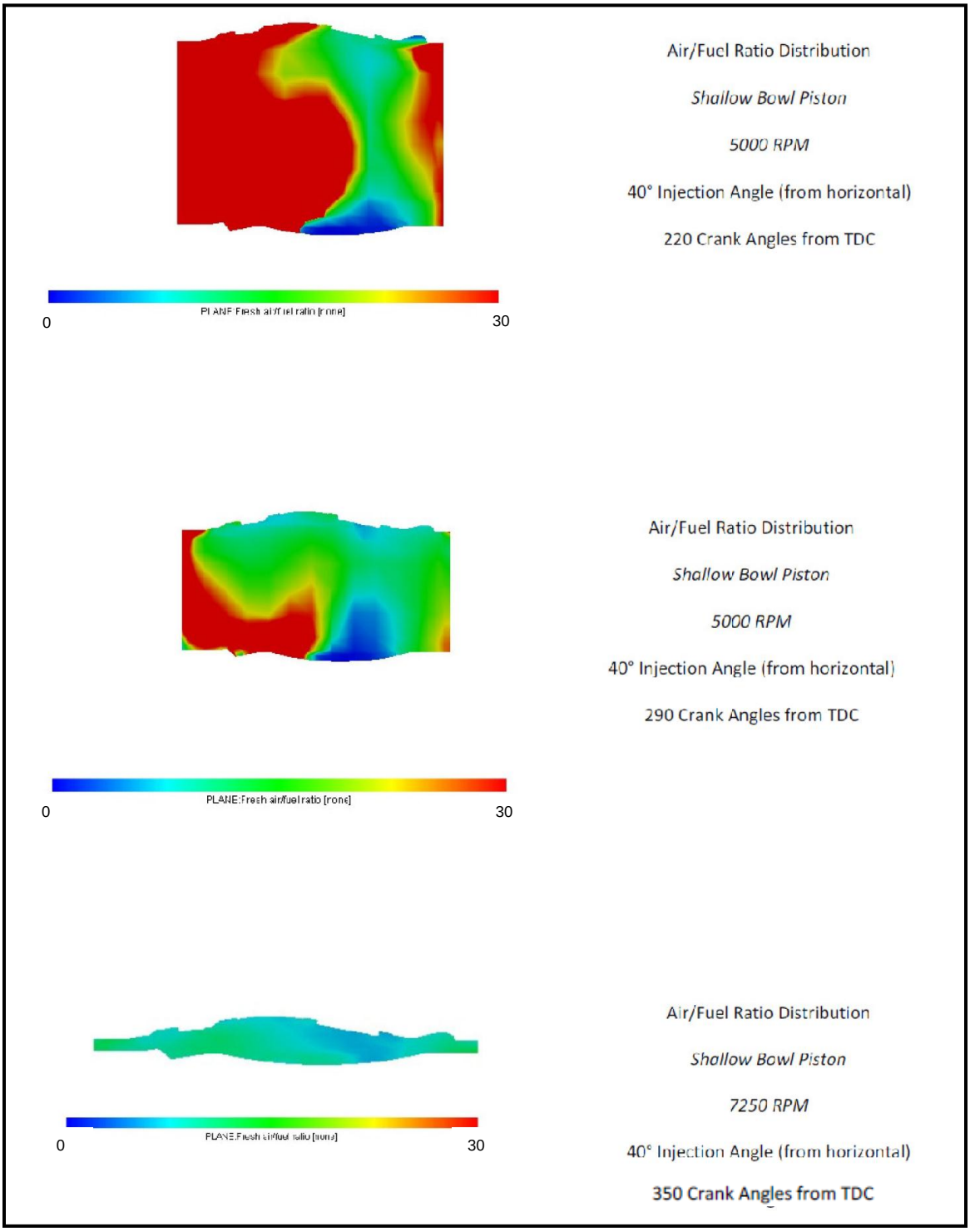


*Figure 71.* Shallow bowl piston with injection angle of 40 degrees, 5000 RPM and varying crank angles.

Additional Findings

As described in sections 4.1.3, preliminary analysis indicated that the compression ratio could be increased to 14.0:1 based on both geometric and knock-limit constraints. The effect of this new compression ratio on engine torque and power was then compared to those obtained with the original (12.2:1) compression ratio of the stock RM-Z450 engine. The increase from 12.2:1 to 14.0:1 led to a 4% increase in engine power, from 48 HP (35.8 kW) to 50 HP (37.3 kW). In a similar fashion, the torque of the engine was increased by approximately 2.5% (from 32.75 ft-lbs (44.4 N-m) in the port-fuel-injection design to 33.5 ft-lbs (45.4 N-m) for the direct-injection design). These results are shown in Figure 72. While modest increases in torque and power were predicted, it was useful to discover that the potential gain in fuel efficiency did not result in a performance penalty.

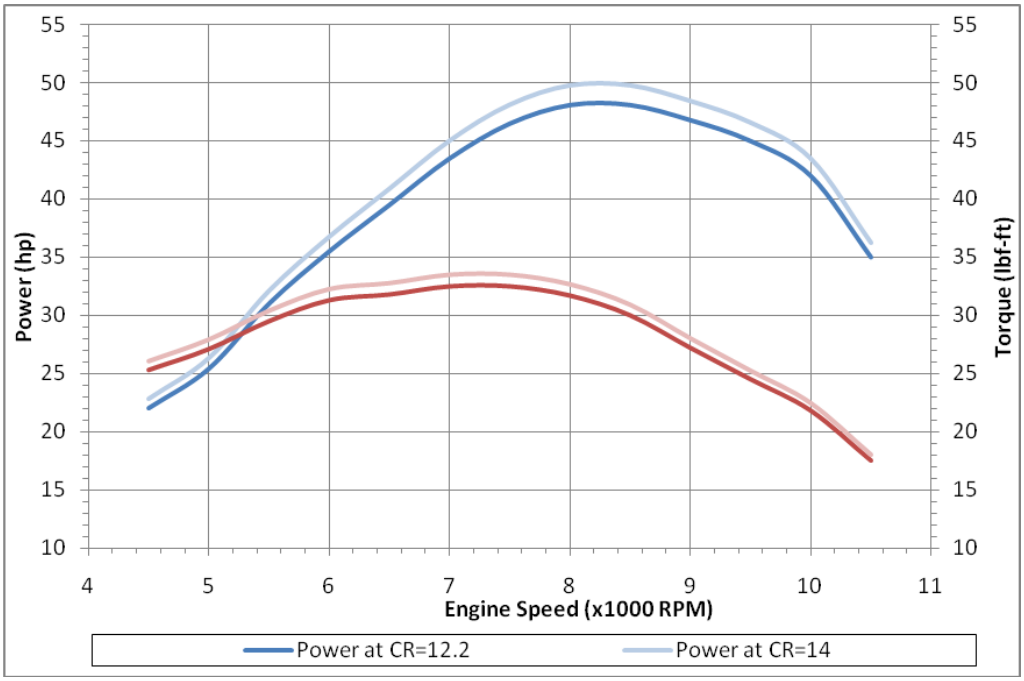


*Figure 72.* Torque and power curves showing the advantage of increasing the compression ratio from 12.2 to 14.0

## 4.4 Opportunities for Improvement

The preliminary study described in sections 4.1 through 4.3, conducted prior to physical tests, revealed important qualitative trends. Any further design improvements required that the engine model be refined. The following areas required further attention:

- Geometry cross-linking
- Boundary and initial conditions
- Mesh size refinement

One of the problems identified was lack of validation against physical data, including in-cylinder pressure throughout the cycle and mass of air inducted. This lack of physical test data led to the assumption of many temperature and pressure boundary conditions. These values were assumed based on suggestions found in the simulation tutorials (15). Although all the estimated boundaries could not be measured during physical testing, the intake and exhaust runners surface temperatures, pressure and temperature at the intake and exhaust manifold boundaries, and cylinder wall surface temperature were quantified. A detailed list of these parameters and corresponding measured values are presented in Table 15 and Table 16 of section 4.5.2.

The previous simulation specified a mass flow rate-based solution rather than a pressure based solution. The mass flow boundary conditions were chosen as they were easier to converge when compared to pressure-driven solutions and were more forgiving to mesh and boundary condition errors. The values used for the mass flow boundary conditions

were based on the simulation values from the Ricardo Wave modeling. At the time of the preliminary simulations, it was recognized that a pressure-driven solution using measured boundary conditions was a more realistic representation of the physical system.

The preliminary simulation was computationally limited in regards to mesh size and time step due to the limited computing power available during the initial study. Only single-processor calculations and limited memory were available, which resulted in extensive computational time (6-8 hours per test case?). While needed at the time, finer mesh sizes and crank angle time steps could not be practically implemented due to lack of computational resources.

## 4.5 Simulation Refinement

### 4.5.1 Test Case Definition and Background

In order compare directly with results from a preliminary study, the shallow bowl piston geometry with an injection angle of 35 degrees was used at an engine speed of 5,000 RPM. This provided a case that was both previously simulated in the preliminary study and a test condition recorded in during physical testing. As in the preliminary study, only the intake and compression strokes were analyzed. The specifications of the computer used in the previous study were not documented and therefore no comparison between computational effort between the refined and preliminary study will be made. Specifications for the Dell Precision T3500 used for the refined study are shown in Table 13.

*Table 13.* Specifications of computer used in refined-model investigations

| **Dell Precision T3500** | |
|---|---|
| **Operating System** | Windows 7 64 Bit |
| **Processor** | Intel(R) Xeon(R) W3670 |
| **Processor Cores** | 6 |
| **Processor Clock Speed** | 3.20 GHz |
| **Processor Cache** | 12MB |
| **RAM** | 12.0 GB |
| **RAM Type** | DDR3-800/1066 |
| **Hard Drive Speed** | 7200 RPM |
| **Hard Drive Size** | 1 TB |

4.5.2 Cross Link Refinement

Background and Strategy

Upon reviewing the previous study, it was recognized that no validation of the cross link strategy had been conducted in regards to mesh distortion. The term *cross-linking* refers to the re-zoning of the solution from one mesh file to another. It is used in situations that involve a moving boundary (e.g., piston) such as found in the present study. The overall solution time range is divided into regions in which a single meshed geometry is applied (e.g., top dead center of the intake stroke corresponding to? $t_1$=0 crank angle degrees). For the next time step of the simulation, (i.e. a crank angle of $t_2=t_1+0.5$ degrees), the cells of this meshed geometry are stretched to the new boundary (e.g. valve and piston) position. This stretching process is repeated until the next specified cross link location is reached. At this point, the solver saves the current solution to a temporary file. The new, un-distorted meshed geometry at the new cross-linked location is loaded, and the nearest equivalent cells are determined between the old and new meshed geometries. The solution is then re-applied from the temporary file.

A potential source of error within this process is mesh distortion, which causes poor transition from one mesh file to the next and results in poor convergence and calculation errors. During the previous study, the VECTIS-recommended strategy was used. This strategy consisted of cross linking:

- Every 10 degrees during valve opening
- Every 20 degrees during valve closing
- Every 10 /20 degrees as piston approaches TDC during the compression stroke

- Every 30 degrees elsewhere in the cycle
- At maximum valve lift
- At valve closing

It was noticed during post processing that the geometry within the animations exhibited sharp transitions. This effect was attributed to mesh over-distortion. A more refined strategy was defined according to the following criteria:

- No greater spacing in crosslink's than 10 degrees throughout the cycle.
- Crosslink's every 2-5 crank angle degrees when the mesh is approaching TDC or valve closing

A comparison between the previous and new strategies is shown in Table 14. Points marked with a letter *S* represent those that are the same between the two strategies, points marked with a letter *N* represent new cross links, and those marked with a letter *R* represent those included in the previous study, but removed in the new one. The previous study contained 20 cross link locations, while the newest study contains 54 cross link locations.

Table 14. Ricardo VECTIS cross link strategy comparison (N=New, S=Same, R=Removed)

| Ricardo VECTIS Cross Link File Strategy | | | | | |
|---|---|---|---|---|---|
| Crank Angle [Deg] | N,S,R | Significant Events | Crank Angle [Deg] | N,S,R | Significant Events |
| 0 | S | TDC Intake | 205 | S | |
| 5 | N | | 210 | N | |
| 8 | N | | 213 | N | |
| 10 | S | | 216 | N | |
| 12 | N | | 218 | N | |
| 14 | N | | 220 | S | Intake Valve Closed |
| 16 | S | Exhaust valve Closed | 230 | N | |
| 20 | N | | 240 | S | |
| 30 | N | | 250 | N | |
| 35 | R | | 260 | N | |
| 40 | N | | 270 | S | |
| 50 | N | | 280 | N | |
| 55 | R | | 290 | N | |
| 60 | N | | 300 | S | |
| 70 | N | | 310 | N | |
| 80 | S | | 320 | S | |
| 90 | N | | 330 | N | |
| 102 | S | Max. Lift Intake Valve | 340 | S | |
| 110 | N | Fuel Injection Started | 345 | N | |
| 120 | N | | 350 | S | |
| 130 | S | | 353 | N | |
| 140 | N | | 356 | N | |
| 150 | N | | 358 | N | |
| 155 | R | | 360 | S | TDC Compression |
| 160 | N | | 362 | N | |
| 170 | N | | 364 | N | |
| 180 | S | BDC Intake Stroke | 367 | N | |
| 190 | N | | 370 | S | |
| 200 | N | | | | |

As part of this work, mesh distortion data were also extracted from the simulation output file and examined for excessive distortion values. The three main measures of distortion are stretch, angular distortion and cross over. Stretch is the fractional amount by which the lines between two points change size. Positive and negative values represent expansion and compression, respectively. Values that approach -1 are considered highly compressed and may be cause for concern. Angular distortion measures the distortion of paired lines originally perpendicular to one another. This distortion is measured in values of cosine, where values within the range of + 0.95 are considered acceptable. A value of +1 indicates a highly skewed mesh that should be corrected. The last measure of mesh distortion is crossover, of which there are two types. Cross over type-one is when two lines parallel to each other with a central common point crossover this central point, and point in the same direction. Values between cosine -1 and 0 are considered acceptable, values between cosine 0 and +1 require refinement. The second type of crossover occurs when the displacement of one of two neighboring points connected by a single line moves past the second point. This is measured as fractional relative displacement in the parallel direction, based on the initial separation distance of the two points. Positive values indicate points are moving away from one another, and negative values indicate the points are moving towards one another. Values less than -0.8 are considered acceptable, while values between -0.8 and -1 indicate that refinement is required.

Refinement Results

The extreme values (minimum and maximum) of mess distortion were examined to identify specific points in which high distortion occurred. The mean value of mesh distortion was used to judge the overall quality of the mesh. As mesh size influences the values of mesh distortion, (i.e., smaller mesh is stretched more for the same boundary displacement), the same mesh spacing was used in both studies in order to provide a direct comparison of the improvements made by the refined cross-link strategy.

Shown in Figure 73 and Figure 74 are the linear distortion results for the preliminary and refined simulations, respectively. Several peaks of over 10,000 in linear distortion rate occurred within the preliminary study, while these extreme values were eliminated in the refined study. The overall mesh quality was improved in the refined study, as indicated by the reduced mean and standard deviation values of linear distortion rate. The large deviation observed at the later portion of the simulation may be attributed to the highly compressed mesh at the end of the compression stroke and warrants further investigation.

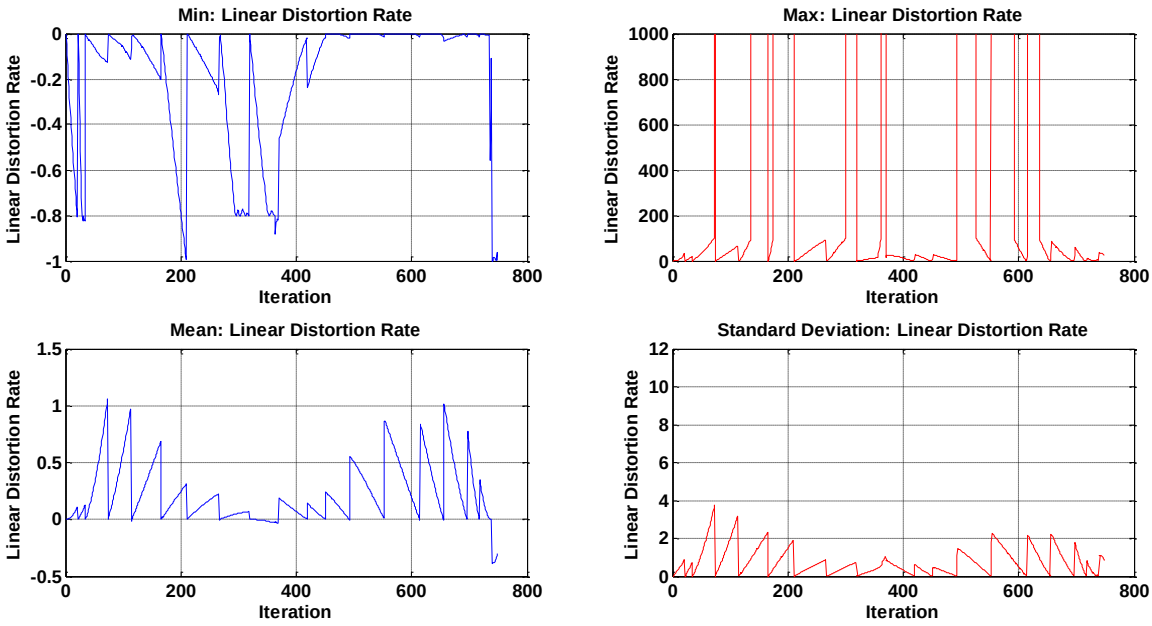


*Figure 73.* Linear distortion rate results from preliminary study

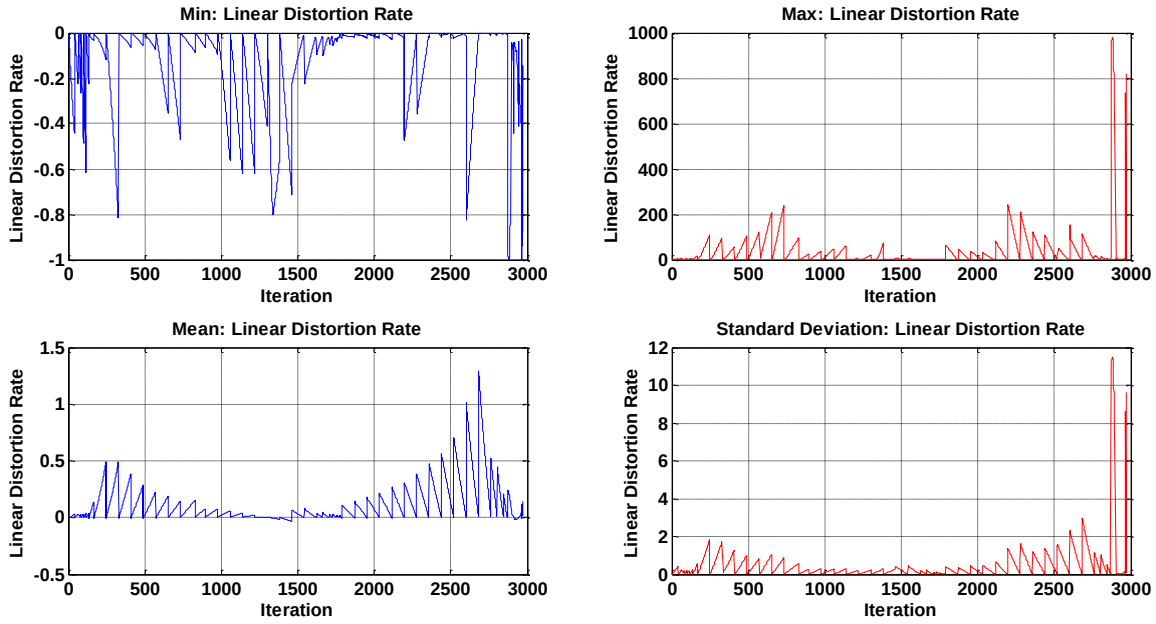


*Figure 74.* Linear distortion rate for refined simulation

Shown in Figure 75 and Figure 76 are the angular distortion results for the preliminary and refined simulations, respectively. As explained above, values outside the range of ± 0.95 are considered highly skewed. Although not completely eliminated, the occurrence of distortion outside of this criteria range was reduced from 10 to 4 in the refined simulation. The overall mesh quality was improved in the refined study, as indicated by the reduced mean and standard deviation values of angular distortion rate.

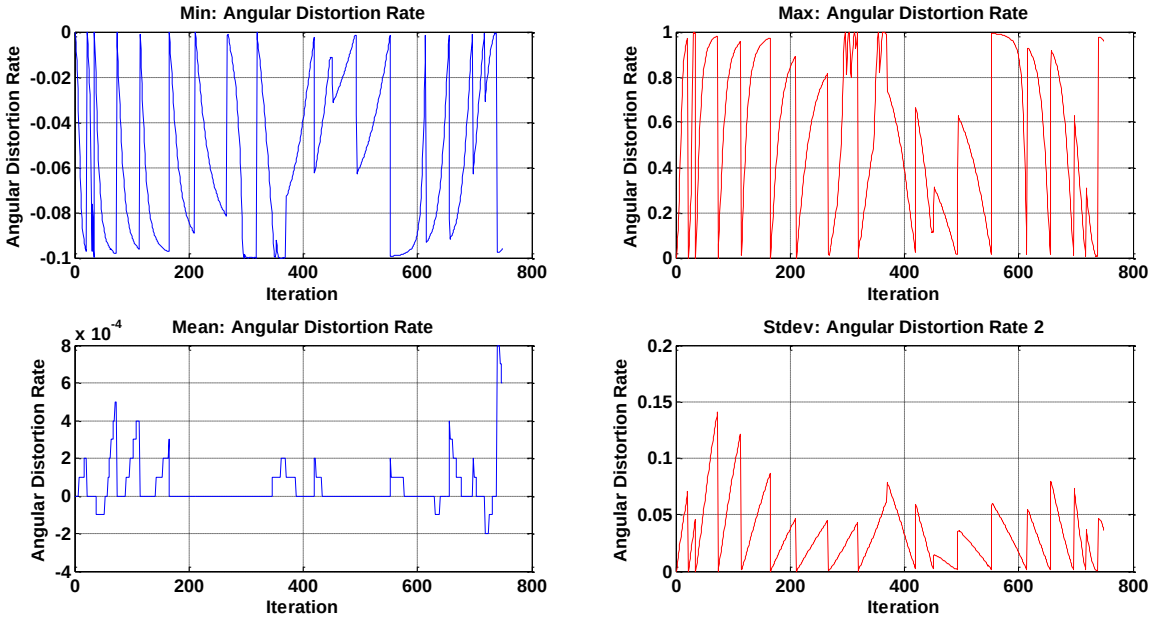


*Figure 75.* Angular distortion rate for preliminary study

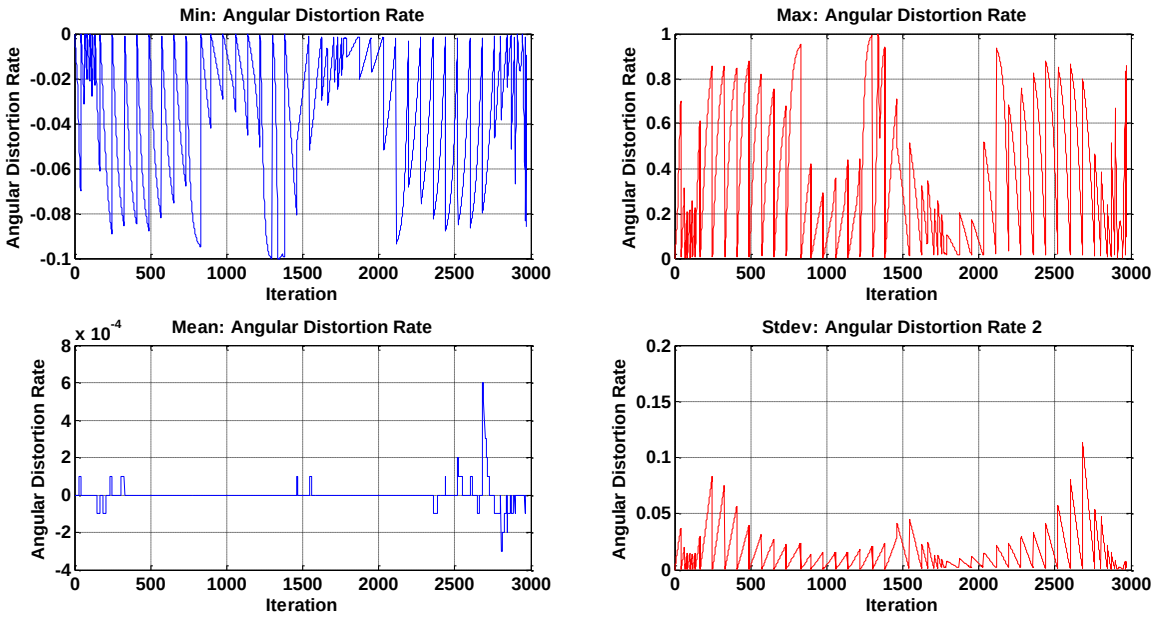


*Figure 76*. Angular distortion rate for refined simulation.

Shown in Figure 77 and Figure 78 are the cross motion type-two distortion results for the preliminary and refined simulations, respectively. It should be noted values greater than -0.8 are considered acceptable while values between -0.8 and -1 indicate refinement is required. The refined study reduced the occurrences of the violation of these criteria from 5 to 3. Although not critical criteria, it should be noted that the values of maximum, mean, and standard deviation in cross motion type two distortion were also reduced, indicating an overall improvement in the refined study.

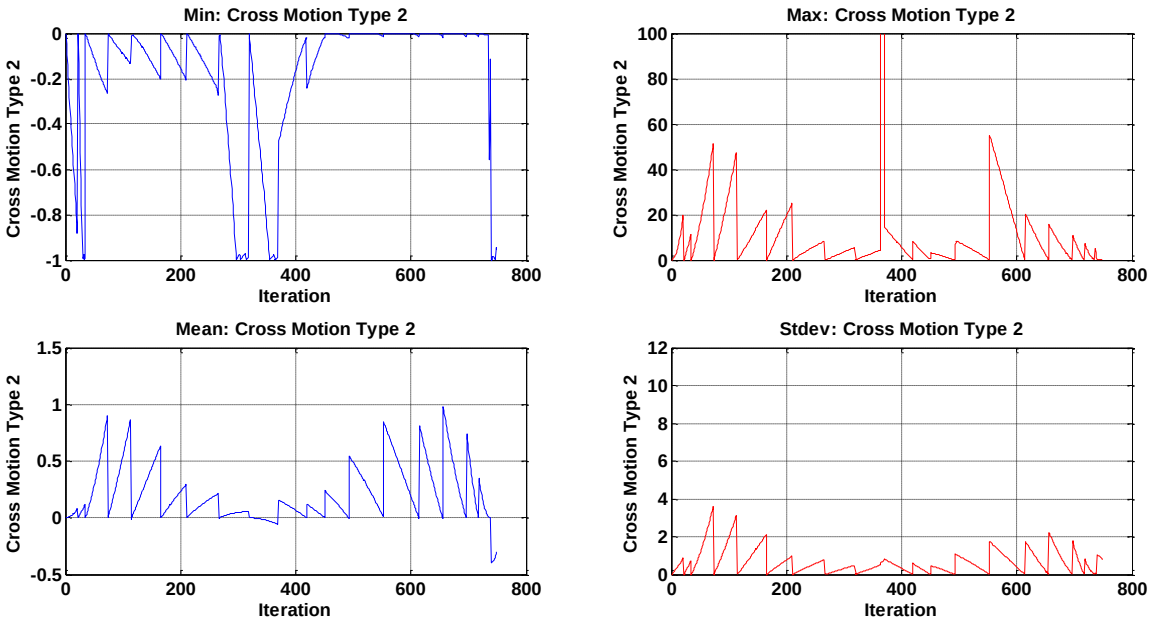


*Figure 77*. Cross motion type-two results for preliminary simulation

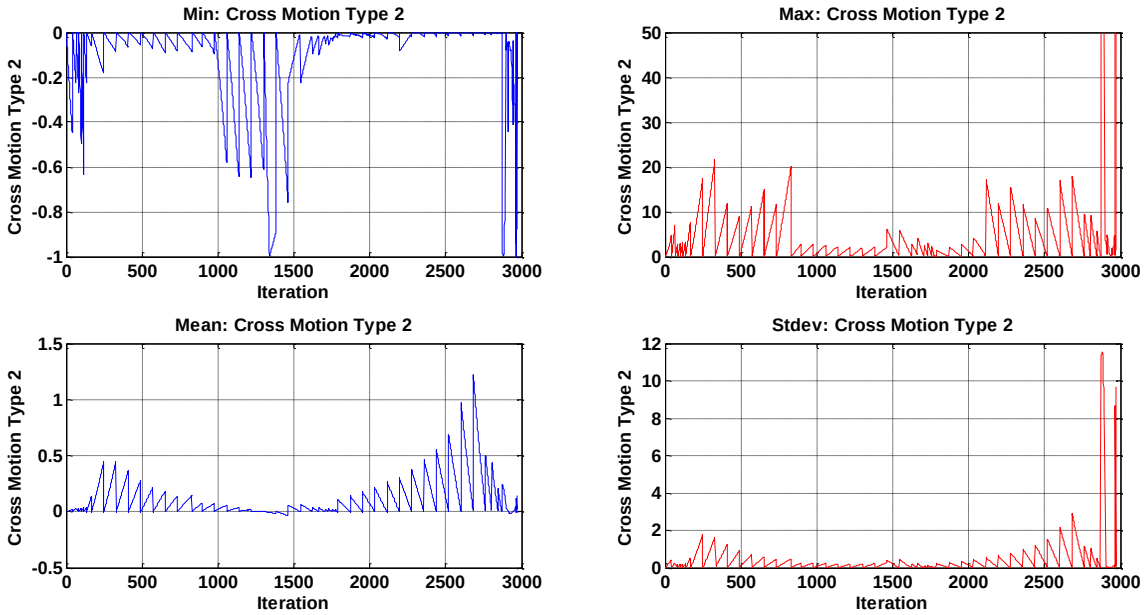


*Figure 78*. Cross motion type-two results for refined simulation

### 4.5.3 REFINEMENT OF BOUNDARY AND INITIAL CONDITIONS

The boundary and initial conditions used in the previous study were either estimated or specified as default in Ricardo VECTIS. In order to better represent the physical system, boundary data obtained from the engine benchmarking study were implemented. The in-cylinder pressure value at top-dead-center (intake stroke) was specified as initial condition. Table 15 shows that the measured value was 95,343 Pa, compared to the default value of 100,000 Pa.

*Table 15*. Initial condition comparison: WOT @ 5,000 RPM

| **Initial Conditions** | | |
|---|---|---|
| **Condition** | **Default simulation value** | **Measured value** |
| Pressure (Pa) | 100,000 | 95,343 |
| Temperature (K) | 500 | N/A |

Boundary conditions are shown in Table 16. The measured values were recorded at steady state. The intake runner and cylinder liner temperatures are the average value of four data and three data points, respectively. Please refer to section 2.3 for location of corresponding temperature sensors. Although most values did not differ significantly from those used in the previous study, the exhaust runner surface temperature decreased by 419 K and the exhaust outlet boundary temperature increased by 689 K. The latter is attributed to the default suggested value being specified for a simple inlet/outlet boundary, but not specifically for an exhaust gas boundary, which has significantly higher temperature.

*Table 16*. Boundary condition comparison: WOT at 5,000 RPM

| Boundary Conditions | | | |
|---|---|---|---|
| **Boundary** | **Condition** | **Previously used value** | **Measured value** |
| Inlet (Intake Entrance) | Pressure | 100,000 | 98,414 |
| | Temperature (K) | 300 | 298 |
| Outlet (Exhaust Outlet) | Pressure | 100,000 | 103723 |
| | Temperature (K) | 300 | 989 |
| Piston Face | Temperature (K) | 520 | N/A |
| Exhaust Runner surface | Temperature (K) | 800 | 381 |
| Cylinder Liner | Temperature (K) | 475 | 351 |
| Combustion Face | Temperature (K) | 520 | N/A |
| Intake Runner surface | Temperature (K) | 300 | 328 |
| Intake Valve | Temperature (K) | 520 | N/A |
| Intake Valve Stem | Temperature (K) | 475 | N/A |
| Exhaust Valve | Temperature (K) | 1,000 | N/A |
| Exhaust Valve Stem | Temperature (k) | 750 | N/A |

### 4.5.4 Mesh Refinement

Setup

A mesh convergence study was conducted. The global mesh sizes tested included 7.5 mm, 6 mm, 4.5 mm, 3 mm, and 2 mm spacings. Localized mesh refinements for geometry boundaries and user-specified block locations were implemented, but it was found that these refinements caused the solution to become unstable. It is believed by the author that this occurs due to the sharp transition in cell size between the refined and unrefined domains, which causes errors between neighboring cells across this transition. Because of this, only uniform meshes were analyzed. The internal cell count for each mesh size at 180 CAD is shown in Table 17. This location was chosen as it was the largest computational volume throughout the simulation.

Results

First, the required computational effort was examined for each mesh size. All cases were run in series (i.e., single-core). Parallel (i.e., multi-core) processing was attempted and significantly improved computation time, but an unresolved file access error within the software only allowed computation to 220 of the 360 CAD. As would be expected, as mesh size was decreased and subsequently cell count increased, computational time increased. CPU usage remained constant, independent of mesh size. Memory usage however, did increase with decreased mesh size. The finest mesh (2mm) was automatically terminated at 179 crank angles due to a negative temperature found in subroutine 'calch' error. The cause of this error is suspected to be caused by a stability issue related to the ratio of time step to mesh size. This was not investigated, however, due to the extensive computational time required.

*Table 17*. Mesh convergence study results: cell count and computation effort

| **Mesh Convergence Study** | | | | |
|---|---|---|---|---|
| **Mesh Size [mm]** | **Number of Internal Cells at 180 CAD** | **CPU Usage** | **Memory Usage [MB]** | **Total Simulation Time [hr:min]** |
| 7.5 | 20481 | 17 | 65 | 2:38 |
| 6 | 32354 | 17 | 97 | 3:13 |
| 4.5 | 58603 | 17 | 141 | 4:15 |
| 3 | 137295 | 17 | 281 | 7:28 |
| 2 | 329103 | 17 | 613 | DNF |

The in-cylinder pressure as a function of engine crank position relative to top dead center (exhaust) is shown in Figure 79 for all mesh sizes. Figure (A) shows pressure throughout the entire engine cycle. The solid black line represents the experimentally measured pressure, whereas dashed lines correspond to the various mesh sizes. On the global scale shown in Figure 79(A), mesh size appears to have little effect on the in-cylinder pressure. It is also observed that deviations from experimental data exist from 50 to 100 crank angle degrees (CAD), 170 to 230 CAD, and from 260 CAD to the end of compression. This large deviation towards the end of compression may be attributed to the different compression ratios between the simulation test case and experimental testing (14.0:1 and 12.2:1 respectively). Figure 79(B) focuses on the in-cylinder pressures during the intake stroke (TDC exhaust to 220 CAD). The more refined pressure scale shows that, for all mesh sizes, the predicted in-cylinder pressure highly deviate from the experimental data. The highest deviation is found between 45 and 240 CAD. These findings suggest that the error in this region is independent of mesh refinement.

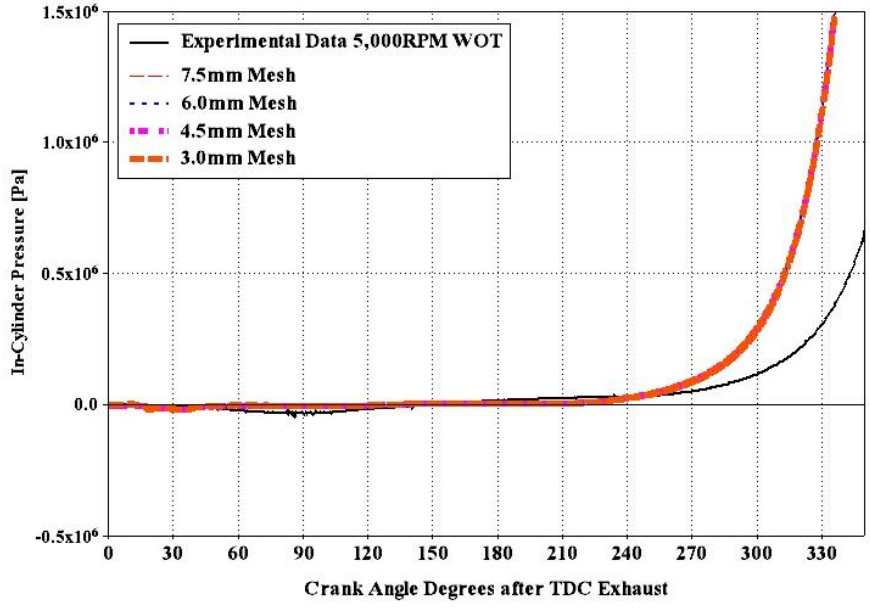


(A)

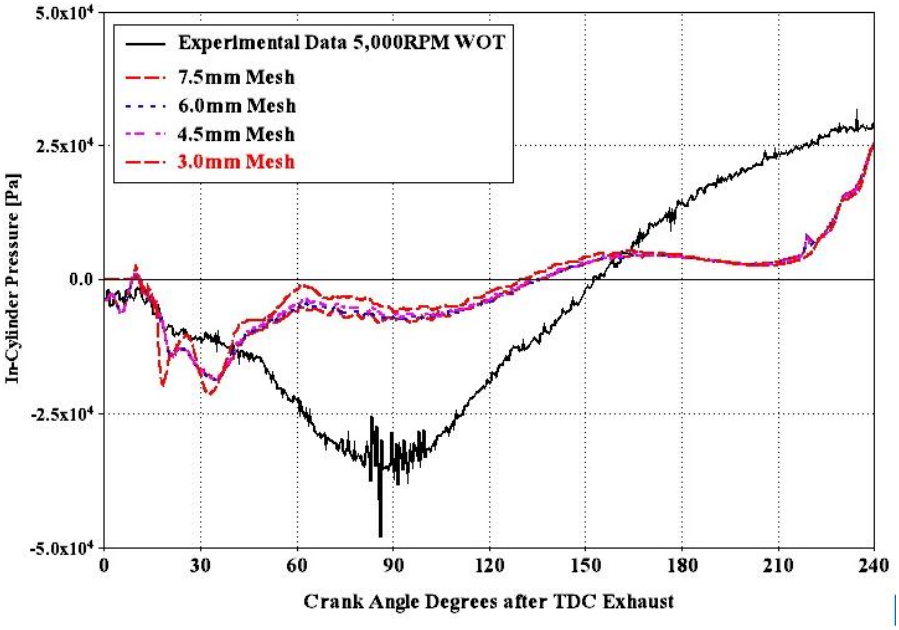


(B)

*Figure 79.* In-cylinder pressure for a range of mesh sizes compared to experimental results throughout the engine cycle (A) and only the intake stroke (B)

Figure 80 shows the global average of turbulent kinetic energy (tke) (A) and its dissipation rate (B) as a function of crank angle degrees after TDC (exhaust). The decrease in mesh size causes minimal variation in the model prediction of turbulent kinetic energy ($\pm$2 $m^2/s^2$) from zero to 115 CAD. Little variation is also observed from 135 to 330 CAD for the 7.5 and 6.0 mm meshes. From 135 to 360 CAD, the 4.5mm mesh predicts an increase in turbulent kinetic energy by approximately 6 $m^2/s^2$ with respect to the courser mesh sizes. A large increase in tke is observed for the 3 mm mesh starting at 100 CAD, with values approximately 15 $m^2/s^2$ higher than those predicted by coarser meshes. The location of this increase can be correlated to the portion of the engine cycle when the intake valve has reached maximum lift (102 CAD).

The dissipation rate of the turbulent kinetic energy also shows variations with mesh size refinement; although these are not as pronounced as the variation in turbulent kinetic energy as a function of mesh size. The turbulent kinetic energy dissipation rate is $1.0x10^5$ $m^2/s^3$ higher for the 3mm mesh at the peak, located at 60 CAD, when compared to the 7.5mm mesh. The dissipation rate of turbulent kinetic energy is approximately $0.4x10^5$ higher for the majority of the engine cycle after this peak. The sharp deviation of the dissipation rate predicted with the 3 mm mesh might be due to better resolution of the turbulence using the finer mesh. Properly resolving these turbulent structures is important to adequately quantify fuel-air mixing in direct-injection engines.

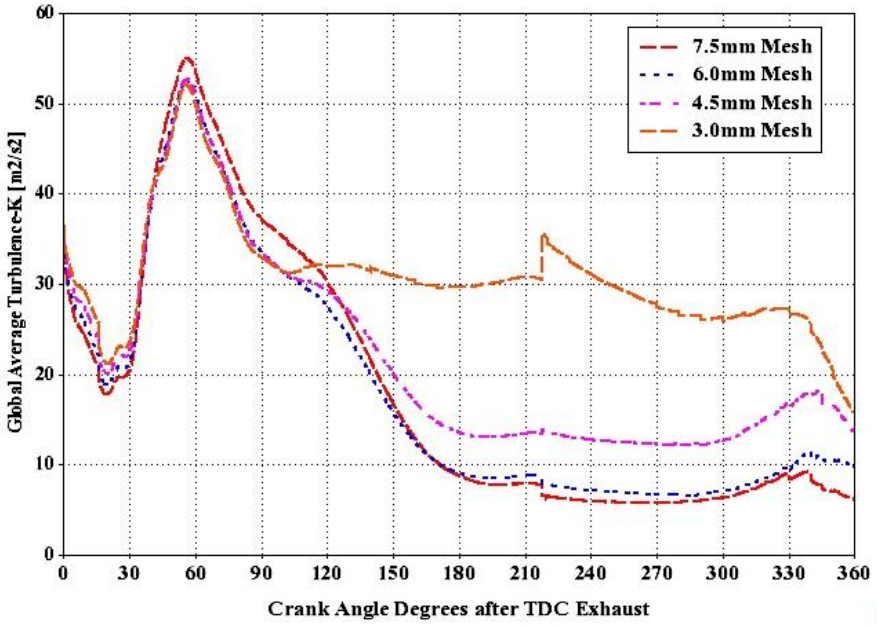


(A)

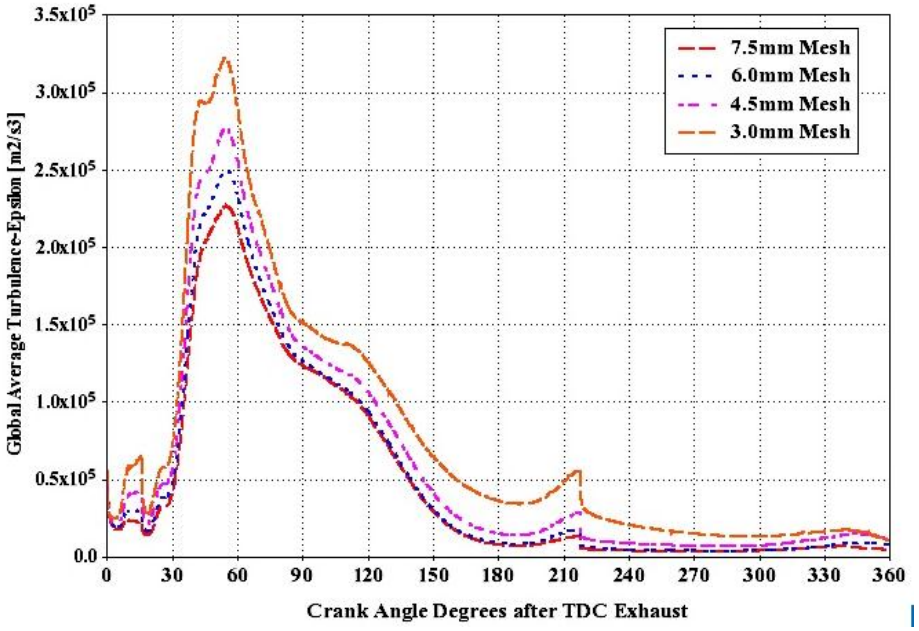


(B)

*Figure 80.* Turbulent kinetic energy [K] (A) and dissipation rate [epsilon] (B) as a function of Engine crank angle degree

The effect of mesh size on resolution can also be seen in Figure 81. The figure shows two-dimensional slices of the velocity field at bottom-dead-center, on a plane located at the centerline of the left most intake valve and parallel to the intake runner. It should be noted that the intake valve is still open. Two large-scale vortices are generated to the left and right of the intake valve. As the mesh size is decreased, these structures become better resolved. Results corresponding to the 3 mm mesh indicate that a third vortex develops midway up the left side of the cylinder. Although the decreased mesh size results appear promising, only physical measurement of the velocity fields at this location can validate these findings. This is the finest mesh that could be tested in the present model and, therefore, was selected for comparison with the preliminary study.

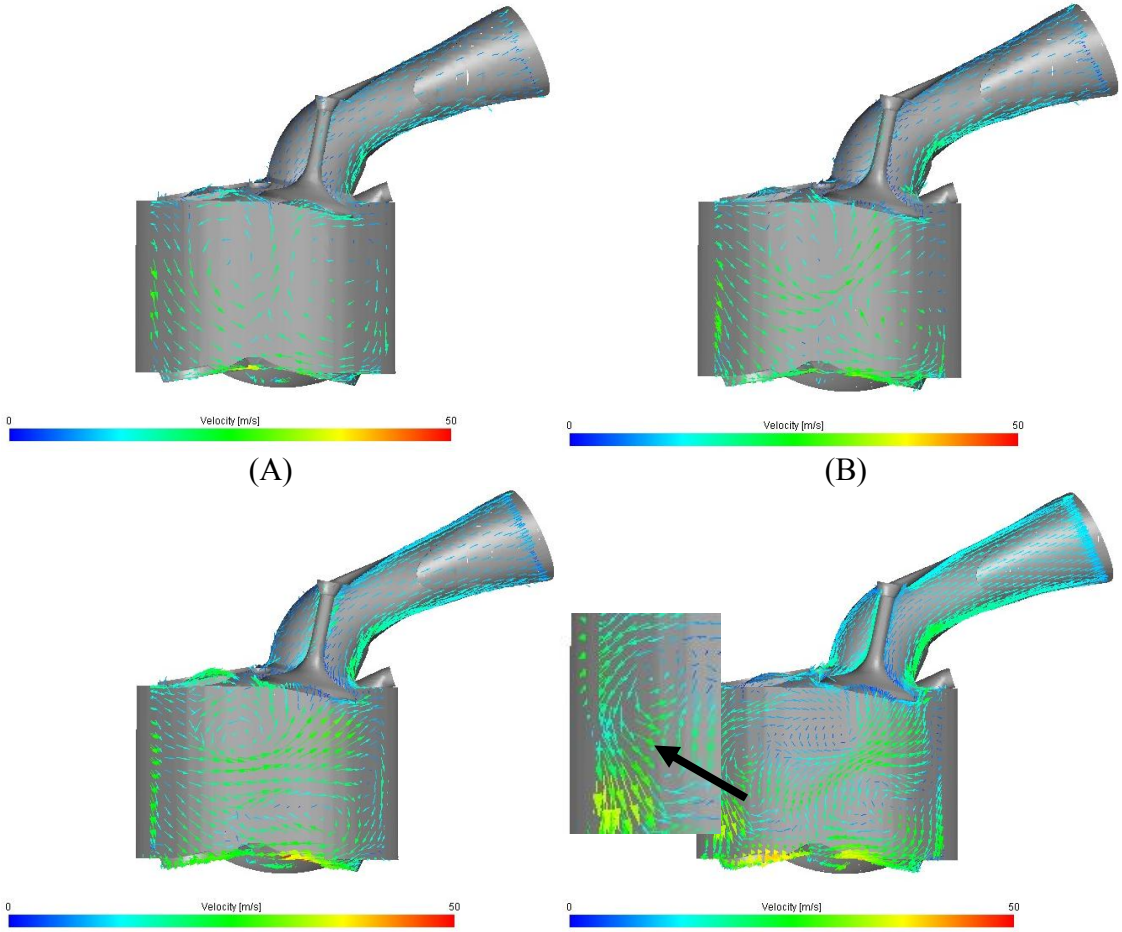


*Figure 81.* Velocity field at the vertical mid-plane of the left intake valve at BDC intake for 7.5 mm (A), 6.0 mm (B), 4.5mm (C), and 3mm (D) mesh sizes

## 4.6 Simulation Results and Validation

### 4.6.1 Pressure Results

In-cylinder pressure results from the preliminary simulation, refined simulation, and experimental data are shown in Figure 82 as a function of engine crank position relative to top- dead-center exhaust. Figure A shows pressure throughout the entire engine cycle. On this large scale, it is difficult to decipher differences in pressure from 0 to 240 CAD. During the compression stroke, (240 to 340 CAD), the preliminary simulation pressure correlates well with the experimental results. This was not expected, as the simulation featured higher compression ratio (14.0:1) compared to the experimental test engine (12.2:1) and, therefore, should exhibit higher pressure during the compression stroke. It is also observed that the peak pressure for the refined simulation is several times higher than that of the preliminary study (approximately 3.1 MPa compared to 0.8 MPa). The peak pressure predicted by either study was not compared to the experimental data, as neither model incorporated combustion, which will increase peak pressure and shift its location relative to top-dead-center.

Figure 82(B) shows the in-cylinder pressure during the intake and early compression strokes (TDC to 220 CAD). While neither simulation reproduces the experimentally measured in-cylinder pressure, the refined simulation introduced less uncertainty. The refined simulation showed a maximum deviation from the experimental data of approximately 25 kPa at 90 and 210 CAD, whereas the preliminary simulation shows a maximum deviation 50 kPa at 210 CAD.

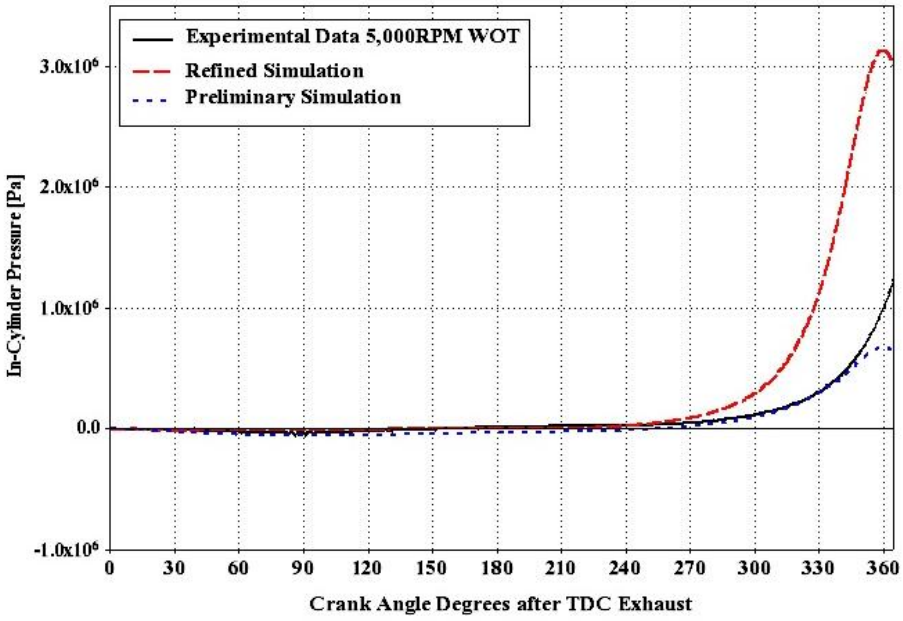


(A)

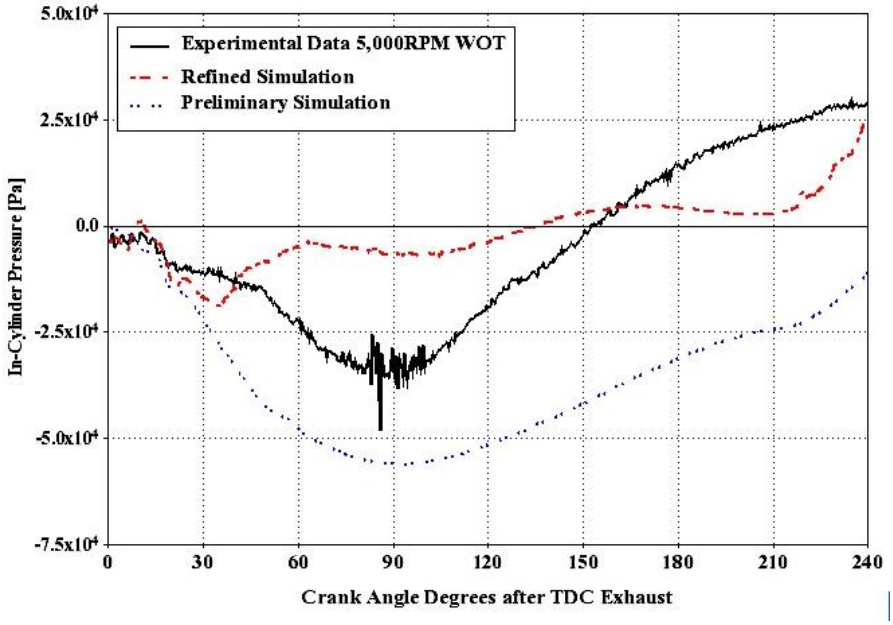


(B)

*Figure 82.* In-cylinder pressure for preliminary and refined simulations compared to experimental results as a function of crank angle throughout the cycle (A) and only the intake stroke (B)

### 4.6.2 Trapped Mass Results

The trapped mass in the cylinder after intake-valve-closing was also used to determine the accuracy of the preliminary and refined simulations with respect to experimental results. The global trapped mass as a function of crank angle is shown in Figure 83, where the red dashed line represents the refined simulation, the blue dotted line represents the preliminary simulation, and the solid black line represents the experimental mass trapped after intake-valve-closing. The experimental value was calculated using the steady state volumetric flow rate, the density of the ambient air, and engine speed measured during testing. Because the fuel mass injected is included in the simulation data, this mass was added to the calculated experimental value to allow direct comparison. The "jumps" in simulation data are due to the removal of the exhaust runner geometry (16 CAD) and removal of the intake runner geometry at (220 CAD). As experimental data was gathered at steady state and not recorded as a function of crank angle position, a quantitative comparison with simulation results is not available while the system is open (prior to intake-valve-closing at 220 CAD). After 220 CAD, the intake valves close and the quantitative comparison, shown in Figure 83, was possible. The refined simulation shows that, after intake-valve-closing, the mass within the system remains fairly constant throughout compression, as would be expected. This small variation in mass in the refined study could be contributed by fuel still being injected after intake valve closing. The preliminary simulation, however, predicts a decrease in trapped mass throughout the compression stroke.

A summary of trapped mass for the refined simulation, preliminary simulation, and experimental data just after intake-valve-closing (221 CAD) and at the end of compression (360 CAD) is shown in Table 18. Just after intake-valve-closing, the refined simulation had a 9% error with respect to the experimental value, while the preliminary simulation led to 23% error. At the end of the compression stroke, the refined simulation error increased to 11%, whereas the preliminary simulation led to 64% error. The error specified for the refined simulation might be partially augmented by fuel evaporation from the boundaries.

The realistic representation of constant mass during the compression stroke, and the significantly smaller error when compared to the experimental data, suggest that the refined simulation improved results. It should also be noted that the error present at the beginning of the refined simulation (0-16 CAD) may be further decreased by lowering the pressure at the exhaust boundary (i.e., by reducing backflow into the system).

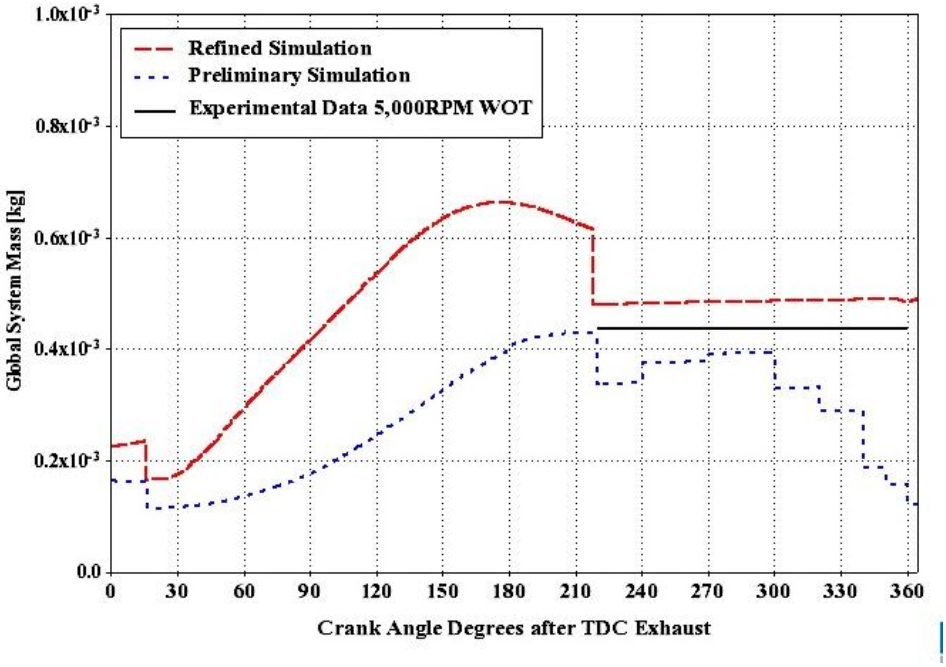


*Figure 83.* Global system trapped mass for preliminary and refined simulation compared to experimental results as a function of engine crank angle

*Table 18.* Trapped mass post intake valve closing results for experimental compared to preliminary and refined simulation and percent error

| Trapped Mass Comparison | | | | | |
|---|---|---|---|---|---|
| **Crank Angle [Deg]** | **Experimental Trapped Mass [kg]** | **Preliminary Study Trapped Mass [kg]** | **Refined Study Trapped Mass [kg]** | **Error Preliminary [%]** | **Error Refined [%]** |
| 221 | 4.38E-04 | 3.37E-04 | 4.79E-04 | -23% | 9% |
| 360 | 4.38E-04 | 1.57E-04 | 4.85E-04 | -64% | 11% |

4.6.3 Velocity Results

Finally, the flow fields predicted by the refined and preliminary studies were compared at the same plane used for the mesh refinement comparison. Shown in Figure 84 is the velocity plane located at the centerline of the left intake valve, parallel to the intake runner for both studies. The time step used is bottom-dead-center (intake stroke).Large-scale flow structures can be expected at this piston position. As no experimental validation was available, this comparison is qualitative. Two major differences are observed between the preliminary (A) and refined (B) studies: the magnitude and direction of the velocity within the intake runner, and the resolution of large-scale vortices.

The preliminary simulation predicts high velocity inflow occurring at bottom-dead-center. This is not expected, as at bottom-dead-center the maximum volume has been achieved and the mean intake flow velocity should decrease. The refined study shows significantly slower velocity magnitudes, in the out flow direction. This is a more reasonable situation, as the intake air momentum decreases at low engine speeds, and this might cause backflow at around bottom-dead-center.

The refined simulation used a 3 mm uniform mesh, where the preliminary study used 7.5 mm uniform mesh. While both simulations predict large-scale vortices to the left and right of the intake valve, the fine-scale structure of these vortices is better resolved with the finer mesh used in the refined simulation. Also observed in the refined simulation is a third smaller vortex appearing midway up the left side of the cylinder wall.

These qualitative results suggest improvements were made with the refined simulation when compared to the preliminary simulation. Additional physical test to measure the velocity fields at this location would be required to properly validate the velocity results

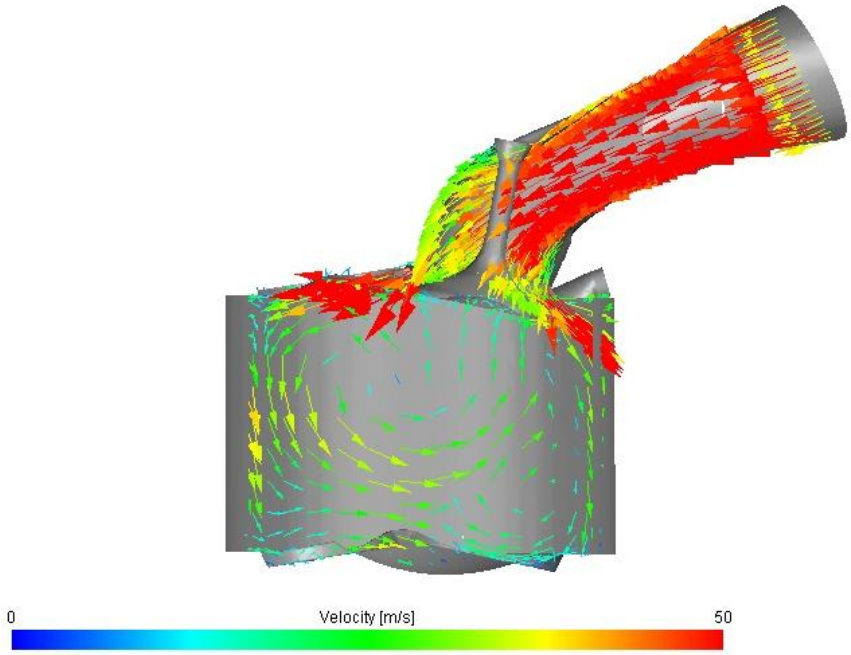


(A)

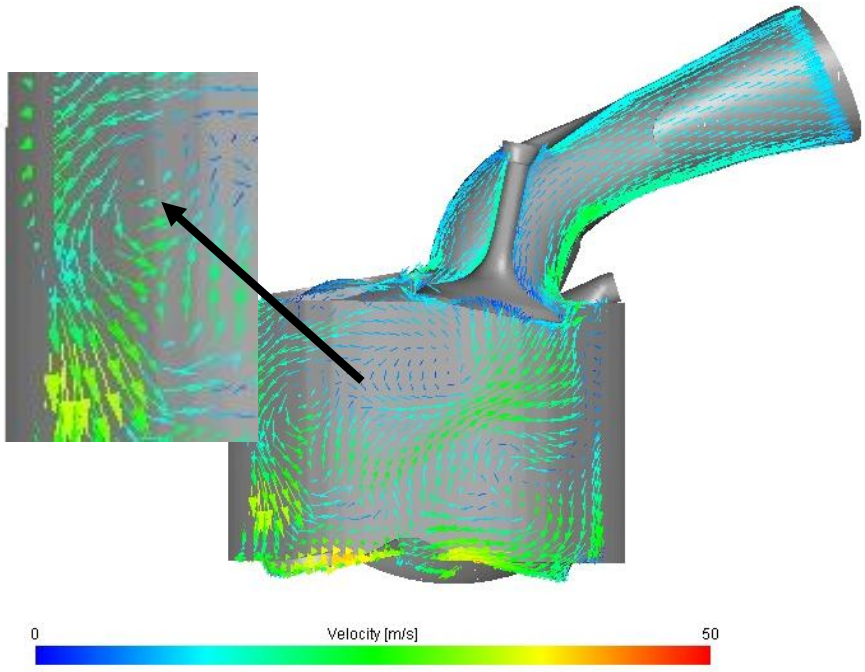


(B)

*Figure 84*. Velocity vectors at the vertical mid-plane of the left intake valve for preliminary (A) and refined simulations (B) at BDC.

# CHAPTER 5

# CUNCLUSIONS AND FUTURE WORK

## 5.1 Summary of Thesis

A benchmark study was conducted on a single-cylinder, Suzuki RM-450Z engine. Results were used to quantify engine performance and efficiency, and to refine a previously developed model of a gasoline direct-injection engine. In chapter 2, the performance and efficiency metrics were identified. These metrics were taken into consideration when developing the small engine test stand and instrumentation package. The engine was tested from 4,000 to 9,500 RPM at 30, 50, 65, 80, and 100 percent throttle openings. Results were quantified and explained in chapter 3. A previously developed computational model of the engine was reviewed in chapter 4 and the areas that required further refinement were identified. The refinement process was explored for a single test case at wide-open-throttle and 5,000 RPM engine speed. Results were compared to those of the preliminary study.

## 5.2 Conclusions

### 5.2.1 Test Stand and Instrumentation Setup

A modular test stand was successfully designed and constructed for testing the Suzuki RM-Z450 engine through the desired load and speed ranges. The test stand provides easy serviceability and adjustability to changes in experimental setups. Subsystems, including engine coolant heat exchanger and throttle actuator, controlled temperature and throttle position to $\pm$ 2.6 °F and $\pm$ 1% of the desired set points, respectively. The instrumentation

and data acquisition packages were successfully used to reliably acquire experimental data with minimal failures. The in-house developed user interface enabled convenient monitoring of all signals throughout the tests.

### 5.2.2 Engine Benchmarking Study

A benchmarking study was conducted on the Suzuki RM-450Z engine at 30, 50, 65, 80, and 100% throttle positions, and for engine speeds between 4,000 and 9,500 RPM. Data were recorded in 500 RPM increments across this range. Critical operating conditions such as engine coolant temperature, fuel pressure and temperature, and intake air temperature were found to remain consistent throughout testing, with maximum variations of $\pm$ 2.6 °F, $\pm$ 0.2 psi, $\pm$ 2.2°F, $\pm$1.6°F respectively. The integrated engine oil temperature control was found to be inadequate. Oil temperature ranged from 139.6 °F (59.8 °C) to 304.1 °F (151.2 °C) from what to what condition. Improved performance of what and extended oil life may be possible with improved temperature control. Maximum brake power and torque at 100% throttle were 67.4 HP (50.3 kW) at 8,500 RPM and 45.8 ft-lbf (62.1 N-m) at 7,000 RPM respectively. The volumetric efficiency reached 100% at 100% throttle and 6,500 RPM and the specific fuel consumption ranged between 200 and 255 g/(kWh), depending on speed and load. Boundary conditions for temperature and pressure were also quantified for use in the simulation refinement study.

### 5.2.3 Simulation Refinement

The previous design study, as well as the setup and results from a preliminary single-cylinder engine simulation were reviewed. Potential sources of uncertainty within this preliminary simulation were identified and a refinement study was conducted in those areas. Improvements were made in mesh distortion throughout the simulation using an improved geometry cross-linking scheme. Measured data from the engine benchmarking study was implemented into the initial and boundary conditions. A mesh size refinement study was also conducted for mesh sizes ranging between 7.5 mm and 2 mm. A 3 mm uniform mesh was found to better resolve mean velocity and turbulence. Finally, the preliminary and refined simulations were compared for accuracy, in comparison to experimentally measured in-cylinder pressure as a function of crank angle and trapped mass during the compression stroke. While neither model successfully predicted the in-cylinder pressure, the error was reduced with the refined simulation. The refined simulation also provided more realistic and accurate results in regards to trapped mass during the compression stroke, with 11% error when compared to experimental results.

## 5.3 Future Work

While this research significantly advances the development of more efficiency power train technologies for application in a Formula SAE or similar vehicle, several opportunities for improvement can be identified.

Additional work is required to improve the agreement between measured and predicted in-cylinder pressures. The current model can also be improved by gathering additional

experimental data. Areas of improvements include:

- Measuring thermal boundaries that were excluded in this work, such as piston and cylinder head faces, and valve body temperatures. This can be used to improve boundary heat transfer to the surrounding fluids.
- Measuring the intake and exhaust manifold pressures as a function of crank position. This would provide more realistic boundary conditions and may improve in-cylinder pressure results in modeling efforts.
- Replicating physical steady state flow testing for boundary conditions at specific crank angle locations (i.e., pressure differential between in-cylinder and manifold conditions during intake stroke) could be used to validate steady state simulation results at these locations
- Measuring the exhaust gas composition as a function of speed and load to establish a combustion efficiency benchmark for a gasoline direct-injection design.
- Quantifying transmission and engine-dynamometer coupling friction to more accurately define brake torque and power.
- Incorporating the Bosch's B6502 injector characteristics (e.g., droplet size probability distribution) to improve the spray model.

In order to fully develop and optimize the proposed gasoline direct-injection engine design, a more thorough CFD-based parametric study needs to be conducted for the entire engine cycle, encompassing a wide range of loads and speeds. Methods to reduce computational time should also be examined.

BIBLIOGRAPHY

1. **Enviromental Protection Agency.** EPA and NHTSA Finalize Historic National Program to Reduce Greenhouse Gases and Improve Fuel Economy for Cars and Trucks . *U.S. Enviromental Protection Agency.* [Online] Office of Transportation and Air Quality , April 05, 2010. [Cited: May 18, 2012.] http://www.epa.gov/oms/climate/regulations/420f10014.htm.

2. **Ford Motor Company.** How Ford's EcoBoost Does More with Less. [Online] May 2011. [Cited: May 18, 2012.] http://media.ford.com/images/10031/EcoBoost.pdf.

3. **General Motors.** All-New Ecotec 2.5L Powers Chevrolet Malibu's Quest for Quietness. *GM News.* [Online] 09 19, 2011. [Cited: 5 24, 2012.] http://media.gm.com/media/us/en/chevrolet/news.detail.html/content/Pages/news/us/en/2011/Sep/0919_malibu_noise_vibration.html.

4. **SAE International.** 2013 FR-S is Scion's halo car. *SAE International.* [Online] 5 21, 2012. [Cited: 5 24, 2012.] http://www.sae.org/mags/aei/11001.

5. *Development and Optimization of the Ford 3.5L V6 EcoBoost Combustion System.* **Jianwen Yi, Steven Wooldridge, Gary Coulson, Jim Hilditch, Claudia O. Iyer,Peter Moilanen, George Papaioannou, David Reiche, Michael Shelby, Brad VanDerWege,Corey Weaver, Zheng Xu, George Davis, Brett Hinds and Andreas Schame,l Ford Motor Company.** 2009, Society Of Automotive Engineers 2009-01-1494.

6. **Formula One World Championship Ltd.** Kinetic Energy Recovery Systems (KERS). *Formula1.com.* [Online] Formula One World Championship Ltd, 2012. [Cited: January 8, 2012.] http://www.formula1.com/inside_f1/understanding_the_sport/8763.html.

7. 2010 Rule Changes- accommodating larger fuel tanks. *Formula 1.* [Online] 2012. [Cited: 5 18, 2012.] http://www.formula1.com/news/technical/2010/0/714.html.

8. **European Le Mans Series.** Michelin Green X Challenge. *Lemans-Series.com.* [Online] lephare. [Cited: January 8th, 2012.] http://www.lemans-series.com/en/s02_corporate/s02p04_michelin.php.

9. **SAE International.** *2012 Formula SAE® Rules.* Warrendale : SAE International, 2012.

10. —. *2009 Formula SAE® Rules.* Warrendale : SAE International, 2009.

11. **Nienhuis, Michael J, Van Gemert, Geoff and Haydon, Nicholas.** *Development of a Gasoline Direct Injection Fuel System for a Single Cylinder Engine.* Kalamazoo : Western Michigan University, 2009.

12. **Heywood, B. John.** *Internal Combustion Engine Fundamentals.* New York : McGraw-Hill, Inc., 1988.

13. **Suzuki Motor Corporation.** *Suzuki RM-Z450 Owner's Service Manual.* Takatsuka : Suzuki Motor Corporation, 2008.

14. **SAE Standards.** Engine Power Test Code-Spark Ignition and Compression Ignition - Net Power rating-SAE J1349 Aug2004. Warrendale, PA : SAE International, 2004. SAE J1349 Aug2004.

15. **Ricardo.** Ricardo VECTIS user manual version 3.13.

16. **Go Power Systems.** *Go-Power Hydraulic Dynamometer D-100 Power and Torque Capacity Diagram.* Plymouth : Froude Hofman, 2003.

APPENDICES

APPENDIX A: KISTLER CALIBRATION CHART

KISTLER
measure. analyze. innovate.

# Kalibrierschein DRUCK
# Calibration Certificate PRESSURE

Type **6113BFD35Q04** Serial No. **1928619**

| Kalibriert durch<br>Calibrated by | Datum<br>Date |
|---|---|
| G. Ratano | 15.12.2010 |

| Referenzgeräte<br>Reference Equipment | Typ<br>Type | Serien-Nr.<br>Serial No. |
|---|---|---|
| Gebrauchsnormal<br>Working Standard | Kistler 6961A250 | 992713 |
| Ladungskalibrator<br>Charge Calibrator | Kistler 5395A | 605251 |

| Umgebungstemperatur<br>Ambient Temperature<br>°C | Relative Feuchte<br>Relative Humidity<br>% |
|---|---|
| 25 | 33 |

## Messergebnisse Results of Measurement

| Kalibrierter Bereich<br>Calibrated Range<br>bar | | Empfindlichkeit<br>Sensitivity<br>pC / bar | Linearität<br>Linearity<br>≤ ± %FSO |
|---|---|---|---|
| 0 ... 200 | (23°C) | -9,918 | 0,08 |
| 0 ... 100 | (23°C) | -9,883 | 0,11 |
| 0 ... 50 | (23°C) | -9,868 | 0,14 |
| 0 ... 150 | (200°C) | -10,11 | 0,10 |
| 0 ... 100 | (200°C) | -10,08 | 0,09 |
| 0 ... 50 | (200°C) | -10,03 | 0,21 |

**Messverfahren** **Kontinuierliche Kalibrierung, Vergleichsverfahren**
Measurement Procedure Continuous Calibration, Comparison Method

Kistler betreibt die SCS Kalibrierstelle Nr. 049, akkreditiert nach ISO 17025. SCS Kalibrierzertifikate sind auf Bestellung erhältlich.
Kistler operates the SCS Calibration Laboratory No. 049, which is accredited per ISO 17025. SCS Calibration Certificates are available on request.

## Bestätigung Confirmation

Das oben durch die Serienummer identifizierte Gerät entspricht der Vereinbarung der Bestellung und hält die Herstelltoleranzen gemäss den Spezifikationen der Datenblätter ein. Dieses Dokument erfüllt die Anforderungen von EN 10204 Abnahmeprüfzeugnis "3.1". Alle Messmittel sind auf nationale Normale rückverfolgbar. Das Kistler Qualitätsmanagement System ist nach ISO 9001 zertifiziert. Dieses Dokument ist ohne Unterschrift gültig.
The equipment mentioned above and identified by Serial Number complies with the agreement of the order and meets the manufacturing tolerances specified in the data sheets. This document fulfils the requirements of EN 10204 Inspection Certificate "3.1". All measuring devices are traceable to national standards. The Kistler Quality Management System is certified per ISO 9001. This document is valid without a signature.

**Kistler Instrumente AG**
Eulachstrasse 22
PO Box
CH-8408 Winterthur
Tel. +41 52 224 11 11
Fax +41 52 224 14 14
info@kistler.com
ZKB Winterthur BC 732
Swift: ZKBKCHZZ80A
Account: 1132-0374.628
IBAN: CH67 0070 0113 2003 7462 8
VAT: 229 713
ISO 9001 certified
www.kistler.com